

Novel spin functionalities of C₆₀ based metallo-molecular interfaces



Matthew Rogers

School of Physics and Astronomy

University of Leeds

Submitted in accordance with the requirements for the degree of

Doctor of Philosophy

April 2019

For my parents and grandparents

Intellectual Property Statement

The candidate confirms that the work submitted is his own, except where work which has formed part of jointly authored publications has been included. The contribution of the candidate and the other authors to this work has been explicitly indicated below. The candidate confirms that appropriate credit has been given within the thesis where reference has been made to the work of others.

This copy has been supplied on the understanding that it is copyright material and that no quotation from the thesis may be published without proper acknowledgement.

The right of Matthew Rogers to be identified as Author of this work has been asserted by him in accordance with the Copyright, Designs and Patents Act 1988.

©2019 The University of Leeds and Matthew Rogers.

In all cases, Dr. O. Céspedes provided guidance for experiments and data analysis. Design and optimisation of C_{60} is done by Dr. M.C. Wheeler and Dr. O. Céspedes.

Work from the following jointly authored publications is presented in this thesis:

F. Al Ma'Mari, **M. Rogers**, S. Alghamdi, T. Moorsom, S. Lee, T. Prokscha, H. Luetkens, M. Valvidares, G. Teobaldi, M. Flokstra, R. Stewart, P. Gargiani, M. Ali, G. Burnell, B. J. Hickey O. Céspedes. "Emergent magnetism at transition-metal-nanocarbon interfaces. *PNAS*, 114(22), 5583-5588 (2017).

This work forms the interpretation of work in Chapter 5, but is not explicitly presented in the results chapter. The findings of this work are presented as part of the literature review in Chapter 2.

Work attributable to the candidate: Growth and characterisation of C₆₀ based samples, contributed to the magnetometry and XAS/XMCD measurements, and contributed to the data analysis.

Work attributable to others: F. Al Ma'Mari grew and characterised C₆₀ based multilayers, performed the μ SR measurements and contributed to the data analysis. S. Alghamdi grew and characterised the amorphous-carbon samples. Dr. G. Teobaldi performed and analysed the DFT simulations. Dr. T. Prokscha, Dr. H. Luetkens, Dr. S. Lee, Dr. M. Flokstra and R. Stewart contributed to the design and analysis of the μ SR experiments. Dr. T. Moorsom, Dr. M. Valvidares and Dr. P. Gargiani contributed to the design and analysis of the XAS/XMCD experiments. Dr. M. Ali, Dr. G. Burnell and Prof. B.J. Hickey: general help with this work and with discussion/ideas. Dr. O. Céspedes designed the study, analysed the data and wrote the manuscript. All authors discussed the results and commented on the manuscript.

M. Rogers[†], T. Moorsom[†], I. Scivetti, S. Bandaru, G. Teobaldi, M. Valvidares, M. Flokstra, S. Lee, R. Stewart, T. Prokscha, P. Gargiani, G. Stefanou, M. Ali, F. Al Ma’Mari, G. Burnell, B. J. Hickey and O. Céspedes. ”Reversible spin storage in metal oxide-fullerene heterojunctions”, *Submitted to Science Advances*. [†] The authors have contributed equally to this work

This work is included within Chapter 4. Some figures featured within Chapter 4 have been taken from this jointly authored work. Fig. 4.1 is attributable to O. Céspedes, Figs. 4.2(b) and 4.14(a) are attributable to T. Moorsom and Fig. 4.13 is attributable to G. Teobaldi in collaboration with O. Céspedes

Work attributable to the candidate: All sample design, deposition and data analysis related to the μ SR measurements, RT transport and PL spectroscopy measurements. Contributed to the sample fabrication and data analysis of XAS/XMCD measurements. Contributed to the preparation of the manuscript.

Work attributable to others: Dr. T. Moorsom contributed to the sample fabrication and data analysis of XAS/XMCD measurements and contributed to the preparation of the manuscript. Dr. I. Scivetti, Dr. S. Bandaru and Dr. G. Teobaldi performed and analysed the DFT simulations. Dr. M. Flokstra, Dr. S. Lee, R. Stewart and Dr. T. Prokscha contributed to the design and analysis of the μ SR experiments. Dr. M. Valvidares and Dr. P. Gargiani contributed to the design and analysis of the XAS/XMCD experiments. G. Stefanou provided aid with optical lithography needed for μ SR samples. Dr. M. Ali, Dr. G. Burnell and Prof. B.J. Hickey: general help with this work and with discussion/ideas. Dr. O. Céspedes designed the study, analysed the data and wrote the manuscript. All authors discussed the results and commented on the manuscript.

Acknowledgements

Firstly, I would like to thank my supervisor Dr Oscar Céspedes with whom it has been a pleasure to work. Without his deep insight and guidance into experimental physics, this work would not have been possible. He has always been able to come up with more daring beam time proposals to keep us all on our toes. Without the experience of these experiments, I wouldn't have enjoyed my PhD half as much as I have. I was fortunate to benefit from the scientific insight of Dr Fatma Al Ma'Mari in the early years of my PhD. Her overwhelming enthusiasm and kindness really made the time we worked together a delight. It must also equally thank Dr Timothy Moorsom who is extraordinarily tenacious and proficient, yet is always more than willing to help and engage with other peoples work. His in-depth knowledge on such a wide range of subjects has not only helped me with interpreting data, but has made whiling away hours on beamlines a pleasure. I am thankful for Dr May Wheeler's extensive work in setting up and optimising the growth systems and protocols used in this work. The advice and interest of Professors Bryan J Hickey and Christopher Marrows as well as the advice of Dr Satoshi Sasaki and Dr Thomas Moore has been invaluable. I am particularly appreciative of Dr Gavin Burnell and Dr Mannan Ali whose patience and willingness in helping to set up experiments is a true asset to the group. I am grateful to all the members of the engineering workshops for masterfully turning my scribbles on pages into cryostat heads and PCB boards. I am also thankful to the past and present members of the cryogenic team, in particular, John Turton and Brian Gibbs for always 'keeping it cool'. Throughout my time in the CM group, it has been a pleasure to work with countless great colleagues and undergraduates that provide both a stimulating and friendly atmosphere.

I am indebted to Dr Thomas Prokscha, Dr Manuel Valvidares and Dr Pierluigi Gargiani. As the beamline scientists in charge of the LEM and XAS instrumentation, I owe the success of the majority of experiments featured within this thesis to these people. They are all

remarkably dedicated to their instruments, and each one has gone above and beyond in using their expertise to adapt beamlines for our challenging experiments. They have all shown great patience in training me in the use of instrumentation, but most of all each has been great company throughout. It has been a great pleasure counting muons with the St Andrews group, made up of Professor Steve Lee, Dr Machiel Flokstra and Rhea Stewart. For the last three years, their passion for superconductors and muons has indeed rubbed off on me and has provided the genesis for the superconducting work seen within this thesis.

I am lucky enough to have an amazingly supportive group of friends in Leeds. In particular, I am grateful to Tom Rylands, Sam Boote, Becky Winwood and Kami for being lovely housemates. I owe much of my mental wellbeing to the kindness and support of you all and the rest of the A-block crew. I would like to express my deepest appreciation and thanks to my parents, brother, sister and grandparents for their unwavering support. Each of you has provided me with so much inspiration and have nurtured the analytical and creative disposition that is needed for the undertaking of a PhD. Most importantly, I would like to thank Lucy Garwood for her enduring support, calm understanding and words of comfort. Only the continuous support and love of friends and family have made this work possible. Thank you very much, everyone!

Abstract

Novel functionalities of C_{60} -based interfaces are investigated with the aim of controlling induced spin-dependent phenomena through electrical and optical charging in photovoltaic devices and the generation of spin-triplet correlations in magneto-molecular/superconductor proximity systems.

Low-energy muon spin rotation is used to probe local magnetic field distributions in molecule/metal-oxide heterojunctions. It is shown that the population of interfacial traps after electrical and optical charging produces an induced magnetisation due to the spin-splitting of the interface. This is supported by XAS and XMLD measurements in similar systems. The emergence of a peak at 282 eV, often associated with interfacial hybridisation, after an electrical bias shows a magnetic field dependence in its X-ray linear dichroism. We propose how these effects may be reversibly switched on and off through the tuning of the interfacial chemistry via electromigration of oxygen in the device.

In Nb/C_{60} stacks a superconducting state can be induced in the molecular layer via the proximity effect. The incorporation of weakly magnetic Cu/C_{60} interfaces leads to the emergence of a paramagnetic spin susceptibility in the superconducting state, as probed by low-energy muon spin rotation. We attribute this effect to the generation of odd-frequency spin-triplet correlations at the spin-split Cu/C_{60} interface.

These studies are a demonstration of novel device architectures available to the field of molecular spintronics. Utilising the unique spin-dependent phenomena observed in hybrid molecular interfaces, systems with new functionalities can be designed.

CONTENTS

1	Introduction	1
1.1	Thesis Layout	4
2	Theoretical background	7
2.1	Introduction	8
2.2	Magnetism in metals	8
2.2.1	Domain formation and the demagnetising field	12
2.3	Magnetism in molecules	12
2.4	Interfacial charge transfer and spin-dependent interfaces	15
2.4.1	The effect of molecular interfaces on metals	20
2.5	Electronic properties of fullerenes	22
2.6	Superconductivity	23
2.6.1	The London theory	24
2.6.2	The Ginzberg-Landau theory	25
2.6.3	Bardeen, Cooper and Schrieffer (BCS) theory	28
2.6.4	Triplet superconductivity	28
2.7	Proximity effects	30
2.7.1	Superconductor-ferromagnet (S/F) proximity effects	32
2.7.2	Experimental evidence of the LRTC through anomalous screening effects at S/F interfaces	35
3	Experimental methods	36
3.1	Sample preparation	37
3.1.1	Sputter deposition	37

3.1.2	Molecule sublimation	39
3.2	X-ray reflectivity	41
3.3	SQUID VSM magnetometry	43
3.4	Raman and photoluminescence measurements	44
3.5	X-ray absorption spectroscopy and magnetic dichroism	46
3.6	Low energy muon spin rotation (LE- μ SR)	48
3.6.1	Muonium formation	52
3.6.2	Characterisation of the muonium state in thin film C ₆₀	54
4	Reversible spin storage in C₆₀/metal-oxide heterojunctions	59
4.1	Introduction	60
4.2	Transport characterisation of metal-oxide /molecule devices	63
4.3	XAS of C ₆₀ junctions	67
4.4	LE- μ SR studies of spin trapping at MnO _x /C ₆₀ interface	72
4.4.1	LE- μ SR with electrical charging	72
4.4.2	Transverse field measurements	79
4.4.3	LEM with optical excitation	81
4.5	Discussion	88
4.6	Outlook	90
5	Incorporation of spin-active metal/C₆₀ interfaces for superconducting spintronics	96
5.1	Introduction	97
5.2	Low-temperature transport of SC-Molecular proximity structures	98
5.3	Characterisation of the emergent magnetism at a Cu/C ₆₀ interface by LE- μ SR	102
5.4	Anomalous screening effects measured by LE- μ SR	108
6	Conclusions and future work	123
	References	130

Abbreviations

BCS	Bardeen Cooper Schrieffer	CMOS	Complimentary metal-oxide-semiconductor
DC	Direct current	DFT	Density functional theory
DOS	Density of states	E_F	Fermi energy
EDX	Energy dispersive X-ray spectroscopy	FCC	Face centred cubic
FFLO	Fulde Ferrell Larkin Ovchinnikov	FFT	Fast Fourier transform
FM	Ferromagnet	G-L	Ginzberg Landau
HOMO	Highest occupied molecular orbital	HRS	High resistance state
IV	Current-voltage	LE- μ SR	Low-energy muon spin rotation
LEM	Low-energy muon	LRS	Low resistance state
LRTC	Long-range triplet component	LUMO	Lowest unoccupied molecular orbital
MR	Magnetoresistance	Mu@C ₆₀	C ₆₀ endohedral muonium state
MuC ₆₀	C ₆₀ radical muonium state	N	Normal metal
NEXAFS	Near edge X-ray absorption fine structure	OSC	Organic semiconductor
PL	Photoluminescence	RF	Radio frequency
RMS	Root mean square	RT	Room temperature
SC	Superconductor	SHIPS	Spin-hybridisation-induced polarised states
SMM	Single-molecule-magnet	SOC	Spin-orbit coupling
SOMO	Singly occupied molecular orbital	SQUID	Superconducting quantum interference device
SRTC	Short-range triplet component	TEM	Transmission electron microscopy
TEY	Total electron yield	TF	Transverse field
UHV	Ultra high vacuum	VSM	Vibrating sample magnetometry
XAS	X-ray absorption spectroscopy	XMCD	X-ray magnetic circular dichroism
XMLD	X-ray magnetic linear dichroism	XRD	X-ray diffraction
XRR	X-ray reflection	ZF	Zero field
ZPL	Zero phonon line		

CHAPTER 1

Introduction

The work within this thesis was undertaken between 2015 and 2019. In that time, global electricity usage has increased from around 22,400 TWh to an expected 25,300 TWh. This represents a year on year growth of about 3%.^[1] In the last two decades, there has been an increasing need for large data centre computation and information storage, driven by the growing use of personal consumer devices and cloud computing. As the appetite for an ever digitised society grows, the expected proportion of global electricity consumption attributable to the ICT sector is expected to increase from 11% in 2019 up to an expected 21% by 2030. In the same period, annual global greenhouse gas emissions are projected to inflate from 55.4 to 70 Gigatonnes. Currently, the ICT sector accounts for nearly 3% of global emissions, yet by 2030 this could increase up to 6.7%. Furthermore, there is a growing popularity for technologies such as cryptocurrencies that can be very computationally intensive. We are also witnessing the internet-of-everything paradigm where more and more appliances are being designed with integrated smart-phone control. With the addition of these, among other, factors the carbon footprint from the ICT sector could increase even beyond 20% of global emissions by 2030.^[2] The 2018 report produced by the intergovernmental panel on climate change (IPCC) has warned that the next 12 years are critical for policy-makers to invest in changing the global energy economy. Such provisions are needed to ensure that global warming remains under 1.5 °C.^[3]

To allow for the inevitable growth of the ICT economy whilst also reducing the expected carbon footprint of this sector, the devices we use must aim to make more out of scarce energy resources. In traditional silicon-based CMOS devices, energy is wasted as heat dissipation due to the motion of charge. One approach to the challenge of reducing our dependence on energy has been the rise of spintronics which utilises the spin degree of freedom for memory and logic operations.^[4] The reduced time scale and energy required for the switching of spin states compared to the charge flow within CMOS devices could lead to faster and more energy efficient computing.^[5] This can, of course, be taken further by the incorporation of superconducting materials which are dissipation-less by their very nature. The early Josephson junction based logic circuits, developed in the 90s, were shown to operate at comparable speeds to CMOS technology whilst also delivering increased energy efficiency, even when including the energy cost of refrigeration.^[6; 7] What has not been developed in this

field is an approach to memory elements that can compete with the information density and stability of CMOS or spintronic devices. It would, therefore, be advantageous to combine the fields of spintronics and superconductivity to utilise the non-volatility of magnetic memory with the low energy dissipation and high processing speeds of superconductors.

Magnetism and superconductivity have classically been considered as antagonistic states of matter as the Cooper pairs which make up the superconducting condensate are broken apart by the exchange field within a ferromagnet. Despite this, the theoretical proposal of spin-triplet Cooper pair states which have aligned spin polarisations could allow for the complete synergy of these two fields.[8; 9] Therefore, the field of super-spintronics has emerged, which is dedicated to the production of spin-triplet states and their incorporation into magnetic memory and logic devices.[10] Where innovations in the ICT sector require an increased need for large data centres, low-temperature computing could significantly reduce the ecological footprint of these emergent technologies whilst also providing increased processing speeds. For the personal devices used by most of society, advances in room temperature spintronics may be needed for the same improvements to data processing speeds and reduced energy consumption.

Society's increased reliance on technology brings about additional challenges. In particular, it is essential to consider the sustainability for the mining of materials required within these devices.[11; 12] A possible solution to this issue is provided within the field of molecular spintronics where the constituent materials can be artificially synthesised rather than mined. This could lead to potentially biodegradable or recyclable devices.[13] Molecular spintronics is a field that emerged when attempts to enhance the efficiencies of organic light emitting diodes were made by using ferromagnetic electrodes.[14] Although the original goal of the project was unsuccessful, the 2002 observation of spin injection from LSMO into sexithienyl (T_6) by Dediu et al. has led to the rise of a field which incorporates molecular materials into spintronic devices that can operate between macroscopic and single molecular scales.[15] The precise chemical control of single-molecule-magnets (SMMs), which exhibit magnetic-memory effects between quantum spin states, show promise for

high-density information storage.[16]

Molecular materials might not, at first glance, seem an appropriate choice for spintronics. For the most part, they have low mobilities compared to inorganic semiconductors and highly complex charge transport properties which can influence spin injection.[17] However, being made from constituent elements of a low atomic number means that spin-orbit coupling is relatively weak. Also, the abundant C^{12} isotope has no nuclear moment, and thus it possesses no hyperfine interaction. Therefore, long spin-relaxation times can be achieved in carbon-based materials.[18] From a practical point of view, molecular materials can be processed very cheaply and have very high chemical and mechanical flexibility.[19] When deposited onto metallic substrates, the hybridisation between molecular orbitals and metallic bands can also lead to new interface phenomena.[20; 21] There is now a concerted effort to comprehend the complex spin-dependent interactions between molecules and metals as manipulating these behaviours may be exploited to develop multifunctional devices.[22] Overall, organic spintronic devices at the present date may not compete with inorganic devices for longevity and reproducibility. However, the new functionalities available from organics combined with their ease of processing provides a promising route towards increased sustainability for the production of memory and logic devices.[23]

1.1 Thesis Layout

The reduction of the ICT sector's reliance on energy resources will likely require developments made across many fields. In particular, increased sustainability might be aided by advancements in room temperature spintronics and low-temperature super-spintronics. The appropriate use of superconducting devices might be for large data centres where refrigeration can be supplied. Nevertheless, in both of these cases, it would be advantageous also to consider how carbon-based materials can be utilised for their multifunctional capabilities, reduced production costs and greater sustainability by virtue of molecular synthesis. This thesis, therefore, aims to demonstrate how the spin-dependent phenomena at molecular C_{60} interfaces can provide new functionalities within both fields. In Chapter 4, a novel room temperature spintronic device is presented which combines the spin-dependent interfacial hybridisation at a

metal-oxide/ C_{60} interfaces with the optical properties of the molecular layer to create a prototypical ‘spin capacitor’ that can be optically or electrically charged. In Chapter 5, we explore how emergent magnetic phenomena at the interface between C_{60} and normal metals can be incorporated into a superconducting proximity structure in order to produce long-range triplet Cooper pair states for low-temperature superconducting spintronics.

In Chapter 2, a theoretical overview of ferromagnetism is given, including a brief description of the manifestation of magnetic order in molecular materials. Critical aspects of molecular materials concerning their application within spintronics are also discussed. Specifically, the effects of interfacial charge transfer and the creation of hybrid interface states for designing materials useful for spintronic applications are reviewed. Toward the end of Chapter 2, the principal theories related to superconductivity are presented whilst the interfacial physics that emerges through the coexistence of superconducting and magnetic long-range order is reviewed. In particular, the current state of the detection of long-range triplet Cooper pair states via muon spin rotation spectroscopy is considered as is relevant for the understanding of the results presented within this work.

Chapter 3 describes the experimental methods used in this work. These include; sample deposition, structural, magnetic and optical characterisation techniques. The samples are produced by a combination of sputter deposition of metals with metal oxides produced by *in situ* plasma oxidation. C_{60} is deposited by *in situ* molecular sublimation. The structural morphologies of the thin films are characterised by X-ray reflectivity and X-ray diffraction (XRR/XRD). The magnetic properties of the macroscopic structures are determined by superconducting quantum interference device (SQUID) vibrating sample magnetometry (VSM). Raman and photoluminescence spectroscopy provide optical characterisation. Where greater understanding on the location of magnetic ordering is required, synchrotron techniques such as X-ray absorption spectroscopy (XAS), X-ray magnetic circular dichroism (XMCD), X-ray linear dichroism (XLD) and low energy muon spin rotation (LE- μ SR) are used. SQUID magnetometry measures the magnetic properties of the whole sample. XMCD can provide element specific magnetic characterisation

by tuning X-ray energy to specific elemental absorption lines. LE- μ SR can instead provide depth specific characterisation by tuning the implantation depth of the muon beam. Low-temperature electrical transport characterisation has been obtained by use of a continuous-flow cryostat. The workings of a cryostat are not discussed in Chapter 3 as it is not necessary for the reader's understanding of the obtained results.

Chapter 4 presents the study of reversible spin storage in C₆₀/metal-oxide heterojunctions. XAS and XMCD results demonstrate that the accumulation and extraction of charge in C₆₀/metal-oxide heterojunctions are spin-dependent. Photoluminescence measurements are used to characterise the current pathways within these structures via the negative luminescence effect. XLD characterises changes to the C₆₀ orbital structure within such a device, where the difference in absorption for linear and vertical light polarisation is shown to be highly sensitive to an applied magnetic field. Wide-area junctions are fabricated for the study of the accumulated spin polarisation by LE- μ SR. The local magnetic field profile is probed within these samples with *in situ* electrical and optical charging. The results obtained through each technique are discussed in detail where density functional theory calculations have aided the interpretation of results.

A pioneering study into the incorporation of spin-polarised molecular interfaces for superconducting spintronics is presented within Chapter 5. In this work, emergent magnetic order arises at the interface between non-magnetic Cu and molecular C₆₀. The localisation of this magnetism to the interface between Cu and C₆₀ is probed with LE- μ SR. By using low-temperature electrical transport, the length scale over which Cooper pair states can maintain coherence within the molecular C₆₀ is determined via the inverse proximity effect. The screening effects produced when the weakly magnetic Cu/C₆₀ system is proximitised to a niobium substrate are then characterised by LE- μ SR. Simulations are provided to correlate the observed internal field profiles of these systems to proposed signatures which indicate the creation of spin-triplet superconducting correlations. Finally, in Chapter 6 all the results from experiments are summarised and interpreted. An outlook for future work based on the results gathered is then proposed.

CHAPTER 2

Theoretical background

2.1 Introduction

This chapter aims to offer a brief introduction to the concepts of magnetism and superconductivity and how these phenomena can be manipulated through the design of interfaces comprised of metals with different long-range order and molecular systems. An overview of the fundamental properties of organic semiconductors (OSCs) and in particular, C₆₀, is given. The emergence of spin-dependent hybridisation at metal/molecular interfaces is discussed, while the conditions necessary for the onset of an emergent ferromagnetic state in non-magnetic materials are also described.

2.2 Magnetism in metals

The spontaneous onset of magnetism in zero field is a phenomenon that has piqued the interest of humanity for millennia. The understanding of the origin of ferromagnetism has only really come about within the last century due to the discovery of the electron spin and the advent of quantum mechanics. The overlap of neighbouring electron wavefunctions leads to the ordering of a collection of spins via the exchange interaction. Exchange is, in essence, quantum mechanical in origin and is fundamental to the alignment of spin along a single axis. We may describe the exchange interaction by considering two electrons that have spatial coordinates \mathbf{r}_1 and \mathbf{r}_2 . The total state wavefunction for such a system is

$$\Psi_{1,2} = \Phi_a(\mathbf{r}_1)\Phi_b(\mathbf{r}_2). \quad (2.1)$$

Here, $\Psi_{1,2}$ describes the total state wavefunction. $\Phi_a(\mathbf{r}_1)$ and $\Phi_b(\mathbf{r}_2)$ describe the wavefunctions for particles 1 and 2 respectively. These include a spatial ($\psi(\mathbf{r})$) and spin ($\chi(s)$) component, given by

$$\Phi(\mathbf{r}, s) = \psi(\mathbf{r})\chi(s). \quad (2.2)$$

According to the Pauli exclusion principle, the total wavefunction must be anti-symmetric under electron exchange such that

$$\Phi_a(\mathbf{r}_1)\Phi_b(\mathbf{r}_2) = -\Phi_b(\mathbf{r}_1)\Phi_a(\mathbf{r}_2). \quad (2.3)$$

This can be achieved in two ways, by having a symmetric spatial state combined with an antisymmetric spin state ($S=0$) or by an antisymmetric spatial state with a symmetric spin state ($S=1$). This gives the respective spin-singlet (χ_S) and spin-triplet (χ_T) states, which may take the following forms:

$$|\chi_S\rangle = \frac{1}{\sqrt{2}}(|\uparrow\downarrow\rangle - |\downarrow\uparrow\rangle) \quad (2.4)$$

$$|\chi_T\rangle = \begin{cases} |\uparrow\uparrow\rangle \\ \frac{1}{\sqrt{2}}(|\uparrow\downarrow\rangle + |\downarrow\uparrow\rangle) \\ |\downarrow\downarrow\rangle \end{cases} \quad (2.5)$$

The total wavefunction for the singlet (Ψ_S) and triplet (Ψ_T) states are then

$$\Psi_S = \frac{1}{\sqrt{2}} [\psi_a(\mathbf{r}_1)\psi_b(\mathbf{r}_2) + \psi_a(\mathbf{r}_2)\psi_b(\mathbf{r}_1)] \chi_S \quad (2.6)$$

$$\Psi_T = \frac{1}{\sqrt{2}} [\psi_a(\mathbf{r}_1)\psi_b(\mathbf{r}_2) - \psi_a(\mathbf{r}_2)\psi_b(\mathbf{r}_1)] \chi_T. \quad (2.7)$$

The energy of the two possible states are

$$E_{S(T)} = \int \Psi_{S(T)}^* \hat{\mathcal{H}} \Psi_{S(T)} d\mathbf{r}_1 d\mathbf{r}_2. \quad (2.8)$$

Assuming correct normalisation of the spin wavefunctions, we may define the exchange integral, J , to be proportional to the difference in energy between the singlet and triplet spin states as

$$J = \frac{E_S - E_T}{2} = \int \psi_a^*(\mathbf{r}_1)\psi_b^*(\mathbf{r}_2) \hat{\mathcal{H}} \psi_a(\mathbf{r}_2)\psi_b(\mathbf{r}_1) d\mathbf{r}_1 d\mathbf{r}_2. \quad (2.9)$$

The difference in energy derived here is effectively an electrostatic interaction due to the exchange of two identical particles. In 1928 Heisenberg incorporated this exchange integral into a Hamiltonian that describes the exchange interaction energy for a generalised many-body system. The Heisenberg Hamiltonian for two spin states, \mathbf{S}_i and \mathbf{S}_j , at lattice positions i and j , can be written as

$$\hat{\mathcal{H}}_{Ex} = -2 \sum_{i>j} J_{ij} \mathbf{S}_i \cdot \mathbf{S}_j, \quad (2.10)$$

where J_{ij} is the exchange integral between the i^{th} and j^{th} spin. For two electrons occupying the same shell of a single atom, electrostatic repulsion will attempt to maximise their spatial separation. This can be achieved by adopting an antisymmetric spatial state. This will be accompanied by a symmetric spin wavefunction and so will lead to parallel spin alignment while minimising the Coulomb repulsion, as is consistent with Hund's first rule. It would appear, then, that any atom with unpaired electrons in the valence orbital would have positive exchange coupling and hence ferromagnetic order. However, the majority of transition metals, which have unpaired electrons in the outer d subshell exhibit paramagnetic or diamagnetic behaviour, with only three elements being ferromagnetic at room temperature: iron (Fe), cobalt (Co) and nickel (Ni). The non-integral moment per atom of $2.2 \mu_B$ in Fe is also illogical based on localised moments solely interacting via exchange.[24]

In 1907, prior to the Heisenberg model, Pierre Weiss proposed that some internal molecular field, \mathbf{B}_{MF} , proportional to the magnetisation exists within a ferromagnetic material. This is written as

$$\mathbf{B}_{MF} = \lambda \mathbf{M}. \quad (2.11)$$

By only considering dipolar interactions, the size of the molecular field λ needed to stabilise ferromagnetic behaviour could not be accounted for until the understanding of Heisenberg's electrostatic exchange interaction came about.

In 1938 Edmund Stoner set out to predict the spontaneous onset of magnetism in metals through the application of Weiss' molecular field theory to the free electron model. First, consider the energy cost of taking spin down electrons with energies from $E_F - \delta E$ up to E_F , flipping their spin, and placing them in the spin up band such that they now occupy an energy range from E_F up to $E_F + \delta E$, where the electrons occupy states up to the Fermi energy (E_F). The number of electrons, δn , transferred is

$$\delta n = \frac{g(E_F)\delta E}{2}, \quad (2.12)$$

where $g(E_F)$ is the density of states at the Fermi level. The energy increase per state is δE . The total kinetic energy cost $\Delta E_{K.E}$ is, therefore,

$$\Delta E_{K.E} = \frac{1}{2}g(E_F)(\delta E)^2. \quad (2.13)$$

The interaction between the magnetisation of a material and the molecular field λ gives an energy reduction that can account for the cost in energy for the band splitting. Assuming a magnetic moment per electron of $1 \mu_B$, the magnetisation of the spin-split system will be

$$\mathbf{M} = \mu_B(n_\uparrow - n_\downarrow). \quad (2.14)$$

The associated molecular field energy will then become

$$\Delta E_{MF} = - \int_0^M \mu_0(\lambda M') dM' = -\frac{1}{2}\mu_0\lambda M^2 = -\frac{1}{2}\mu_0\lambda\mu_B^2(n_\uparrow - n_\downarrow)^2. \quad (2.15)$$

Substituting $J = \mu_0\mu_B^2\lambda$, J being the exchange integral introduced within Heisenberg's exchange model:

$$\Delta E_{MF} = -\frac{1}{2}J(g(E_F)\delta E)^2. \quad (2.16)$$

A total change in energy ΔE is then obtained:

$$\Delta E = \Delta E_{K.E} + \Delta E_{MF} = \frac{1}{2}g(E_F)(\delta E)^2(1 - Jg(E_F)). \quad (2.17)$$

We can now see that spontaneously spin-split bands will form for $\Delta E < 0$, when

$$Jg(E_F) \geq 1. \quad (2.18)$$

This simple relationship, known as the Stoner criterion, demonstrates that a metal with sufficient exchange interaction strength and density of states at the Fermi energy will exhibit spontaneous ferromagnetism. Spin up and spin down bands will be split by an exchange energy ΔE , in the absence of an applied field.[\[25\]](#) A material's magnetic properties are directly related to the band structure via the DOS at the Fermi level and the exchange integral. Changes to a material's band structure can hence be expected to cause changes to its magnetic properties.

2.2.1 Domain formation and the demagnetising field

So far we have considered the manifestation of a magnetisation vector, \mathbf{M} , inside a magnetic material which requires the exchange interaction between individual spins along a regular lattice. It might be assumed that for some infinite plane, after the application of an external magnetic field (\mathbf{H}_{Ext}), \mathbf{M} shall remain aligned along the same axis. If we were to measure the magnetisation of a magnetic film after the \mathbf{H}_{Ext} field has been removed, we would observe that there is a remanent magnetisation, that is often less than that observed at saturation. This is due to the formation of domains within the sample, where the magnetisation within each domain may reach the saturation value. However, they need not lie parallel to one another. The formation of magnetic domains saves energy associated with dipolar fields. As $\nabla \cdot \mathbf{B} = 0$ and $\mathbf{B} = \mu_0(\mathbf{H} + \mathbf{M})$ it is clear that

$$\nabla \cdot \mathbf{H} = -\nabla \cdot \mathbf{M}. \quad (2.19)$$

Therefore, when there is some abrupt end to the magnetisation (at say the edge of a thin film), there is a divergence in the magnetic field. This produces a demagnetising field with energy

$$E_D = -\frac{\mu_0}{2} \int_V \mathbf{M} \cdot \mathbf{H}_D dV, \quad (2.20)$$

where \mathbf{H}_D is the demagnetising field. The domain structure of a magnetic material in zero field is then a balance between the energy saved due to the reduction in the above magnetostatic energy against the energy associated with the formation of a domain wall.

2.3 Magnetism in molecules

Magnetic materials are conventionally inorganic compounds where the unpaired d or f orbitals (for transition and rare earth materials respectively) form the basis for most magnetic phenomena. In the last few decades, the realisation of magnetic effects in organic-based compounds has become an important focus due to the prospect of highly tunable properties owing to the complexities of carbon-based chemistry.[26] In the

early 1960s, Edelstein and Mandel performed paramagnetic resonance measurements of Wurster’s blue perchlorate which alluded to the onset of molecular ferromagnetism at sufficiently low temperatures.[27] In 1963, McConnell supplied some theoretical insight related to the work by Edelstein and Mandel by considering the stabilisation of ferromagnetic exchange coupling between two molecular sites. Rewriting the Heisenberg Hamiltonian to approximate the exchange interaction between two aromatic radicals A and B gives

$$\mathcal{H}^{AB} = -\mathbf{S}^A \cdot \mathbf{S}^B \sum_{ij} J_{ij}^{AB} \rho_i^A \rho_j^B, \quad (2.21)$$

where $\mathbf{S}^A(\mathbf{S}^B)$ is the total spin operator for molecule $A(B)$. $\rho_i^A(\rho_j^B)$ is the π -spin density on atom $i(j)$ of molecule $A(B)$. The exchange integral J_{ij}^{AB} is expected to favour anti-parallel alignment since the overlap of singly occupied molecular orbitals (SOMOs) will tend to lead to a state with similar attributes of a bonding orbital. Consequently, in this case, we assume J_{ij}^{AB} to be negative.[28] SOMO spin up (α') electrons will experience a different electron-electron repulsion with spin up (α) and spin down (β) electrons in the fully occupied molecular orbital (FOMO). Therefore, SOMO α' electrons will redistribute themselves in space, leading to areas of varying π -spin density. A positive π -spin density is defined for when SOMO α' electrons have a non-zero contribution. A negative π -spin density is defined for when SOMO α' electrons have no contribution. The McConnell mechanism proposes that if two neighbouring aromatic molecules are stacked on top of another, an overlap of orbitals with opposite ρ (a region of positive spin density overlapping with a region of negative spin density) can lead to an overall ferromagnetic interaction.[29]

A second mechanism was proposed by McConnell to describe spontaneous magnetism in charge-transfer salts. Triplet states emerging through excitations between donor and acceptor molecules that propagate through the charge transfer molecular chain, giving rise to magnetic ordering.[30; 31] In 1987, the McConnell II mechanism was used to describe the ordering in the first organic-based magnet, $[\text{Fe}^{III}(\text{C}_5\text{Me}_5)_2][\text{TCNE}]$, which orders below 4.8 K.[32] Such mechanisms based on charge transfer were also used to describe the magnetic state in tetrakis(dimethylamino)ethylene [TDAE]- C_{60} in 1991.[33] Subsequent structural

studies of the charge transfer complex indicated the importance of the relative orientation of the C_{60} molecules to each other for the emergence of the magnetic state below 16 K.[34] Within the same year, the first room-temperature molecular/organic based magnet was synthesised through the reaction of bis(benzene)vanadium and tetracyanoethylene (TCNE).[35] $V[TCNE]_x$ is an intrinsic ferrimagnetic semiconductor ($E_g=0.5$ eV, $\sigma = 0.01$ Scm $^{-1}$ at RT) which can be grown by chemical vapour deposition (CVD) on a variety of substrates whilst maintaining quality factors (Q-factors) that rival those of epitaxial YIG.[36] The versatility of $V[TCNE]_x$ demonstrates the feasibility of integrating bulk molecular-based magnetic materials into spintronic devices especially, in this case, for magnonic devices.

Despite the successes of generating room temperature magnetism in bulk 3d molecule-based materials, the stabilisation of a magnetic state in single molecules remains a technological challenge. Single-molecule-magnets (SMMs) are an attractive route to high-density magnetic recording as they possess extremely long magnetisation relaxation times, reaching years below 2 K. Unlike conventional methods of preparing magnetic nanoparticles, the component size will be reliably identical, leading to a low distribution of switching times.[37] This class of material contains an inner magnetic core with a surrounding shell of organic ligands which show magnetic hysteresis below a characteristic blocking temperature. Until recently, blocking temperatures (T_B) have been limited to liquid helium temperatures. However, the synthesis of the dysprosium metallocene cation $[(Cp)^{Pr5}Dy(Cp^*)]^+$ (Cp^{Pr5} = penta-iso-propylcyclopentadienyl, Cp^* = pentamethylcyclopentadienyl) has demonstrated how the engineering of parameters such as the ligand bond angle and Dy-Cp distances can lead to improvements in magnetic stability. In this case, the effective energy barrier for the reversal of magnetisation is significant enough to make the Cp-Dy-Cp system magnetically order below 80 K.[38]

2.4 Interfacial charge transfer and spin-dependent interfaces

During the last few decades, research into two prominent areas of materials science, spintronics and molecular electronics have begun to coalesce. Organic semiconductor (OSC) materials have been considered as promising substitutes for inorganic spacer layers in spintronic devices as they possess a number of desirable properties such as chemical and mechanical flexibility. In particular, OSCs generally have low spin-orbit coupling (SOC) strengths. Early resonance measurements have shown spin relaxation times exceeding microseconds, surpassing those of metals ($\sim 10^{-12}$ s for Cu [39]) and crystalline semiconductors ($\sim 10^{-9}$ s for Si [40]).[18; 41] Pioneering work by Tsukagoshi et al. in 1999 represents the first integration of carbon-based molecules within spintronic device architectures. Resistance measurements of carbon nanotubes sandwiched between Co electrodes showed magnetic hysteresis, as would be expected from a conventional spin valve structure. The spin-polarised charges, injected into the nanotubes were shown to diffuse over a length scale of the order of 100 nm.[42]

Following from this, Dediu et al. presented the first experimental evidence in 2002 of spin-polarised injection into a prototypical OSC, sixithienyl (T_6).[15] Later, the study by Céspedes et al. of carbon nanotubes in contact with a ferromagnetic substrate demonstrated that hybridisation between molecular orbitals and those of the metallic substrate occurs. This results in a spin-dependent charge transfer, inducing a magnetic moment of $0.1 \mu_B$ per contact carbon atom.[43] In 2009, the injection of spin-polarised carriers into OSCs was directly observed in two studies. The first by Cinchetti et al.[44] by the use of spin-resolved two-photon photoemission (SR-2PPE) and the second by Drew et al.[45] through the use of low-energy muon spin rotation (LE- μ SR). As the efficiency of spin injection into OSCs will be highly dependent upon the spin-dependent properties of the interface, the emergent spin polarisation that can occur due to interfacial hybridisation has become a recent focus of research, and remains an essential consideration for the emergent field of organic spintronics.[46]

In 2010 Barraud et al. considered the role of chemical bonds on the spin injection efficiency of OSC spin-valves. For LSMO/tris[8-hydroxyquinoline]-

2.4 Interfacial charge transfer and spin-dependent interfaces

aluminium(Alq_3)/Co nanojunctions, magnetoresistance effects of up to 300% at 2 K were observed.[20] This was nearly an order of magnitude larger than that observed for macroscopic junctions of identical composition.[47] Barraud et al. predicted that the overlap between the ferromagnetic, metallic and molecular orbitals leads to the formation of spin-hybridisation-induced polarised states (SHIPS) which act as an effective magnetic electrode and has a vital role in the magneto-resistive characteristics of the device.[48] This insight was utilised by Raman et al. to develop a device that comprised of a single ferromagnetic electrode and a spin-dependent hybrid molecular interface layer. The spin filtering properties of the adsorbed organometallic molecule gave rise to an interface magnetoresistance effect of up to 20% near room temperature.[49] The term ‘spinterface science’ was coined by Sanvito to describe the study and engineering of SHIPS for spintronic devices.[50]

In an isolated molecular semiconductor, electron energies are characterised by discrete levels or molecular orbitals. This is in contrast to typical inorganic semiconductors whose periodic crystal lattice leads to a continuum of states described by bands. Molecular energy states shall be occupied up to the Fermi energy giving rise to the highest occupied molecular orbital (HOMO) and lowest unoccupied molecular orbital (LUMO). These orbitals are analogous to the valence and conduction bands, respectively, for band semiconductors. A simplistic model would assume that as molecules are brought into contact with a metallic substrate, vacuum level alignment (Schottky-Mott limit) would occur. This would infer that any resultant charge transfer would be highly dependent on the relative difference of work function (ϕ) of the metallic substrate to the electron affinity (E_A) of the molecule.[51]

In the case of C_{60} , the ionisation potential has been measured to be around 6.9 eV.[52] Considering the band gap between the HOMO and LUMO is approximately 2.3 eV, we would expect that $E_A \sim 4.6$ eV. However, several studies of C_{60} adsorbed onto a range of metals such as Mg($\phi = 3.6$ eV), Au ($\phi = 5.1$ eV) and Ag ($\phi = 4.3$ eV) show charge redistribution from the metal into the molecular LUMO, in all cases, indicating that there is no intrinsic dependence on vacuum level alignment.[53; 54] Instead, chemical interactions and electron transfer distort the electronic structure of a molecule close to the interface leading to the redistribution of charge and the

2.4 Interfacial charge transfer and spin-dependent interfaces

formation of an interfacial dipole. The weak dependence of charge redistribution on work function is known as Fermi-level pinning. A complete model of Fermi-level pinning in the case of molecule-metal interfaces must take full consideration of chemical bonding, orbital hybridisation and interfacial dipole formation.[51; 55–57]

As a consequence of interfacial hybridisation, when a molecule is brought into proximity with a metallic electrode, there is a finite probability that an electron in the molecular orbital will leak into the metal. The lifetime (τ) of the interfacial molecular state has, therefore, been reduced as compared to the same energy state for an isolated molecule. Consequently, the molecular orbital energy is no longer well defined as an energy broadening of the molecular orbital (Γ) is experienced via the uncertainty principle ($\Gamma \propto \frac{\hbar}{\tau}$). The energy level broadening is expected to be dependent upon the DOS of the metal. Depending on the strength of the interaction, Γ can range from meV (physisorption) up to eV (chemisorption). Some physical examples are provided in Fig. 2.1 of the possible range of interaction types.[55]

As a result of charge redistribution and resultant interfacial dipole formation, the effective energy (ϵ_{eff}) of the molecular orbital shall also be shifted from its bulk energy (ϵ_0). ϵ_{eff} is also expected to be proportional to the DOS of the metallic substrate. If we consider the outcome of a molecule absorbed onto the surface of a ferromagnetic (FM) substrate, the DOS ($D_{FM}(E)$) is now different for spin up and spin down ($D_{FM}^{\uparrow}(E) \neq D_{FM}^{\downarrow}(E)$). Consequently, the initial spin degenerate molecular orbitals shall experience two different level broadening widths, $\Gamma^{\uparrow} \neq \Gamma^{\downarrow}$, and two different shifts in energy, $\epsilon_{eff}^{\uparrow} \neq \epsilon_{eff}^{\downarrow}$ for the two spin directions.

2.4 Interfacial charge transfer and spin-dependent interfaces

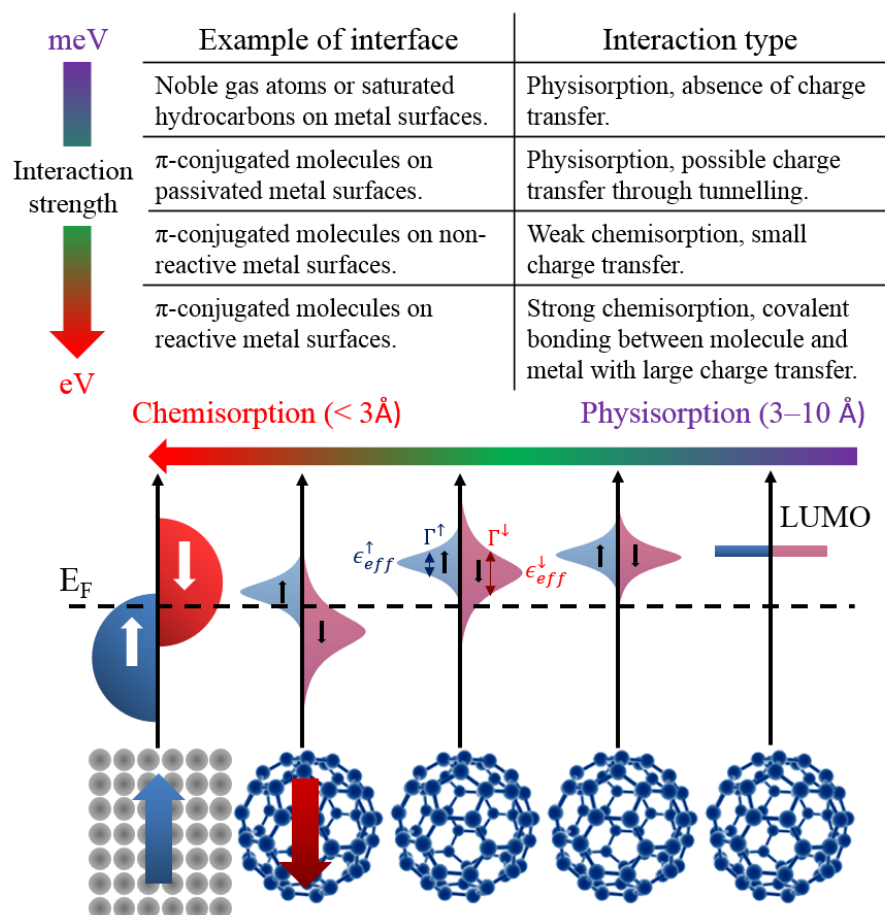


Figure 2.1: Top: Examples of molecular interfaces, with expected interaction types, are shown. Adapted from [55]. Bottom: a schematic representation of the molecular energy level broadening and spin-dependent splitting due to orbital hybridisation with a ferromagnetic metal surface. For an isolated (bulk) molecule there is negligible interaction between the molecule and metal and as such bulk electronic properties are maintained. For distances of around 3 Å, weak (physisorption) interactions lead to a broadening of the molecular orbitals. For simplicity, this has just been represented here for the molecular LUMO, but similar effects are expected for other molecular orbitals. As the distance between the molecule and substrate shortens, the interaction becomes progressively stronger (chemisorption). Energy level broadening and energy shifting become spin-dependent due to spin-split DOS of the ferromagnetic substrate. For some choices of material, this can lead to the inverse spin polarisation being induced in the hybrid interface states. Figure adapted from [50].

2.4 Interfacial charge transfer and spin-dependent interfaces

As shown in Fig. 2.1 it is clear to see how this spin-dependent energy broadening and shifting may induce an interfacial spin polarisation (P_{int}) into the molecular orbital, defined as

$$P_{int} = \frac{D_{int}^{\uparrow} - D_{int}^{\downarrow}}{D_{int}^{\uparrow} + D_{int}^{\downarrow}}, \quad (2.22)$$

where $D_{int}^{\uparrow(\downarrow)}$ is the DOS of the molecular interface (spinterface). The interface DOS can be described by a Lorentzian distribution, $D_{int}^{\uparrow(\downarrow)}(E)$, characterised by a width ($\Gamma^{\uparrow(\downarrow)}$) and centre position ($\epsilon_{eff}^{\uparrow(\downarrow)}$):

$$D_{int}^{\uparrow(\downarrow)}(E) = \frac{\Gamma^{\uparrow(\downarrow)}/2\pi}{(E - \epsilon_{eff}^{\uparrow(\downarrow)})^2 + (\Gamma^{\uparrow(\downarrow)}/2)^2}. \quad (2.23)$$

From this, we can see that the nature of the chemical interactions at the interface can have a critical effect on P_{int} .

First, consider the case where the broadening is much larger than the energy difference of the orbital to the Fermi level, $\Gamma \gg \Delta E$, with $\Delta E = E_F - \epsilon_{eff}^{\uparrow(\downarrow)}$. From equation 2.23 we see that $D_{int}^{\uparrow(\downarrow)} \simeq \frac{1}{\Gamma^{\uparrow(\downarrow)}}$. We have already established that $\Gamma^{\uparrow(\downarrow)} \propto D_{FM}^{\uparrow(\downarrow)}$ hence we may rewrite the spin polarisation of the interface as

$$\lim_{\Gamma \gg \Delta E} P_{int} = -\frac{\Gamma^{\uparrow} - \Gamma^{\downarrow}}{\Gamma^{\uparrow} + \Gamma^{\downarrow}} \propto -\frac{D_{FM}^{\uparrow} - D_{FM}^{\downarrow}}{D_{FM}^{\uparrow} + D_{FM}^{\downarrow}} = -P_{FM}, \quad (2.24)$$

where the spin polarisation of the interface is shown to be oppositely coupled to that of the ferromagnet.

Now consider the case where the molecular orbital level is only slightly shifted and the broadening is small, $\Delta E \gg \Gamma$. The interface DOS now becomes, $D_{int}^{\uparrow(\downarrow)} \simeq \frac{\Gamma^{\uparrow(\downarrow)}}{(\Delta E^{\uparrow(\downarrow)})^2}$ and so $D_{int}^{\uparrow(\downarrow)} \propto \frac{D_{FM}^{\uparrow(\downarrow)}}{(\Delta E^{\uparrow(\downarrow)})^2}$. The interface spin polarisation is now

$$\lim_{\Delta E \gg \Gamma} P_{int} = \frac{\frac{\Gamma^{\uparrow}}{(\Delta E^{\uparrow})^2} - \frac{\Gamma^{\downarrow}}{(\Delta E^{\downarrow})^2}}{\frac{\Gamma^{\uparrow}}{(\Delta E^{\uparrow})^2} + \frac{\Gamma^{\downarrow}}{(\Delta E^{\downarrow})^2}} \propto \frac{\frac{D_{FM}^{\uparrow}}{(\Delta E^{\uparrow})^2} - \frac{D_{FM}^{\downarrow}}{(\Delta E^{\downarrow})^2}}{\frac{D_{FM}^{\uparrow}}{(\Delta E^{\uparrow})^2} + \frac{D_{FM}^{\downarrow}}{(\Delta E^{\downarrow})^2}}. \quad (2.25)$$

This yields a situation where P_{int} is no longer opposite in sign to that of the ferromagnetic electrode but for weak coupling between the molecule and metal,

2.4 Interfacial charge transfer and spin-dependent interfaces

$P_{int} > P_{FM}$. The spin-dependent energy shift $\epsilon^{\uparrow(\downarrow)}$, found within $\Delta E^{\uparrow(\downarrow)}$ now acts to selectively filter spins due to the modulation in the effective barrier height for spin up electrons tunnelling into the interface as compared to that for the spin down electrons.[58]

This model proposed by Barraud and co-workers demonstrates how spin-splitting and the spin injection efficiency, of organic semiconductors, can be highly tuned by hybridisation at the interface. Subsequent experimental evidence of these effects was obtained through spectroscopy and magnetotransport studies. Spin-polarised STM of H₂Pc on an iron surface showed the predicted spin polarisation inversion of the H₂Pc orbitals.[59] However, the deposition of the same molecule on a Co substrate showed an enhanced GMR ratio of around 60%, again measured by SP-STM. The spin filtering at the molecular interface in this system gives a GMR ratio around one order of magnitude larger than is obtained from direct tunnelling from the Co substrate to the STM tip.[60] The microscopic origin of spin filtering at Co/Alq₃ interfaces was explored by Steil et al. in 2013. By exciting charge carriers into hybrid interface states and probing the time evolution of the transient population by two-photon photoemission spectroscopy, the authors found that charge carriers at the hybrid interface are trapped at the interface by spin-dependent confining potentials. In this study, the spin-polarised carriers are trapped for a time on the order of 1 ps.[61] These studies show how magnetotransport properties can be modulated through the engineering of molecular interfaces.

2.4.1 The effect of molecular interfaces on metals

We have so far considered the changes to the DOS that molecules experience due to hybridisation, assuming the metal substrate to be thick enough that any changes to the metal DOS are screened over a few Å. It is also the case, however, that the magnetic and electronic properties of adequately thin metallic substrates can be modulated through such interactions.[62–64] Of particular relevance to this study is the observation by Al Ma’Mari et al. of an emergent magnetisation in transition metals due to the effect of orbital hybridisation and charge transfer at normal metal-C₆₀ interfaces. In this system, changes in the curvature of the Cu DOS and increases in the exchange integral

2.4 Interfacial charge transfer and spin-dependent interfaces

through magnetic hardening of interfacial Cu atoms yield an observable room temperature magnetic ordering in Cu that has been interfaced with C_{60} . [21] It has been shown to exist for other transition metals where the resultant maximum magnetisation in the transition metal appears to be correlated to the charge transfer expected when interfaced with C_{60} . X-ray dichroism measurements (XMCD) in a magnetic Sc- C_{60} system show a polarisation dependence in the C_{60} absorption edge that is indicative of a sizeable magnetic moment in the fullerene. [65] For the carbon K edge, X-ray transitions occur from the 1s states into the 2p final states. As the 1s states have not been spin-split due to the spin-orbit interaction, the sum rules cannot be applied. [66] Consequently, it is challenging to distinguish between orbital and spin momentum contributions to the overall magnetic moment. [62]

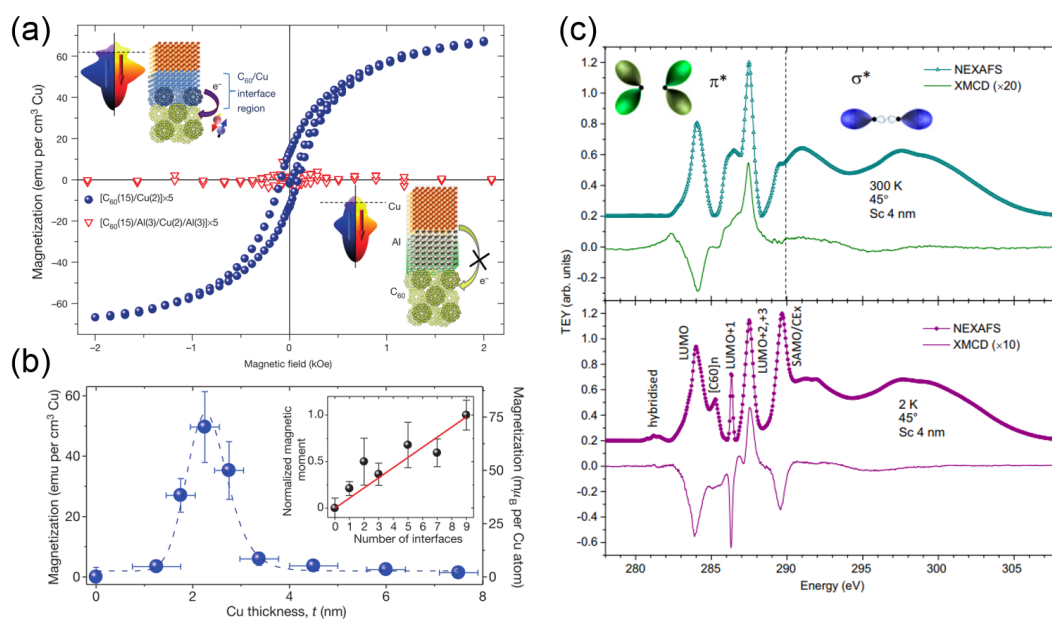


Figure 2.2: (a) The effect of the molecular interfaces on the magnetic properties of Cu. Charge transfer and interface reconstruction result in substantial changes in the DOS of the metallic film and the emergent of magnetic ordering. Interfaces where the charge transfer and hybridisation is screened by an Al spacer layer show no emergent magnetism. (b) The dependence of the emergent magnetism is highly dependent upon the Cu layer thickness. Films thinner than 1.5 nm are discontinuous, yet films thicker than 3 nm appear to screen the changes in the DOS and hence show no magnetic ordering. (c) The XAS/XMCD spectrum is obtained for a C_{60} -Sc magnetic system where the induced magnetism leads to measurable dichroism in the C_{60} DOS. Figures (a) and (b) are adapted from [21] and (c) from [65].

The emergent magnetic effects that may be generated at C_{60} interfaces are exploited throughout this thesis to bring about spin-polarised interfacial states that act as stable spin-dependent charge traps (see Chapter 4). They are also used to investigate the generation of spin-correlated superconducting states when proximitised to superconducting substrates (see Chapter 5).

2.5 Electronic properties of fullerenes

The carbon allotrope Buckminsterfullerene, C_{60} , possesses many desirable properties making it a promising candidate for investigation in spintronic applications. Being a purely carbon system, it has virtually negligible hyperfine interaction as the naturally abundant C^{12} isotope has no nuclear moment. In contrast to most organic semiconductors, C_{60} shows suitable mechanical robustness against metal penetration during metal deposition.[67] Therefore, it can be incorporated into devices, where sizeable magnetoresistance (5.5% for a 28 nm barrier layer) has been measured at room temperature.[68; 69] Spin-orbit coupling strengths in carbon allotropes are distinguishable by their shape. For instance, the SOC in C_{60} is distinctly larger than that for C_{70} or graphene. The curvature of the molecule leads to hybridisation of the π and σ orbitals, enhancing its SOC.[70; 71] This makes fullerene C_{60} particularly efficient in spin-charge conversion via the inverse spin Hall effect.[72]

Organic semiconductors and fullerenes are characterised by strong intramolecular covalent bonds with relatively weak intermolecular Van de Waals forces. Carbon has an electron configuration of $1s^2, 2s^2, 2p^2$. When forming molecular bonds, electrons with principal quantum number $n = 2$ form three distinct hybridisations: sp^3 , sp^2 and sp^1 . These orbital configurations not only lower the overall energy of the system but are also responsible for the highly variable electronic and mechanical properties of the carbon allotropes. When Kroto et al. discovered fullerene C_{60} in 1985, they were able to attribute the high stability of C_{60} to the strong σ bonds which, for the sp^2 configuration, are the product of $2s$ electrons hybridising with the planar $2p_y$ and $2p_x$ orbitals. The remaining $2p_z$ orbitals overlap to generate the weakly bonding π orbitals. Electrons in these π orbitals are delocalised to the entire molecule. Consequently,

electron transport takes place via hopping events between the π orbitals of adjacent molecules. Whilst the highly localised σ orbitals are generally found well below E_F , and therefore do not contribute to the transport properties of the fullerenes, but are crucial to the mechanical stability of the cage.

Fullerene C_{60} has a complex geometry. It belongs to the icosahedral I_h symmetry group which possesses 120 possible symmetry operations, including reflections and rotational transformations. In bulk, C_{60} cages form a face-centred cubic (fcc) structure at room temperature where the individual molecules are orientationally disordered and freely rotate between degenerate configurations via a ratcheting mechanism.[73] Below 260 K, C_{60} molecules lose two rotational degrees of freedom. Due to inequivalent molecular orientations on the Bravais sites of the fcc lattice, crystalline C_{60} undergoes a first order phase transition to a simple cubic structure. Below 90 K the time scale of the molecular rotation, $\tau > 10^3$ s. Therefore, to a measurement technique such as μ SR, where the measurement time scale $\tau \sim 10^{-6}$ s, the rotational degrees of freedom appear completely frozen.[74; 75]

The high degree of symmetry of fullerene C_{60} leads to degeneracies in the electronic states. A tight binding approximation can be used to calculate the molecular orbital levels attributable to the de-localised, π orbitals. A five-fold degenerate highest occupied molecular orbital (HOMO) and three-fold degenerate lowest unoccupied molecular orbital (LUMO) are obtained. These states contribute to the electronic transport and optical properties of C_{60} , analogous to the valence and conduction states for band semiconductors.[76]

2.6 Superconductivity

Over a century ago, the first observation of superconductivity in metals was made by H. Kamerlingh Onnes when cooling mercury to liquid He temperatures in 1911 to reveal a ‘vanishing’ resistivity at sufficiently low temperature.[77] The properties of superconductors are not limited to a zero resistance state but are also defined by the complete expulsion of magnetic flux known as the Meissner-Ochsenfeld effect. In this section, we will discuss the early phenomenological theories which successfully predict the

onset of zero resistance and perfect diamagnetism, where the relevant length scales of these effects shall be defined. The microscopic theories, describing the mechanism by which electrons in a material couple to produce these effects shall also be discussed. Finally, the manipulation of superconducting states in superconductor/ferromagnetic interfaces shall be described. Such investigations lead to a synergy between these antagonistic states of matter. The spin-triplet electron pairs and the characteristic anomalous Meissner screening observable in these systems hold great promise for spintronic research as it opens a path to ultra-low power, dissipationless spin transport.[10]

2.6.1 The London theory

The 1935 London theory was the first phenomenological model that could account for the existence of the Meissner effect. Formulated by two brothers, F. London and H. London it assumes that some fraction of the conduction electrons in a solid become superfluid while the rest remain normal.[78] Those with superfluid properties carry the supercurrent. The London equation relates the electrical current density \mathbf{j} to the magnetic vector potential \mathbf{A} by

$$\mathbf{j} = -\frac{n_s e^2}{m_e} \mathbf{A}, \quad (2.26)$$

where n_s , e and m_e is the number density, charge and mass of electrons contributing to the superconducting state. From this equation, we may consider how the magnetic field \mathbf{B} decays within a superconductor. By considering the static Maxwell equation $\nabla \times \mathbf{B} = \mu_0 \mathbf{j}$, the fact that $\nabla \times \mathbf{A} = \mathbf{B}$ and $\nabla \cdot \mathbf{B} = 0$ we obtain the following differential equation:

$$\nabla \times (\nabla \times \mathbf{B}) = -\nabla^2 \mathbf{B} = -\mu_0 \frac{n_s e^2}{m_e} \mathbf{B}. \quad (2.27)$$

The solution to which takes the form

$$\mathbf{B}(x) = \mathbf{B}_0 \exp\left(-\frac{x}{\lambda_L}\right), \quad (2.28)$$

where the London penetration length $\lambda_L = \sqrt{\left(\frac{m_e}{\mu_0 n_s e^2}\right)}$ is the length scale inside the superconductor over which the magnetic field is screened out to zero.

2.6.2 The Ginzberg-Landau theory

A second phenomenological theory of superconductivity was introduced in 1950 to describe the superconducting phase transition from a thermodynamic point of view. The theory utilises Landau's formalism for second-order phase transitions, which typically involve some change in symmetry of the system. Such phase transitions are characterised by an order parameter which is zero in the disordered state, but becomes non-zero below some critical temperature T_C as the system becomes ordered.[79] Just as for a ferromagnetic material, below its Curie temperature, some non-zero magnetisation spontaneously develops. In that case, the magnetisation, \mathbf{M} , is the suitable order parameter. Therefore, we introduce a complex superconducting order parameter, $\psi(\mathbf{r})$, which consists of some amplitude and phase and is dependent upon position. When the framework introduced by Ginzberg and Landau (G-L) was initially proposed, the significance of $\psi(\mathbf{r})$ was not easily perceived. However, it was later shown by Gor'kov that the outcomes of the G-L theory could be derived from the microscopic BCS theory of superconductivity. In Gor'kov's theoretical framework, $\psi(\mathbf{r})$ is shown to correspond to the wavefunction for the centre of mass motion for the Cooper pairs of electrons and that $|\psi(\mathbf{r})|^2$ yields the number density of superconducting states, n_s .

$\psi(\mathbf{r})$ is a complex function that goes to zero at the transition temperature, yet the free energy density of the superconducting state, $f_s(T)$, must be real. Therefore, we may Taylor expand $f_s(T)$ in terms of $|\psi(\mathbf{r})|$, taking into account the first two terms of the expansion with an extra term that accounts for the gradient in $\psi(\mathbf{r})$:

$$f_s(T) - f_n(T) = \frac{\hbar^2}{2m^*} |\nabla\psi(\mathbf{r})|^2 + a(T)|\psi(\mathbf{r})|^2 + \frac{1}{2}b(T)|\psi(\mathbf{r})|^4. \quad (2.29)$$

Here, $f_s(T)$ and $f_n(T)$ are the free energy densities ($f = F/V$) for the superconducting and normal states respectively. m^* is the mass of the superconducting charge carriers, now known to be $2m_e$. $a(T)$ and $b(T)$ are thermodynamic phenomenological parameters. In Fig. 2.3, the case where there are no gradients in the order parameter ($\psi(\mathbf{r}) = \psi$) and T is close to T_C is demonstrated. As is seen, $b(T)$ must take a positive value for there to exist some minimum in the free energy. For $a(T) > 0$

there exists some minimum in the free energy for $\psi = 0$, which is to say that the superconducting state is non-existent. Whereas for $a(T) < 0$ there are minima when $|\psi|^2 = -a(T)/b(T)$, describing the onset of a superconducting state with overall lower free energy.

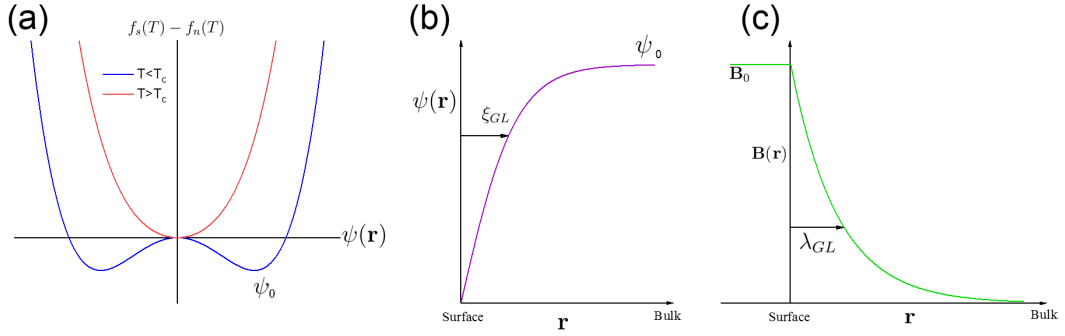


Figure 2.3: (a) The free energy $f_s - f_n$ as a function of the G-L order parameter ψ . As the derived, thermodynamic parameter $a(T)$ falls below zero at the transition temperature T_C , minima in the free energy emerge at non-zero values of ψ . (b) The recovery of ψ from the surface where the appropriate length scale is the derived G-L coherence length ξ_{GL} . (c) The decay of external field within the bulk of a superconductor over the penetration depth, λ_{GL} .

The advantage of the G-L theory is the ability to consider the case where $\psi(\mathbf{r})$ is not uniform, for example in proximity effects or in the presence of some magnetic vector potential \mathbf{A} . In these cases, the microscopic BCS theory becomes very difficult to apply, and so the macroscopic G-L theory becomes a powerful tool in analysing such phenomena. In the presence of a magnetic field, we may include a magnetic term, in the usual manner, through the substitution

$$\frac{\hbar}{i} \rightarrow \frac{\hbar}{i} - q\mathbf{A}. \quad (2.30)$$

Equation 2.29 then becomes

$$f_s(T) - f_n(T) = \frac{1}{2m^*} \left| \left(\frac{\hbar}{i} \nabla - q_s \mathbf{A} \right) \psi(\mathbf{r}) \right|^2 + a(T) |\psi(\mathbf{r})|^2 + \frac{1}{2} b(T) |\psi(\mathbf{r})|^4, \quad (2.31)$$

where the appropriate charge of the superconducting carriers, $q_s = 2e$. We may now find the condition for the minimum in free energy by performing a functional differen-

tial of the total free energy $F_s(T)$ with respect to the wavefunction, $\psi(\mathbf{r})$ and the vector potential, \mathbf{A} , which leads to the G-L differential equations:

$$-\frac{\hbar^2}{2m^*} \left(\nabla + \frac{2ei}{\hbar} \mathbf{A} \right)^2 \psi(\mathbf{r}) + (a + b|\psi|^2) \psi(\mathbf{r}) = 0 \quad (2.32)$$

$$\mathbf{j}_s = -\frac{\delta F_s}{\delta \mathbf{A}(\mathbf{r})} = -\frac{2e\hbar i}{2m^*} (\psi^* \nabla \psi - \psi \nabla \psi^*) - \frac{(2e)^2}{m^*} |\psi|^2 \mathbf{A}. \quad (2.33)$$

Solving the non-linear Schrödinger equation given in Eqn. 2.32 gives the G-L order parameter of the form $\psi(\mathbf{r}) = |\psi(\mathbf{r})|e^{i\theta(\mathbf{r})}$. Appropriate boundary conditions may be applied to both Eqn. 2.32 and Eqn. 2.33 to yield useful experimental parameters used throughout this study. The G-L coherence length, $\xi_{GL}(T)$, which defines the length scale over which $\psi(\mathbf{r})$ recovers to its full value from the surface of a superconductor. Also the G-L penetration depth, $\lambda_{GL}(T)$, which sets the length scale over which an external magnetic field decays within the superconductor, as was originally set out in the London brothers' theory. These parameters are defined as

$$\xi_{GL}(T) = \sqrt{\frac{\Phi_0}{2\pi B_{c2}}} = \sqrt{\frac{\hbar^2}{4m_e a'(T_C - T)}} \quad (2.34)$$

and

$$\lambda_{GL}(T) = \sqrt{\frac{m_e}{\mu_0 n_s e^2}} = \sqrt{\frac{m_e b}{2\mu_0 e^2 a'(T_C - T)}}, \quad (2.35)$$

where B_{c2} is the upper critical field and Φ_0 is the flux quantum. These two parameters are linked by the dimensionless G-L ratio, $\kappa = \xi_{GL}/\lambda_{GL}$. For materials with $\kappa > \frac{1}{\sqrt{2}}$, the upper critical field $B_{c2} > B_c$. For these type II materials, a mixed state forms between the two critical fields via the penetration of magnetic flux in the material in the form of Abrikosov flux vortices, each of which contains a single quantum of magnetic flux, Φ_0 . For type I materials with $\kappa < \frac{1}{\sqrt{2}}$ the upper critical field $B_{c2} < B_c$ and therefore above B_c the order parameter abruptly jumps to zero eliminating the superconducting phase. For thin film polycrystalline Nb, the material exclusively used throughout this study, typical values for ξ_{GL} extracted from transport measurements are of the order of 10 nm.[80] The penetration depth can be directly measured through muon spin rotation measurements, with typical values of $\lambda_{GL} \approx 90$ nm.[81] This gives a G-L ratio of $\kappa \approx 9$ making Nb type II.

2.6.3 Bardeen, Cooper and Schrieffer (BCS) theory

Although the phenomenological theories adequately describe the macroscopic behaviour of most superconducting condensates, the origin of superconductivity was little understood until a microscopic theory was proposed in 1957 by Bardeen, Cooper and Schrieffer.[82] Due to the coupling between electrons and phonons in the crystal lattice, the effective forces between nearby electrons can sometimes be attractive. When considering a system of two electrons outside the Fermi surface, Cooper showed that when a small attractive potential is assumed, a superposition of stable bound states (Cooper pairs) exist at an energy lower than the Fermi energy. The many-particle wavefunction describing this state, constructed by Schrieffer, has the form of a coherent state wavefunction where all the electrons near to the Fermi surface are paired up. The interpretation of this wavefunction leads to a BCS energy gap 2Δ , being the energy associated with breaking the pair into two free electrons. This energy gap, fixed at E_F , is zero at the critical temperature of the condensate. We may define Δ as[83]

$$2\Delta_{0K} = 3.53k_B T_C. \quad (2.36)$$

This relationship holds for any choice of material as long as the mechanism of the superconductivity has conventional (s-wave) symmetry. Perhaps the most critical consequence of BCS theory is the fact that this bound state of two spin 1/2 Fermions can approximately be described with Bose-Einstein statistics. As such, Cooper pairs are able to condense to the same energy level.

2.6.4 Triplet superconductivity

In a conventional BCS superconductor, electron pairs are bound by an attractive interaction, mediated by virtual lattice vibrations. Considering the symmetry of the individual spatial and spin parts of the overall wavefunction, it may seem evident that spin-singlet (anti-symmetric spin alignment) Cooper pair states will, generally, be favoured, as it allows for greater overlap of the mutually attracted electron wavefunctions. Due to the Fermionic properties of the electrons making up the Cooper pair, the anti-symmetric spin-singlet state is accompanied by a symmetric orbital wavefunction (even parity), where the orbital angular momentum $L = 0$ for s-wave symmetry and

$L = 2$ for d wave symmetry. Spin-singlet s-wave superconductivity is referred to as being conventional merely because it is the simplest form of pairing. Additionally, in the first few decades of research into superconductors, only s-wave superconductors were discovered.

It is now acknowledged that the s-wave symmetry of the bound state is not critical to the formation of the superconducting condensate. In fact, Cooper pairs need not possess total spin $S = 0$ (spin-singlet), as they can be of an $S = 1$ (spin-triplet) type. A symmetric spin-triplet state is now accompanied by an antisymmetric orbital wavefunction (odd parity), for instance with orbital angular momentum $L = 1$ (p wave). This type of spin-triplet state has been observed in several single crystal materials, the most widely understood being Sr_2RuO_4 .[\[84; 85\]](#) For these systems, the antisymmetry requirements are now satisfied through spatial asymmetry, that is, odd in orbital momentum. Unconventional p-wave superconductors, therefore, exhibit spatially anisotropic superconductivity, making them highly susceptible to crystallographic irregularities and non-magnetic scattering. To be able to utilise these exotic materials for spintronic applications, it must be possible to deposit thin films, that are rarely of single crystal quality. The very nature of the bulk p-wave SCs, therefore, limits their use within devices.

In this study, however, the type of superconductivity is of a different type to those demonstrated in the bulk unconventional superconducting materials. In 2001, Bergeret et al. considered interfaces between superconductors and ferromagnets which possess certain kinds of magnetic inhomogeneity. They demonstrated that theoretically, $S = 1$ spin-triplet correlated states can form that are symmetric in both spin and momentum. The so-called, long-range triplet component (LRTC) is less susceptible to magnetic and non-magnetic scattering. In principle, this allows a proximity induced superconducting state to form within magnetic metals. The phase coherence is now maintained over a length scale comparable to that for normal metals. For the LRTC, total wavefunction asymmetry is provided by a change in sign of the order parameter under an exchange of time coordinates, that is, odd in frequency.[\[10\]](#) This odd-frequency pairing state no longer has the same pair-breaking effect due to the internal exchange field of the ferromagnet. The generation of odd frequency spin-triplet Cooper pairs has been a

strong focus of the field of superconducting spintronics, as it provides a system where one can create dissipationless spin-polarised currents.[86]

2.7 Proximity effects

Proximity effects occur in systems where the order parameters of adjacent materials of differing long-range ordering have influence over each other. Such is the case of a ferromagnet interfaced with a normal metal where spin polarisation appears to ‘leak’ into the normal metal leading to an effective magnetisation, observable through various magnetometry techniques. A similar situation is apparent for the SC/normal-metal interface, where changes in the conductivity of the normal conductor arise due to the influence of the superconducting order parameter on the charge carriers in the normal metal. Cooper pairs penetrate the normal conductor over some length scale, retaining their superconducting properties. The extension of the superconducting order parameter into the normal conductor then reduces its strength close to the interface within the superconductor (referred to as the inverse proximity effect). The propagation of Cooper pairs into a normal metal subsequently ‘weakens’ the superconductivity, observable as a reduction in the transition temperature.

Using the G-L theory as described in Section 2.6.2, we may determine the approximate length scale over which Cooper pairs shall propagate into the normal conductor. The solution to Eqn. 2.32 takes the form $\psi(\mathbf{r}) = \psi_0 \exp(\mathbf{r}/\xi_{GL}(T))$. Within the normal metal, thermal fluctuations destroy the coherence of the Cooper pair over a length scale of ξ_{GL} . Although useful, this simplistic approach derived from the G-L theory does not fully account for the suppression of the superconducting order parameter within the superconductor via the inverse proximity effect.

In 1964, de Gennes provided a more extensive formalism to elaborate upon the diffusion of Cooper pairs in normal conductors. Similarly to the G-L theory, the length scale over which the SC order parameter decays within the normal conductor depends on the size of the Cooper pair within the normal metal. However, de Gennes’ observation was that the type of electron transport present in the conductor is critical to the penetration of Cooper pairs. That is, the effective coherence length ξ_{Eff} for a ‘clean’

system, where the electron transport is considered to be ballistic ($\xi_{Eff} > l$), is different to that of a ‘dirty’ system where the electron transport is diffusive ($\xi_{Eff} < l$). l being the electron mean free path in the metal.[87] The obtained temperature dependent coherence lengths for the two limiting cases are[88]

$$\xi_{Eff}(clean) = \frac{v_F(n)\hbar}{2\pi k_B T} \quad (2.37)$$

and

$$\xi_{Eff}(dirty) = \sqrt{\frac{D_n \hbar}{2\pi k_B T}}. \quad (2.38)$$

$D_n = v_F l / 3$ is the diffusion constant in the normal metal, with v_F being the Fermi velocity. In addition to the decay of the superconducting order parameter in the normal metal, de Gennes also defines a coherence length within the superconductor, $\xi_S = v_F(S)\hbar / 2\pi k_B T_C$, which determines how the SC order parameter changes within the superconductor and therefore how the gap energy changes at the interface. The modification of the superconducting gap, and therefore, the transition temperature, by the inverse proximity effect, provides a useful way of characterising proximity effects in S/N bilayer structures.

Key to the understanding of the superconducting proximity effect is the Andreev reflection that takes place at the microscopic level. Andreev revealed the mechanism behind the conversion of single-electron states in the normal conductor into Cooper pairs. The transfer of a single electron in the normal metal into the superconductor is allowed when the relative energy of the incoming electron is greater than the superconducting gap ($eV > \Delta$). However, if the energy of the electron is less than the superconducting gap ($eV < \Delta$), it may only transfer into the superconductor by pairing up with a second electron state to form a Cooper pair on the superconducting side. This pairing is made possible by the retro-reflection of a hole with opposite momentum to the incoming electron. The Andreev reflected hole carries phase information of the superconducting state over the previously mentioned coherence length, ξ_{Eff} . [89]

2.7.1 Superconductor-ferromagnet (S/F) proximity effects

When considering the diffusion of Cooper pairs into ferromagnetic materials, it is no longer the thermal fluctuations that destroy the phase coherence of the condensate. Instead, the presence of an internal magnetic vector potential now promotes a shifting in momentum via the Lorentz force for the oppositely aligned spin pair leading to the Cooper pair being torn apart by this so-called orbital effect. In addition, the Zeeman interaction between the internal exchange field and the electron spin favours a parallel alignment which is clearly at odds with the conventional antisymmetric spin alignment of the Cooper pair. However, as has been previously discussed in Section 2.6.4, the two states of matter are not always mutually exclusive. In 1964, Peter Fulde and Richard Ferrell [90] working independently to Anatoly Larkin and Yurii Ovchinnikov [91] (FFLO) studied the superconducting condensate under the influence of strong spin-exchange fields. In both studies, the conclusion was met that if the two opposing order parameters were to coexist, then the electron pairs must gain a non-zero centre of mass momentum. The resulting FFLO state then exhibits an inhomogeneous pair wavefunction that oscillates periodically in space. As noted by Eschrig [86], it is possible to write the evolution of a BCS state due to the action of some magnetic field.

Consider the singlet Cooper pair state:

$$|\Psi_S\rangle = \frac{1}{\sqrt{2}} (|\uparrow\downarrow\rangle - |\downarrow\uparrow\rangle). \quad (2.39)$$

At the superconductor-ferromagnet interface, an additional non-zero centre of mass momentum term \mathbf{Q} is added due to the orbital effect,

$$|\Psi_{S-F}\rangle = \frac{1}{\sqrt{2}} (|\uparrow\downarrow\rangle \exp(i\mathbf{Q} \cdot \mathbf{x}) - |\downarrow\uparrow\rangle \exp(-i\mathbf{Q} \cdot \mathbf{x})) \quad (2.40)$$

$$|\Psi_{S-F}\rangle = \frac{1}{\sqrt{2}} [(|\uparrow\downarrow\rangle - |\downarrow\uparrow\rangle) \cos(\mathbf{Q} \cdot \mathbf{x}) + i (|\uparrow\downarrow\rangle + |\downarrow\uparrow\rangle) \sin(\mathbf{Q} \cdot \mathbf{x})]. \quad (2.41)$$

It can be seen that now a singlet/triplet mixed state forms whose amplitude oscillates out of phase with each other and is the origin of the oscillating FFLO state. The triplet state that emerges from this spin mixing process is known as the

short-range triplet component (SRTC) as it has zero spin along the quantisation axis ($S_z = 0$) and is, therefore, still susceptible to the pair breaking effect of the Zeeman field.

As discussed in Section 2.6.4 it is possible to form a condensate comprising odd-frequency $S_z = 1$ spin-triplet states. In order to generate this spin aligned, triplet state, a rotation or flipping of one of the spin states in the $S_z = 0$ triplet component must occur. In the paper of Bergeret, Volkov, and Efetov the process of spin rotation is considered by introducing some magnetic inhomogeneity whereby the spin-quantisation axis spatially varies.[8] This leads to the transformation of the SRTC into the $S_z = 1$ long-range triplet component (LRTC). Where both electrons in the pair have the same spin and so are no longer affected by the Zeeman field. The length scale over which the LRTC may propagate through the ferromagnet is now determined, once again, by thermal fluctuations as in Eqn. 2.7. Fig. 2.4 summarises the generation and decay of the various superconducting correlations achievable at superconductor surfaces.

The precise nature of the magnetic inhomogeneity necessary for the creation of the LRTC is open to debate. Examples in the literature of theoretical systems that propose to support the conversion of SRTC into LRTC cover a wide range of systems. These include, but are not limited to; S/F interfaces where Bloch and Néel domain walls allow for spin rotation processes due to the non-collinearity of the magnetic moments within the domain wall[92; 93], LRTC generation in conical ferromagnets, such as holmium[94; 95] and hybrid nanostructures that contain magnetic skyrmions and vortices.[96; 97] Part of this thesis, aims to demonstrate that the highly tunable magnetic textures generated at molecular interfaces provides a novel means of the generation of spin-polarised superconducting correlations.

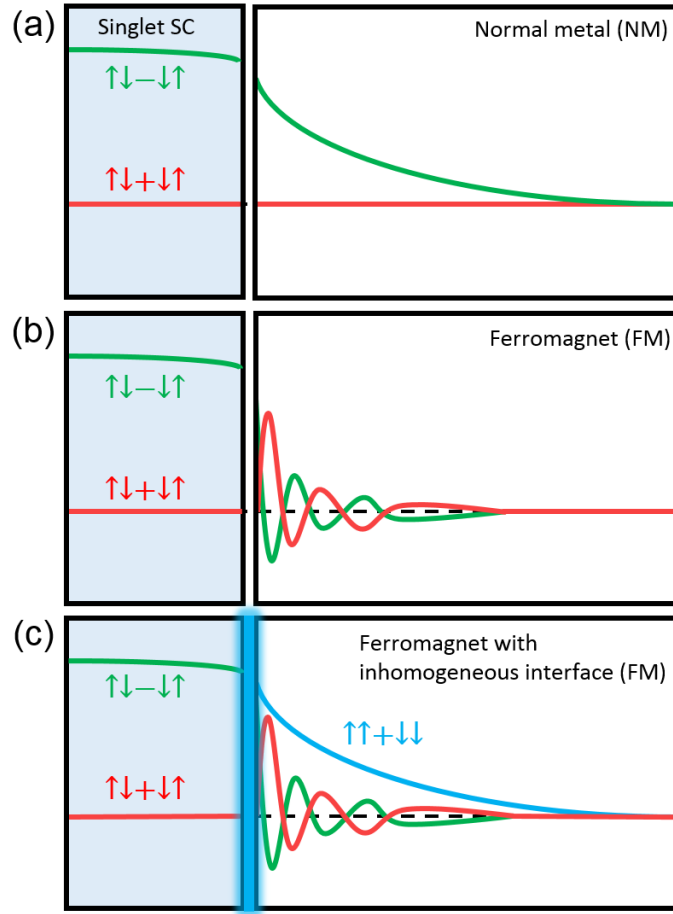


Figure 2.4: (a) Leakage of Cooper pair states into a normal metal, which causes a decrease in the Cooper pair density at the surface of the superconductor. This inverse proximity effect can be evaluated by measuring changes in the critical temperature of the condensate when interfaced with metals. (b) When interfaced with ferromagnetic interfaces a new short-range triplet component is generated. The SRTC pair amplitude oscillates out of phase with the singlet component leading to the creation of the FFLO state. (c) Where the interface between the superconductor and ferromagnet is inhomogeneous, long-range triplet correlations are generated with $S_z = \pm 1$ via a spin rotation process. Figure adapted from [86].

2.7.2 Experimental evidence of the LRTC through anomalous screening effects at S/F interfaces

From the large theoretical body of work seen in the previous sections, it is apparent the variety of systems that one may call upon to generate odd-frequency spin-triplet correlations. A key experimental aim of this thesis is the direct experimental observation of the generation of spin-triplets in hybrid molecular superconductor heterostructures. Of particular relevance to the work within this thesis is the contribution of singlet and triplet Cooper pairs towards the magnetic susceptibility of hybrid proximity structures. Theoretical studies have considered the possible Meissner state formed by singlet and triplet Cooper pairs.[98] For this, we require a sample designed to isolate the LRTCs in a normal metal. One possibility is an S/F₁/F₂/N structure where the odd-frequency triplet correlations can be turned on and off through rotation of the magnetisation vector for F₂ relative to that of F₁. In the theoretical study of Alidoust et al. when only LRTCs are present in such a device the magnetic susceptibility inside the normal metal is paramagnetic.[99] Experimentally, this effect would be difficult to measure as it requires high magnetic and spatial sensitivity. Despite this, a recent report by Di Bernardo et al. claims the observation of this anomalous Meissner effect by using the low energy muon spin rotation (LE- μ SR) technique, as outlined in Section 3.6, in an S/F/N device comprised of Nb(S), Ho(F) and Au(N). In this system, LRTCs are generated in the Au layer via spin rotation of Cooper pairs in the non-collinear Ho layer. By tuning the muon implantation depth, the magnetic susceptibility is locally probed throughout the structure (see Section 3.6 for more information). Most notably, below the T_C of the Nb film, a paramagnetic spin susceptibility is measured within the Au layer.[100] When combined with numerous other studies that focus on the rich physics observable at hybrid superconductor/ferromagnetic interfaces,[101–103] it is clear that the LE- μ SR technique provides a reliable means of characterising often unexpected magnetic effects that can occur in the near surface regions of superconducting hybrid systems.

CHAPTER 3

Experimental methods

This chapter will introduce the various techniques for sample preparation and characterisation employed throughout this study. Sample deposition was done by a combination of magnetron sputtering and *in situ* thermal sublimation. Characterisation of samples fall into the following classifications: structural morphology and elemental analysis (X-ray reflectivity XRR and transmission electron microscopy TEM), magnetometry (superconducting quantum interference device (SQUID) vibrating sample magnetometry (VSM)) and low-temperature electron transport. Synchrotron radiation techniques such as X-ray absorption spectroscopy (XAS), X-ray magnetic circular dichroism (XMCD) and X-ray magnetic linear dichroism (XMLD) were utilised for element specific magnetic characterisation. Local magnetic field distributions were probed by low energy muon spin rotation (LE- μ SR) experiments. The principles behind these techniques are addressed in this chapter. The procedures followed that are unique to this study are also highlighted.

3.1 Sample preparation

3.1.1 Sputter deposition

Throughout this project, the deposition of nanometre thick metallic films was done by DC magnetron sputtering. Sputtering is a physical vapour deposition process which utilises the elastic exchange of momentum to liberate atoms from a metallic target via bombardment with highly accelerated gaseous ions. An inert growth gas, in this case, argon, is introduced to the chamber generating a growth pressure of around 2.5 mTorr. A large DC potential difference of approximately 400 V is applied across a conductive target and shield which acts to ionise the gas. The plasma of high energy positive argon ions is then accelerated toward the cathode, or target, resulting in the steady ejection of metal atoms. These metal atoms then diffuse through the plasma to the substrate above, creating the desired metallic thin films.[104] Typically, the target materials used throughout this study are of either 99.99% or 99.999% purity. These equate to respective impurity concentrations of around 100 ppm and 10 ppm. For materials which are critical to the observed interfacial effects, particularly Nb and Cu, the higher purity of target is used. The use of higher purity niobium can, for instance, significantly improve the critical temperature of the thin film, allowing

3.1 Sample preparation

stronger screening effects to be observed.

To increase the rate of film growth from the sputtering process and to allow a stable plasma to form at lower pressures, magnetron sputtering was used. A specific arrangement of magnets within the gun, as demonstrated in Fig. 3.1, allow for a magnetic field parallel to the target's surface to be formed. Electrons that are released from the ion bombardment of the target then interact with this field via the Lorentz force. The ensuing racetrack motion of these electrons is localised near to the surface of the target, leading to an increase in the probability of ionising electron-argon collisions. The efficiency of deposition onto the substrate is then improved.[105]

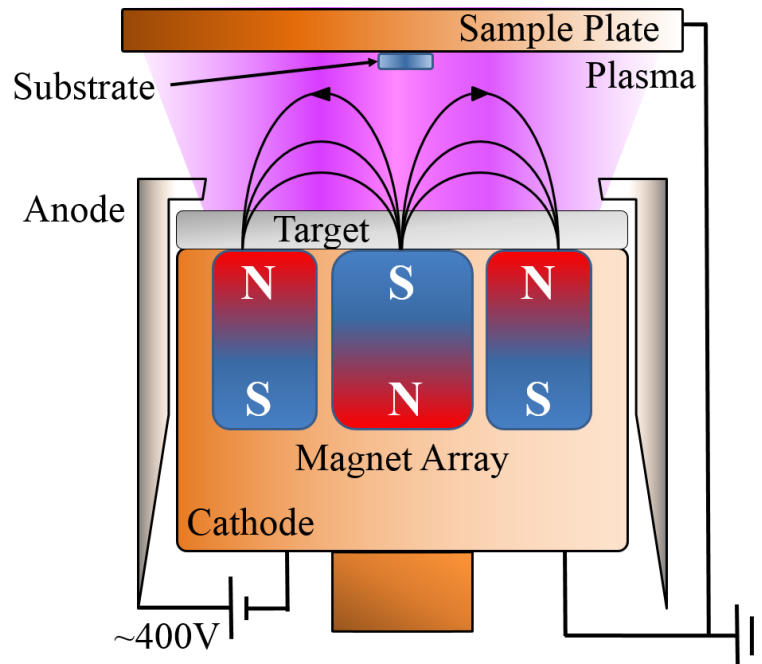


Figure 3.1: Schematic of a DC magnetron gun. A biased cathode (target) and anode (shield) generate an argon plasma which is localised to the surface of the target by the use of a toroidal magnetic field.

Our instrumentation allows for the growth of metallic and magnetic films by DC sputter deposition, insulating films by RF sources and the growth of metal oxides through plasma oxidation. Films in this study are grown at a base pressure of around 1×10^{-8} Torr, achievable by using a cryo-pump in combination with a liquid

nitrogen trap (Meissner trap). Sputter deposition of thin films in these high vacuum conditions yields highly reproducible, polycrystalline films, with interfaces that are free of oxygen. The use of shadow mask deposition in this study also allows for the fabrication of molecular tunnel junctions, photovoltaic devices and superconducting wires down to 100 μm in lateral size.

Throughout this study the following procedures are followed to ensure consistent sample growth; substrates are cleaned in an ultrasonic bath using acetone to dissolve any organic contaminants. These are then washed with isopropyl alcohol to remove residual acetone. Any remaining liquid is then removed using compressed air before the alcohol entirely evaporates. Immediately before the growth, the target material is pre-sputtered for several (~ 5 -10) minutes to remove any surface contaminants and trapped gas. This is particularly vital when growing highly reactive or porous materials.

3.1.2 Molecule sublimation

C_{60} molecular films were sublimated *in situ* to DC magnetron sputtering. The evaporation source consists of a water-cooled cover that encloses a small alumina crucible containing powdered C_{60} (99.9% purity). At atmospheric pressure, the sublimation of fullerene C_{60} takes place between 700 and 900 K. Under high vacuum conditions C_{60} sublimates at a significantly lower temperature (~ 500 -600 K at 10^{-8} Torr).[75] The molecular cage itself is remarkably stable up to very high temperatures. Isolated C_{60} cages will refrain from coalescing until roughly 1500 K.[106] The large disparity between the interatomic and intermolecular bonding strengths make C_{60} particularly robust over this large temperature range. In our high vacuum deposition system, molecular sublimation is achieved by resistively heating a tungsten coil with a current of around 21 A. An aperture on top of the copper cover allows the C_{60} vapour to pass through and condense onto the substrate above.

The deposition rate of the vapour C_{60} upon the substrate was tracked by a crystal rate monitor. The resonant frequency of a quartz crystal, positioned above the C_{60} source, alters from the adsorption of C_{60} onto its surface. The change in frequency is

3.1 Sample preparation

then processed into a time-averaged growth rate and film thickness by the rate monitor. A tooling factor allows for the calibration of the instrument, whose value accounts for the differences in distance between the crucible and the quartz/substrate. As demonstrated in Fig. 3.2(a), cross-sectional transmission electron microscopy (TEM) images of multi-layered films grown using these methods show continuous layers with minimal inter-diffusion of around 1-2 nm when metal is sputtered on C_{60} . Fast Fourier transform (FFT) analysis shows areas of sharp contrast in the diffraction pattern due to regions of face centred cubic (FCC) texture in the molecular layer. Fig. 3.2(b) provides X-ray diffraction (XRD) confirmation of the FCC texture present in a C_{60} film via the measurement of the [111] peak.

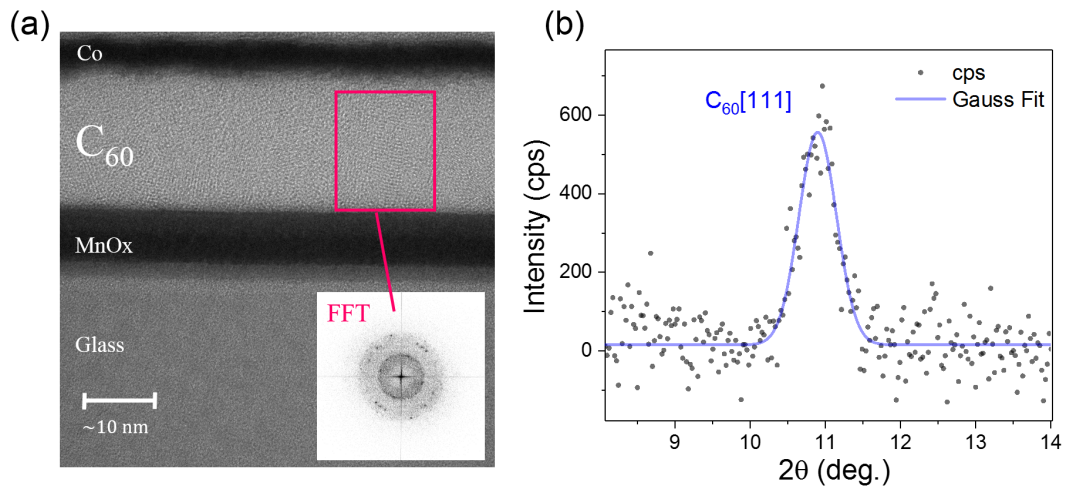


Figure 3.2: (a) Cross-sectional TEM image of a typical device structure used to study the photovoltaic properties of the MnO_x/C_{60} interface. Inset: fast Fourier transform of the region indicated shows the presence of sharp peaks in the diffraction pattern due to nano-crystalline grains found in the sublimated C_{60} . (b) XRD measurements of a C_{60} film shows the presence (with very low intensity) of the [111] peak for molecular C_{60} with some FCC texture. Fitting this peak yields the expected inter-molecular spacing ($a = 1.404 \pm 0.003$ nm) via Bragg's law and an out of plane crystallite grain size of 15.9 ± 0.6 nm through fitting with the Scherrer equation.

Unlike other molecular species, C_{60} is relatively stable under ambient conditions. Irreversible oxidation of C_{60} can occur if heated in the presence of oxygen above 473 K where the cage will begin to break down.[107; 108] Below this temperature the intercalation of molecular oxygen into crystalline C_{60} may occur. This is not a problem unless

the film is illuminated, as a photo-assisted oxidation process will happen where the O₂-C₆₀ reaction produces CO, CO₂ and various amorphous graphite-like residue.[109] It is therefore vital that throughout this study samples of C₆₀ are sufficiently capped with thick (~ 3-15 nm) metallic surface layers that prevent the intercalation of molecular oxidation but also minimise any photo-induced oxidation processes.

3.2 X-ray reflectivity

Spin-dependent phenomena that emerge at molecular interfaces can have strong dependences on structural morphology. It is vital then that the morphology of thin film systems can be consistently characterised. Throughout this study, structural parameters are obtained using a low angle X-ray reflectivity technique. XRR relies on the reflection of electromagnetic waves off surfaces with sudden changes in electron density. Sensitivity to inter-atomic separation requires wavelengths in the 10⁻¹⁰ meters. This is obtainable through core-hole recombination in copper targets via bombardment with an accelerated electron source. The deceleration of electrons in the target material produces a broad distribution of radiation known as Bremsstrahlung radiation while the recombination of core holes with outer-shell electrons produces characteristic X-ray emission. Specifically, the transition of a 2p electron from the n = 2 (L) shell to the n = 1 (K) shell gives rise to the Cu K α line with a wavelength of 1.54 Å. This emission line is commonly used in lab-based reflectivity techniques.

For X-rays, the refractive index is conventionally written as a small perturbation, δ , from unity:[110]

$$n = 1 - \delta. \quad (3.1)$$

δ can be rewritten as

$$\delta = \frac{2\pi\rho r_0}{k^2}, \quad (3.2)$$

where ρ is the electron density, r_0 is the Bohr radius and k is the wave vector for the incoming photon.

The incident grazing angle θ is related to the refracted angle θ' from Snell's law:

$$\cos \theta = n \cos \theta'. \quad (3.3)$$

For an index of refraction that is less than unity, there exists a critical angle, θ_C , below which X-rays undergo total external reflection. Expanding the cosine in Eq.(3.3) with $\theta = \theta_C$ and $\theta' = 0$ yields a relation between δ and the critical angle θ_C :

$$\theta_C = \sqrt{2\delta} = \sqrt{\frac{4\pi\rho r_0}{k^2}}. \quad (3.4)$$

θ_C can provide information about the electron density, ρ , of the measured material.[111; 112]

Beyond the critical angle, θ_C , the measured reflected intensity rapidly falls as X-rays become internally reflected. An oscillatory dependence on the measured intensity with incident angle then becomes apparent due to the constructive and destructive interference of X-rays reflected off the top and bottom surfaces of a film with thickness, t . The occurring phase shift of the two waves has an angular dependence and produces peaks in intensity (θ_i). The angular dependence of the so-called Kiessig fringes is given by

$$\lambda = 2t\sqrt{\sin^2 \theta_i - \sin^2 \theta_C}, \quad (3.5)$$

where i is an integer, λ is the wavelength and θ_C is the position of the constructive peaks.[113] Clearly, in real systems the surfaces are not atomically flat and so diffuse scattering off these surfaces leads to an angular dependence in the reduction of intensity. XRR curves of calibration samples may be fitted using the Kiessig function or using GenX software for multi-layered structures.[114] As demonstrated in Fig. 3.3, information about the structural morphology of metallic and molecular films can be obtained using this technique.

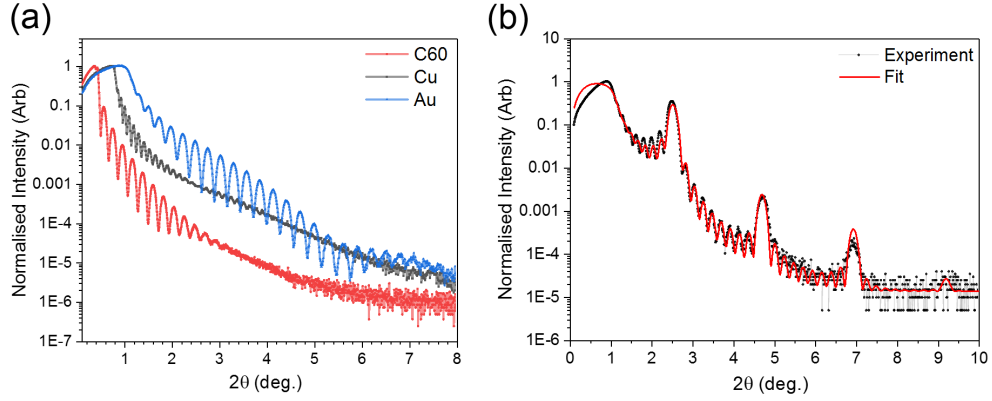


Figure 3.3: (a) XRR measurements of single films of C₆₀ (39.2 ± 0.3 nm), Cu (62.0 ± 0.2 nm) and Au (30.5 ± 0.3 nm). The dependence of the critical angle, θ_C upon the density of the material is observable in this figure. (b) The XRR of a [Co(16.8 ± 0.1 Å / Pt(21.8 ± 0.2 Å)] $\times 10$ multilayer is shown. The rms roughnesses obtained for the Co and Pt layers are 2.9 ± 0.3 Å and 4.7 ± 0.9 Å respectively. The thickness of the single films was determined using the Kiessig equation, whereas the multilayer fit (shown in red) has been generated using the GenX fitting software.

3.3 SQUID VSM magnetometry

In this study, the emergent magnetic effects in metal/fullerene films are anticipated to be very small due to the magnetism being highly localised to the interfaces. In a 4×4 mm² sample, a magnetic moment of the order of 10^{-6} emu can be expected. Therefore, the high resolution of a system such as a superconducting quantum interference device (SQUID) vibrating sample magnetometer (VSM) is required. Fig. 3.4 schematically demonstrates how a SQUID device is inductively coupled to VSM electronics allowing a resolution $\leq 10^{-8}$ emu.

A magnetic film oscillating at around 14 Hz induces a current within a set of superconducting (SC) detection coils according to Faraday's law. The detection coils are configured as a second order gradiometer to reduce signals from external field disturbances. These detection coils are then inductively coupled to a SQUID via a flux transformer.[115] The SQUID consists of a superconducting ring with two weak links that have a critical current I_J smaller than the rest of the loop, otherwise known as

3.4 Raman and photoluminescence measurements

Josephson junctions. A constant measurement current is applied by the SQUID head which travels in opposite directions around the loop. When a magnetic field is then applied to the SQUID, the critical current of both weak links I_C has an oscillatory response to the external flux ϕ : [116; 117]

$$I_c = 2I_J \left| \cos \left(\pi \frac{\phi}{\phi_o} \right) \right| \quad (3.6)$$

The effect is analogous to Young's double slit experiment where the signal has a period, hence resolution, of one flux quantum $\phi_o = h/2e$. The resulting oscillating voltage signal that is produced due to the change in phase across the two junctions allow the SQUID to be used as a highly sensitive magnetometer.

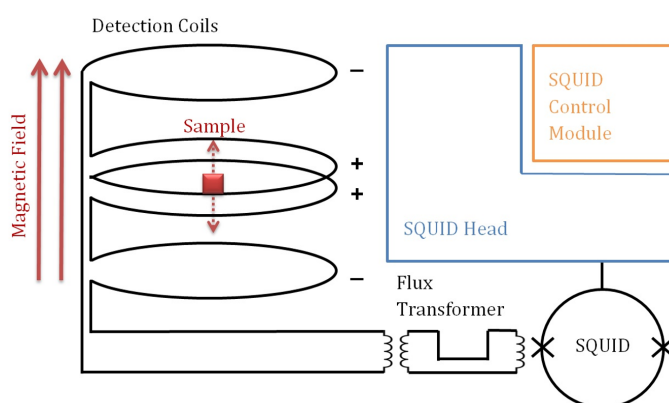


Figure 3.4: A simplified schematic of the SQUID detection system found within the Quantum Design Magnetic Properties Measurement System. A small ($4 \times 4 \text{ mm}^2$) magnetic sample is vibrated at 14 Hz with an oscillation amplitude of 5 mm. The use of a superconducting quantum interference device coupled to superconducting detection coils allows high-resolution measurement of the properties of magnetic thin films.

3.4 Raman and photoluminescence measurements

In this research, photoluminescence (PL) and Raman scattering measurements provide optical characterisation of the molecular C_{60} films. These are performed using a Horiba LabRam HR800 Raman microscope, where three possible laser frequencies are available for illuminating samples; 633 nm (red), 532 nm (green) and 473 nm (blue). For higher energy laser sources, care must be taken against non-reversible degradation

3.4 Raman and photoluminescence measurements

of the molecules by photo-induced chemical changes. Illumination of materials whose energy band gaps are comparable to that of visible light produces excited electron-hole pairs that are bound to each other by Coulomb interaction. The e-h pair is considered to be a quasi-particle known as an exciton. For molecular systems, like C_{60} , where a tight binding model more appropriately describes the energy states, the electron-hole pair will be highly localised. Consequently, a strong electrostatic attraction will act to lower the energy of the excitation, such that it lies between the band-gap. This attractive term accounts for the discrepancy between the observed optical bandgap (1.69 eV as shown in Fig. 3.5(a)) and that measured by photoemission spectroscopy (2.3 eV).[118; 119] This is known as a Frenkel exciton and exists in many poorly screened and localised systems. Singlet and triplet exciton states can be formed with total spin $S = 0$ (spins anti-aligned in the HOMO and LUMO) and $S = 1$ (spins aligned in the HOMO and LUMO) respectively. Since the recombination of electron and hole pairs of the same spin polarity is forbidden, triplet excitons require a spin flip mechanism in order to recombine. The lifetime of the triplet Frenkel exciton state is, therefore, many orders of magnitude higher (\sim ms) than that of the singlet state (\sim ns). As a result, triplet exciton states lead to reduced photoemission due to longer recombination times or intersystem crossing with non-radiative decay.[120]

Raman scattering uses the inelastic scattering of electrons by a monochromatic light source. These electrons are coupled to vibrational modes of molecules to give energy transitions that are either; of the same initial frequency (elastic Rayleigh scattering), of a larger frequency (inelastic Stokes scattering) or a lesser frequency (inelastic Anti-Stokes scattering). C_{60} has 10 Raman active vibrational modes which can be shifted or quenched through charge or even spin doping of the molecule.[121] For these reasons, Raman spectral analysis of C_{60} based thin films acts as a powerful characterisation tool to monitor the quality of molecular thin films. For example, in the event of photo-induced polymerisation, the prominent pentagonal pinch mode ($A_g(2)$), as seen in Fig. 3.5(b), is significantly suppressed. The optical spectra of C_{60} is highly sensitive to a variety of external factors, such as electric and magnetic fields, temperature changes and the trapping of exciton states.[75] Raman and PL measurements can, therefore, provide a deterministic probe of the modifications to the molecule during device operation.

3.5 X-ray absorption spectroscopy and magnetic dichroism

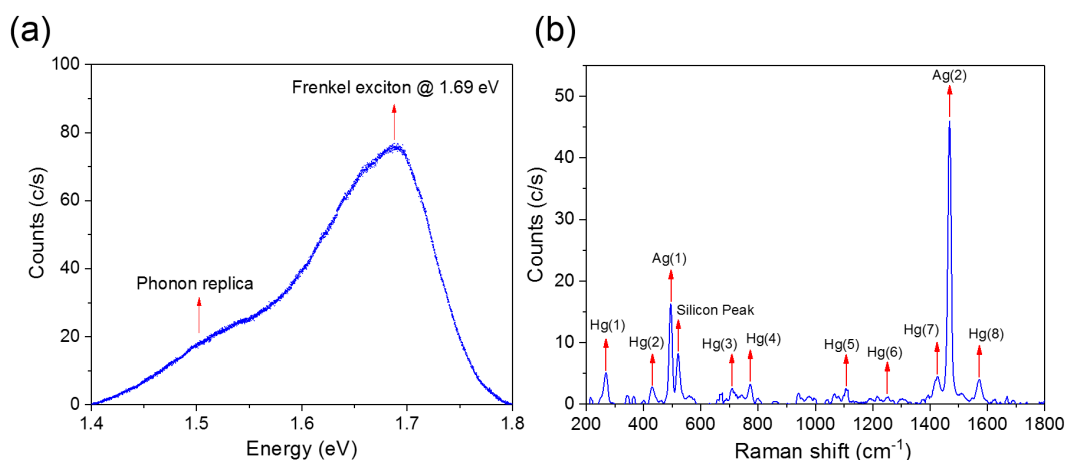


Figure 3.5: The typical PL and Raman spectrum for fullerene C_{60} . a) In the PL spectrum, the 1.69 eV feature corresponds to the zero-phonon line for the recombination of the C_{60} Frenkel exciton. Phonon-assisted recombination occurs at lower energies, such as that which has been labelled at 1.5 eV. The fluorescence background has been subtracted from this data. b) The Raman active vibrational modes for a thick (~ 100 nm) C_{60} film. The relative intensity of the Raman peaks is governed by the change in polarisability associated with that vibrational mode.

3.5 X-ray absorption spectroscopy and magnetic dichroism

Synchrotron techniques have been used throughout this research to study interfacial hybridisation effects and emergent magnetic phenomena. X-ray absorption spectroscopy (XAS) measurements probe the energy-dependent absorption of light, tuned to the transition of core-shell electrons into unoccupied states. This provides information about the band or orbital structure of a material and allows the elemental composition to be obtained. In the case of 3d metals, X-rays are tuned to specific energy transitions, exciting electrons from core p (L edge) or s (K edge) orbitals into the valence shell. A small bias present between the sample and detection equipment collects the photoelectron drain current in a total electron yield (TEY) configuration. Because the TEY method requires the collection of free electrons released during Auger cascade in the molecular film, the signal produced is highly surface sensitive.

3.5 X-ray absorption spectroscopy and magnetic dichroism

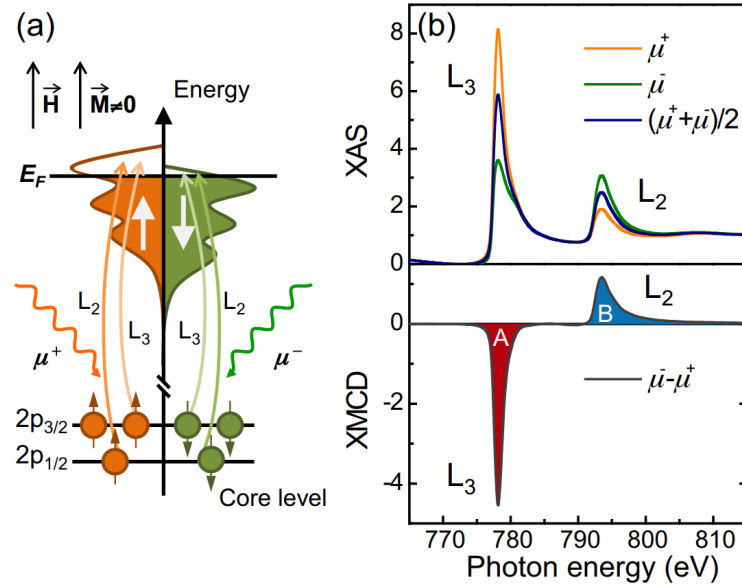


Figure 3.6: (a) The XAS for a 3d metal is obtained through the excitation of electrons from the core 2p states into unoccupied states in the 3d band. (b) The statistically favourable excitation from the $j = 3/2$ 2p state leads to the larger L_3 edge whereas an excitation from the $j = 1/2$ 2p state leads to the L_2 edge. If the valence 3d band has a majority spin population, the difference in XAS for opposite polarisations ($\mu^- - \mu^+$) leads to an element-specific XMCD spectrum as seen for Co in the bottom panel. As the light only interacts with the orbital part of the electron wavefunction, as opposed to the spin part, the opposite dichroism is obtained for the L_3 edge (spin and orbit aligned parallel) compared to that of the L_2 edge (spin and orbit aligned antiparallel). The integrated XMCD signal can be analysed with the sum rules to separate the spin and orbital contributions to the total magnetic moment. Figure taken from [122])

For the study of magnetic phenomena, the effect of X-ray magnetic circular dichroism (XMCD) can be utilised. Dichroism refers to the polarisation-dependent absorption of light. XMCD, therefore, provides element-specific magnetic characterisation. An XMCD spectrum is obtained as the difference of two absorption spectra, using light whose circular polarisation vectors lie parallel and antiparallel to the magnetisation vector of a material. XMCD can be described as a two-step process, demonstrated in Fig. 3.6 for the case of metallic L_2 and L_3 edges. 2p core states are split into two energy levels due to the spin-orbit interaction. A $j = 3/2$ and $j = 1/2$ level exists due to the spin and orbit being coupled parallel and antiparallel respectively. First, light with a helicity vector parallel (antiparallel) to the 2p orbital

3.6 Low energy muon spin rotation (LE- μ SR)

moment excites electrons with up (down) spin orientation. Secondly, these electrons occupy a spin 3d band according to their original spin angular momentum. A difference between the two spectra (dichroism) then exists if the 3d electrons have a majority spin polarisation.[122]

For the case of organic molecular X-ray spectroscopy, where the occupation of carbon extends only into the 2p orbital, we instead study the carbon K edge. Derived from transitions from the 1s orbital to the LUMO and higher energy levels, XAS of carbon-based molecules can yield valuable information on orbital occupation and the generation of hybridised orbitals. The linear polarisation dependence of the absorption (XLD) into the unoccupied orbitals can inform upon the orientation of specific orbitals relative to the light polarisation.[123]

XAS measurements in hybrid transition metal-C₆₀ samples demand soft (<2 keV) X-ray light of high brilliance to achieve the appropriate excitations in the 3d metal and carbon samples. As such, synchrotron radiation was required. XAS, XMCD and XLD measurements were, therefore, taken at the ALBA synchrotron facility in Barcelona, Spain. Synchrotron sources produce a broad spectrum of high flux radiation where a complex series of diffraction gratings produce a variable monochromatic beam. The measurement is undertaken in a pressure of 10⁻¹⁰ Torr to minimise the scattering of soft energy X-rays with air. The active junction area for all samples used for XAS measurements was 100×100 μm^2 . The monochromated beam was, therefore, collimated by variable focusing bender mirrors to an area of approximately 100×50 μm^2 . This allows for the precise triangulation of the device centre and the attribution of the observed carbon K edge to the device's molecular barrier.

3.6 Low energy muon spin rotation (LE- μ SR)

The muon is an elementary spin $\frac{1}{2}$ particle that is used to study the microscopic landscape of magnetic texture within a variety of materials.[124–126] For muon spin rotation it is the positive muon that is used. The positive muon occupies interstitial sites in the crystal lattice. As such, it has a greater sensitivity to magnetic phenomena by probing areas of larger electron density. Although the muon has a mass of around

3.6 Low energy muon spin rotation (LE- μ SR)

207 times that of an electron, it is more useful to consider it as a light proton. Nevertheless, the magnetic moment is approximately 3.2 times that of a proton, making it particularly sensitive to magnetic centres. In muon spin rotation experiments it is the depolarisation and precession of the μ^+ magnetic moment that is evaluated.

At facilities such as the Paul Scherrer Institute (PSI), muons are created from the bombardment of protons (p) into a light target, usually graphite, that produces pions (π^+) and neutrons (n) via the reaction



The pion subsequently undergoes a rapid, within 26 ns, decay into muons (μ^+):



where ν_μ is a muon-neutrino. As a two-body process, the pion decay is a relatively simple process. To conserve momentum in the π^+ rest frame, the muon and neutrino must have equal and opposite momentum. Also, as a consequence of the π^+ being a spin zero particle and the neutrino having a negative helicity (its spin is aligned antiparallel to its momentum), the muon must also have a negative helicity. Therefore, it is entirely possible to generate a beam of nearly 100% spin-polarised muons by selecting those muons which stop at the target surface and are thus at rest at the time of decay.

Muons are stopped in the sample of interest and decay after some time t , with a probability $P \propto \exp(-t/\tau_\mu)$, where τ_μ is the lifetime of the muon = 2.2 μ s. The decay is a three-body process:



As shown in Fig. 3.7(b) the μ^+ decay does not conserve parity. A positron shall predominantly be emitted along the muon spin vector direction, at the time of decay. Through the measurement of the emitted positron trajectory, the time evolution of the muon spin polarisation within our material can be evaluated.

3.6 Low energy muon spin rotation (LE- μ SR)

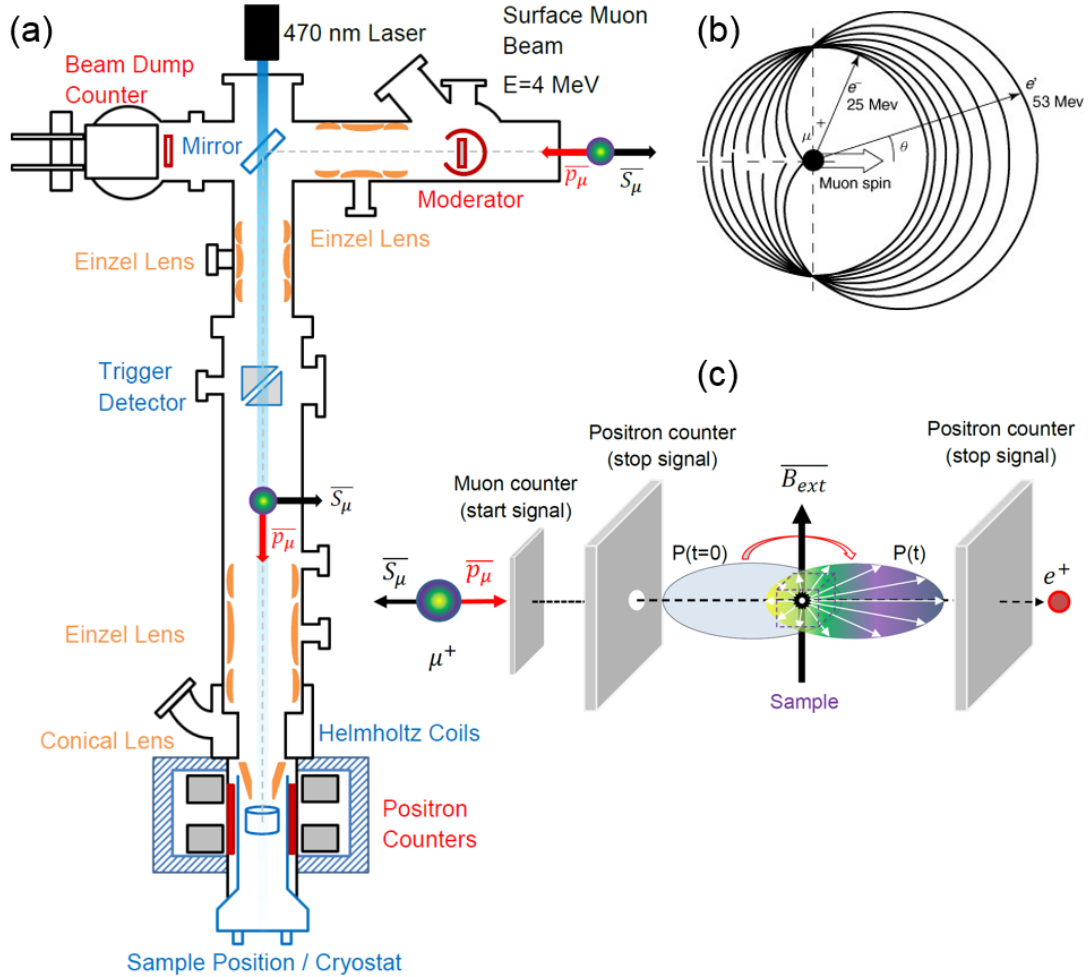


Figure 3.7: (a) The low energy muon beamline at PSI which utilises a moderation technique to generate a spin-polarised muon beam, with a kinetic energy of around 15 keV. It is shown how a laser may be incorporated into the experiment to perform μ SR with optical irradiation (see Chapter 4). (b) The angular distribution of emitted positrons is shown as a function of the energy of the emitted positron. The tendency for the emission trajectory to be parallel to the muon spin direction is greatest for the highest energy emitted positrons. (c) The experimental geometry of a muon spin rotation experiment in an externally applied transverse field B_{ext} is shown in this schematic. p_μ and S_μ represent the muon momentum and spin vectors. Figures adapted from [127; 128])

3.6 Low energy muon spin rotation (LE- μ SR)

The kinetic energy of the muons that are produced by proton bombardment processes as described above is around 4.1 MeV. This is equivalent to an implantation depth of the order of mm. This, therefore, limits the conventional muon production method to the study of bulk materials rather than thin films. This is not the case at PSI, however, where a moderation technique is utilised to produce a tunable beam of muons between roughly 0.5 keV to 25 keV. The technique, unique to the Swiss muon source, allows the study of depth dependences upon magnetic effects in thin films.[129] A schematic of the low energy muon beamline is shown in Fig. 3.7.

The moderator consists of a thin (125 μ m) silver foil that is cooled to 10 K in a 10^{-10} mbar base pressure. Argon is then condensed onto the foil to a thickness of nearly 20 nm and is protected by a solid 1.2 nm film of condensed nitrogen. A portion of muons passing through the moderator is decelerated from an initial kinetic energy of 4 MeV to around 15 eV whilst retaining their spin polarisation. After being accelerated in a potential of 15 kV, the beam is directed towards the sample by a 90° electrostatic mirror. Muons that have not been successfully moderated and possess greater energy will pass through the mirror and shall be counted by the beam dump positron counter. The implantation energy of the muons can then be altered with the application of a potential applied to the sample plate.

The beam is focussed by a series of electrostatic lenses. Einzel lenses focus the beam without changing its energy whilst the conical lens focuses the beam toward the sample. Each muon that passes into the sample chamber passes through a 10 nm carbon foil at the trigger detector. The resulting scintillation sets off a timer with nanosecond resolution. If the muon decays instantly, then the positron shall be emitted toward a backward detector, as dictated by the spin vector of the muon. If instead, the muon lives long enough to undergo half a precession, it shall be emitted toward a forward detector. By timing an ensemble of positron detection events in forward ($N_F(t)$) and back ($N_B(t)$) detectors, we may describe the time evolution of the muon polarisation, $P(t)$, through an Asymmetry function:

$$A(t) = \frac{N_B(t) - N_F(t)}{N_B(t) + N_F(t)}. \quad (3.10)$$

3.6 Low energy muon spin rotation (LE- μ SR)

We then model the μ SR signal with the program *musrfit*.[\[130\]](#) A software package developed at PSI for the fitting of μ SR spectra according to various decay models.

3.6.1 Muonium formation

In metallic systems with high carrier concentrations, the conduction electrons screen the positive charge of the muon forming an electron cloud around the muon of a size dictated by the Thomas-Fermi screening length. Therefore in metals, we need only consider the precession of the diamagnetic μ^+ around internal or applied magnetic fields and their depolarisation due to internal field distributions and nuclear moments. In insulating and semiconducting systems, the picture becomes somewhat more complex, however. As there is a lack of screening electrons, the muon can thermalise and generate a hydrogen-like atomic bound state by picking up an electron. This paramagnetic isotope of hydrogen is called muonium ($\text{Mu} = \mu^+e^-$).

Eigenvector	Eigenvalue
$ \Psi_1\rangle = \uparrow_\mu\uparrow_e\rangle$	$E_1/\hbar = \frac{1}{4}[A_{xx} + A_{yy} + A_{zz}](1 + 2m\mathbf{B}/B_0)$
$ \Psi_2\rangle = \alpha \uparrow_\mu\downarrow_e\rangle + \beta \downarrow_\mu\uparrow_e\rangle$	$E_2/\hbar = -\frac{1}{4}[A_{xx} + A_{yy} + A_{zz}](1 - 2\sqrt{1 + (\mathbf{B}/B_0)^2})$
$ \Psi_3\rangle = \downarrow_\mu\downarrow_e\rangle$	$E_3/\hbar = \frac{1}{4}[A_{xx} + A_{yy} + A_{zz}](1 - 2m\mathbf{B}/B_0)$
$ \Psi_4\rangle = \beta \uparrow_\mu\downarrow_e\rangle - \alpha \downarrow_\mu\uparrow_e\rangle$	$E_4/\hbar = -\frac{1}{4}[A_{xx} + A_{yy} + A_{zz}](1 + 2\sqrt{1 + (\mathbf{B}/B_0)^2})$
$B_0 = A_H/(\gamma_\mu + \gamma_e)$ $m = \frac{(\gamma_e - \gamma_\mu)}{(\gamma_\mu + \gamma_e)} \approx 0.9904$	
$\alpha = [1/\sqrt{2}]\sqrt{1 - [(\mathbf{B}/B_0)/\sqrt{1 + (\mathbf{B}/B_0)^2}]}$ $\beta = [1/\sqrt{2}]\sqrt{1 + [(\mathbf{B}/B_0)/\sqrt{1 + (\mathbf{B}/B_0)^2}]}$	

Table 3.1: The calculated eigenvectors and eigenvalues for isotropic muonium in an applied magnetic field, \mathbf{B} .

3.6 Low energy muon spin rotation (LE- μ SR)

As Mu is a system of two spin $\frac{1}{2}$ particles, the electron spin and muon spin are coupled by a hyperfine interaction. The Hamiltonian for which can be written in terms of angular frequency:

$$\frac{H}{\hbar} = -\gamma_{\mu}\mathbf{S}^{\mu} \cdot \mathbf{B} + \gamma_e\mathbf{S}^e \cdot \mathbf{B} + \mathbf{S}^{\mu} \cdot A \cdot \mathbf{S}^e, \quad (3.11)$$

where \mathbf{S}^{μ} and \mathbf{S}^e are the respective muon and electron spin operators, γ_{μ} and γ_e are the gyromagnetic ratios for the electron and muon, A is the hyperfine coupling tensor and \mathbf{B} is the magnetic field.[131; 132]. The eigenvectors and eigenvalues can be calculated for this Hamiltonian, the results of which are displayed in table 3.1. As can be seen from these solutions, for an isotropic hyperfine tensor ($A_{xx} = A_{yy} = A_{zz}$), two states exist in zero field: a singlet and a degenerate triplet state.

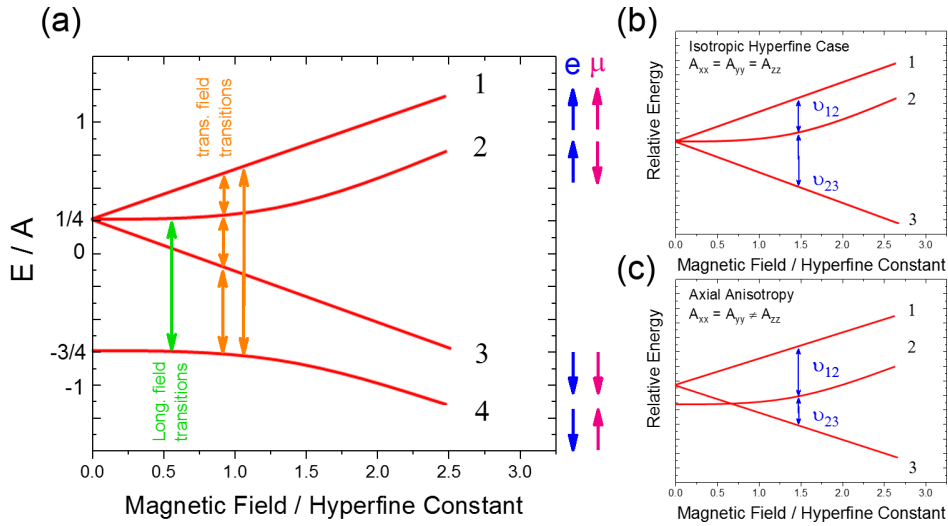


Figure 3.8: (a) The Breit-Rabi diagram for isotropic muonium is shown where two energy levels exist in zero field. The application of a magnetic field splits the higher energy triplet state which then evolves with field as is shown. Transitions between hyperfine energy levels exist in transverse and longitudinal applied fields with characteristic frequencies, ν_{ij} . For the completely isotropic hyperfine case in (b), no measurable muonium frequency will exist in zero field. For the anisotropic hyperfine case in (c) however, there will exist some transition probability between non-degenerate triplet states in zero field due to the unequal diagonal components of the hyperfine tensor, A_{ii} .

Fig. 3.8 demonstrates the electron and muon spin configurations for these states and the field dependence of the hyperfine levels as a Breit-Rabi diagram. The application of a magnetic field lifts the degeneracy of the triplet state and then transitions between energy levels can be observed as a precession frequency ν_{ij} which is equal to the splitting between energy levels $(E_i - E_j)/\hbar$. The splitting between the zero field (ZF) states is equal to the hyperfine coupling constant $A_H = 2\pi \times 4463$ MHz. This frequency would be unobservable in a typical μ SR experiment. Therefore, it is expected that no oscillation should be observed in the isotropic hyperfine case. If, however, some axial asymmetry is introduced into the hyperfine tensor, then the degeneracy of the triplet state is lifted as in Fig. 3.8(c), where a single frequency can now be expected in the absence of magnetic field.

3.6.2 Characterisation of the muonium state in thin film C₆₀

The characteristic ZF muonium oscillation data for a thick (~ 200 nm) C₆₀ film, measured at 300 and 40 K, is shown in Fig. 3.9. The data has been fitted by a multiple frequency model, where an individual precession frequency ν_i has a contribution to the muon polarisation, $P(t)$, given by

$$P = A_i \exp(-\lambda t) \cos(2\pi\nu_i t), \quad (3.12)$$

where λ describes the depolarisation rate of a muon/muonium state precessing at a frequency ν_i . The Asymmetry, A_i , is then a measure of the fraction of signal one may attribute to the given precession.

3.6 Low energy muon spin rotation (LE- μ SR)

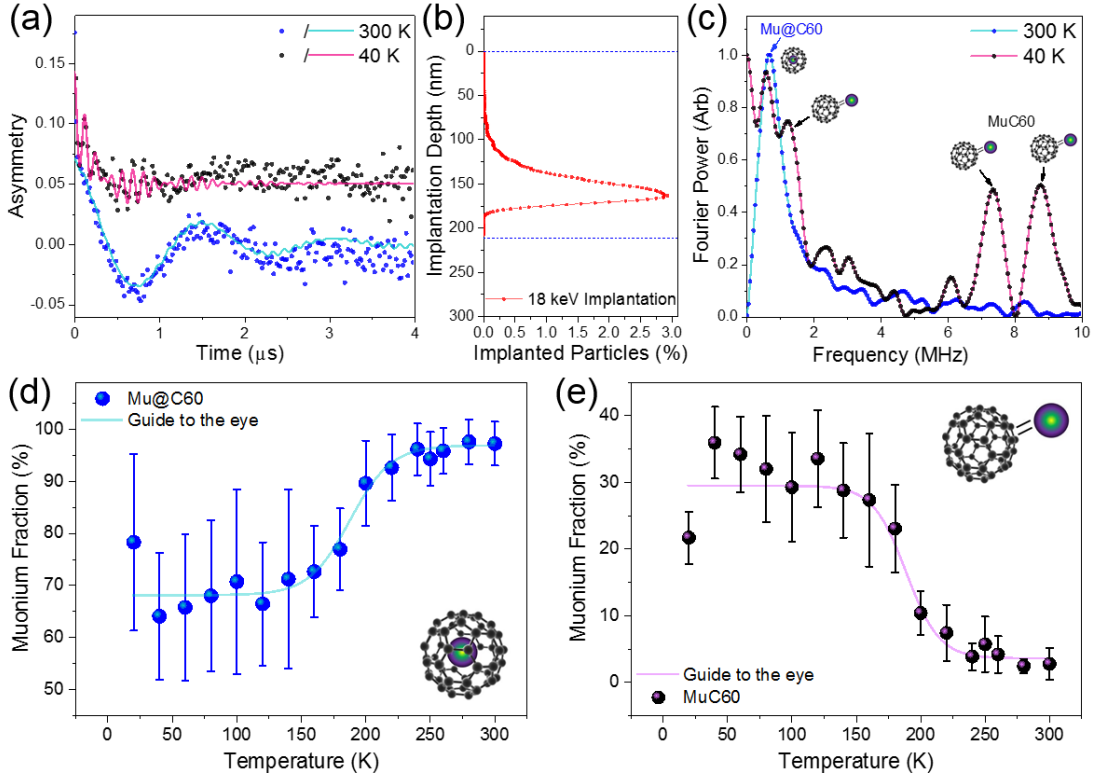


Figure 3.9: The time evolution of the muon spin polarisation is shown for a plain C₆₀ (210 nm thick) film on a Si/SiO₂ substrate in (a). The asymmetry function describing the muonium precession is shown for 40 and 300 K. The depth dependence of the muon implantation for these measurements is shown in (b). The Fourier transform of the time domain asymmetry data is shown in (c), where it can be seen that a single low-frequency line exists of around 0.6 MHz at room temperature. We attribute this frequency to the endohedral Mu@C₆₀ state. At lower temperature, as the rotational degrees of freedom for the molecule freeze out, three additional frequencies emerge that are associated with the C₆₀ muonium radical (MuC₆₀; 1.2, 7.4 and 8.6 MHz). (d) and (e) show the respective temperature dependence of the measured muonium fraction for the endohedral Mu@C₆₀ and radical MuC₆₀ lines.

At low temperatures (below 90 K), the rotational motion of the C₆₀ slows down (see Section 2.5). At these temperatures, oscillations at 1.2 MHz, 7.4 MHz and 8.6 MHz are visible. These frequencies are well understood and are attributed to the completely anisotropic hyperfine interaction of the exohedral radical muonium state (MuC₆₀).[133; 134]. These frequencies are only present when the time scale of the molecular rotation is of the same order as the muon lifetime ($\sim 2.2 \mu\text{s}$). In addition

3.6 Low energy muon spin rotation (LE- μ SR)

to the MuC_{60} radical precession, we observe an additional low-frequency precession that persists up to room temperature. This has not been reported in the various studies of bulk crystalline C_{60} fullerite.[134–136] However, it is seen in all of the thin fullerene films grown throughout this study. The observed muonium state has also been shown to be sensitive to magnetic surface states induced at transition metal/fullerene interfaces.[21; 65] The presence of this low-frequency ZF oscillation infers some intrinsic distortion of the fullerene cages. A molecule such as C_{70} possesses an inherent uniaxial anisotropy due to the symmetry of the molecule's elongated shape. A low-frequency precession has therefore been reported, observable at 0.7 MHz, and attributed to an endohedral Mu@C_{70} state.[137; 138]

With the absence of a magnetic field, hence Zeeman splitting, the hyperfine Hamiltonian for anisotropic muonium is simply

$$H_{HF} = \mathbf{S}^e \cdot A \cdot \mathbf{S}^\mu. \quad (3.13)$$

\mathbf{S}^e and \mathbf{S}^μ are the spin operators of the respective electron and muon. A is a tensor with diagonal components A_{xx} , A_{yy} and A_{zz} . The associated frequencies of the muonium oscillations in zero field are then given by

$$\nu_{12} = \frac{A_{zz} - A_{yy}}{2h}, \nu_{13} = \frac{A_{yy} - A_{xx}}{2h}, \nu_{23} = \frac{A_{zz} - A_{xx}}{2h}. \quad (3.14)$$

For a completely anisotropic A where $A_{xx} \neq A_{yy} \neq A_{zz}$, three zero field oscillations will be observed. Such is the case for the MuC_{60} radical precession as previously reported.[133; 134] It is also possible to obtain a single frequency for an axially symmetric A where ($A_{xx} = A_{yy} \neq A_{zz}$). We accordingly attribute the low-frequency oscillation seen in our films to an axially symmetric hyperfine interaction for an endohedral Mu@C_{60} state.

The depolarisation rate λ of the low-frequency Mu@C_{60} oscillation was studied as a function of temperature. We assume Arrhenius type dynamics, as would govern spin-lattice (T2) relaxations in NMR:[139]

$$\lambda \sim \frac{1}{\tau} = A \exp\left(\frac{E_A}{k_B T}\right). \quad (3.15)$$

3.6 Low energy muon spin rotation (LE- μ SR)

It can be seen in the Arrhenius plot in Fig. 3.10, that two dramatically different dynamic regimes strongly govern the depolarisation of this Mu@C₆₀ precession. The phase transition, occurring at roughly 100 K, matches the glass phase transition temperature (T_g) for C₆₀. Below this temperature, the rotational degrees of freedom for the fullerene cages are completely frozen. Above T_g , a uniaxial ratcheting mechanism between different molecular orientations takes place until around 260 K, where the cages undergo continuous rotational diffusion.[140] Fitting the data to Eqn. 3.15 yields an activation energy (E_A), suitable for the ratcheting motion of the molecules above T_g , of 40 ± 3 meV. Below T_g , the activation energy of 1.0 ± 0.1 meV is too small for an orientational transition along any molecular axis. Rather, it is likely associated with the motion of Mu⁺ particle about the centre of the cage. Above T_g the activation is also very close to Meyer-Neldel energy for C₆₀, $E_{MN} = 35$ meV. E_{MN} is an activation energy term associated with the level of disorder in a material where hopping transport is the dominant carrier transport mechanism and is linked to the properties of the DOS in which charge transport occurs.[141–143]. The combination of increased rotational motion and Mu diffusion act to reduce the depolarisation rate of the Mu@C₆₀ state as the temperature increases. This is similar to the motional line-narrowing experienced in NMR experiments, where the increased motion of a sampling environment causes areas of varying magnetic field to become more homogeneous, reducing the depolarisation of the nuclear spin.

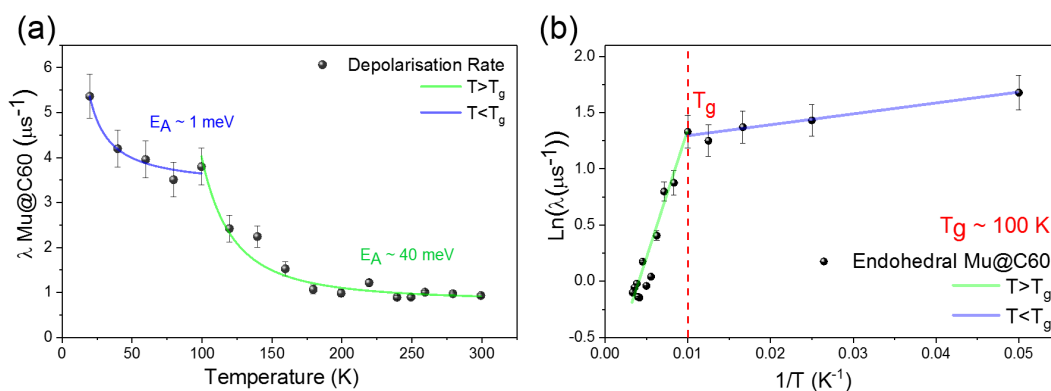


Figure 3.10: The temperature dependence of the Mu@C₆₀ zero field depolarisation rate is shown in (a). Two distinct exponential curves can be seen. An Arrhenius plot in (b) shows two linear regimes where the phase transition observed at around 100 K corresponds to the glass transition temperature for the molecular rotational degrees of freedom.

3.6 Low energy muon spin rotation (LE- μ SR)

We are, therefore, confident that we may attribute the low frequency (~ 0.5 MHz) zero field muonium signal to the endohedral Mu@C_{60} state. It is clear from this investigation that we can use the endohedral Mu@C_{60} state to study in depth the dynamics of the fullerene molecules. Due to the Zeeman splitting of the triplet hyperfine levels, we may also use the Mu@C_{60} state as a highly sensitive magnetic probe. This study will show how emergent magnetic effects at molecular interfaces can be studied via small changes muonium oscillation frequencies.

CHAPTER 4

Reversible spin storage in
 C_{60} /metal-oxide heterojunctions

4.1 Introduction

As far back as 2011, it was realised that molecular spintronics could not compete with device architectures borrowed from inorganic spintronics by simply replacing inorganic spacer layers with organic ones. Despite the low spin-orbit coupling of organic, carbon-based, materials and accompanying high spin lifetimes, mobilities of carriers in these materials are generally very poor, leading to relatively uncompetitive spin diffusion lengths.[144] Moreover, the lack of reproducibility and degradation of molecular devices are significant obstacles to industrial adoption. In spite of these drawbacks, organic spintronics research remains worthwhile due to the potential for reduced device processing costs combined with more sustainable and perhaps recyclable constituent materials. Additionally, novel device functionalities that can be synthetically engineered or utilise effects that are unique to molecules make research into molecular spintronics advantageous.

In particular, zero-dimensional systems, such as single-molecule magnets, exhibit potential for quantum information processing. The magnetic hysteresis observed in these systems demonstrates their capability for information storage on the atomic scale.[145] In two dimensional systems, the spin-dependent interface states that emerge between molecular and metal surfaces can lead to a variety of surprising macroscopic effects.[21; 49; 63; 146; 147] There has been a concerted effort to comprehend the complex spin-dependent charge interactions between molecules and metals, in particular, the formation of spin-polarised hybrid interfaces and tuneable surface states, where molecular materials offer unique behaviour and effects that can be exploited to produce multifunctional devices.[20; 22; 148]

In this chapter, we study the use of a hybrid molecule/metal-oxide semiconducting device to store spin-polarised charge in localised, interfacial states. The accumulation and extraction of charge are controlled by the spin-dependent density of states of the interface. The device is, in essence, a spin analogue of a conventional circuit element, the spin capacitor. This effect was first observed by performing X-ray absorption spectroscopy (XAS) measurements on C_{60} tunnel junctions while simultaneously

applying electrical bias.

The measured XAS junctions comprised a thick (30 nm) cobalt electrode separated from a 15 nm C₆₀ film by a 1.4 nm Al₂O₃ tunnel barrier, which acted to prevent the formation of a magnetic interface state. Mn was sputtered directly onto the C₆₀ film, with a thickness of 3 nm, and capped with a 1.6 nm Al layer. Oxygen permeates the Al cap producing an insulating capping layer and a thin manganese oxide film on the surface of the C₆₀. It is necessary to minimise the thickness of over-layers on the C₆₀ to reduce signal loss through the scattering of Auger electrons.

The electronic structure of C₆₀ in such a device is shown in Fig. 4.1. The carbon K-edge was probed before, during and after the application of a bias to characterise any changes in the NEXAFS spectra due to charge accumulation. In the initial state, before a bias, the K-edge shows the expected peak of the C₆₀ LUMO at 284 eV but also a hybridisation shoulder at 282.5 eV (labelled ‘Ground’). Such features in the electronic structure for molecular systems are attributable to hybrid interface states.[62; 63] The electronic structure of the C₆₀ is mostly unchanged during charge transport, only the signal to noise ratio is affected due to crosstalk of the TEY drainage with the sample electronics (labelled ‘0.2 V’). However, once the external bias is removed and the device is left floating, the LUMO at 284 eV is quenched and a new peak dominates the NEXAFS at 283 eV, which we refer to as LUMO* (labelled ‘Charged’). The change in the edge structure was observed to be extremely stable over many hours, possibly due to additional charging effects via the X-ray irradiation. X-ray magnetic circular dichroism measurements (XMCD) reveal a polarisation dependence in the LUMO* state at room temperature. The emergent spin-split edge feature can be removed through discharging the sample to a common ground, demonstrating a reversible accumulation of spin-polarised charge (labelled ‘Discharged’).

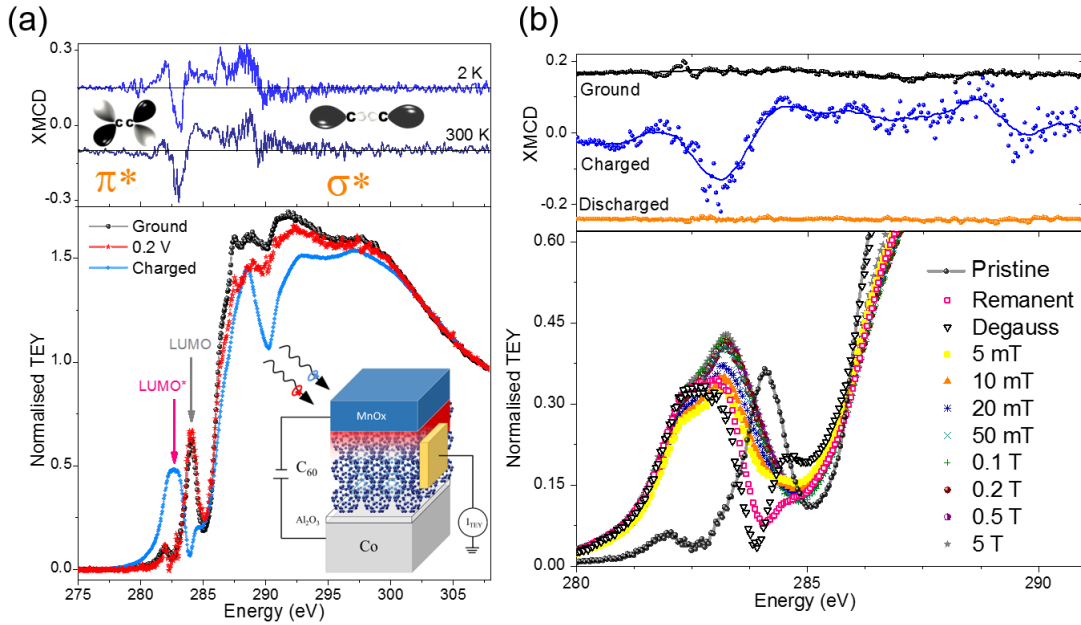


Figure 4.1: The observation of spin-polarised charge trapping. (a) Bottom: XAS measurements of the carbon K-edge for a junction where the structure is $\text{SiO}_2//\text{Co}(30)/\text{Al}_2\text{O}_3(1.6)/\text{C}_{60}(15)/\text{MnO}_x(2.5)$ - film thicknesses in brackets are in nm. Following the application of a 0.2 V bias to the sample the LUMO broadens and shifts to 283 eV. This persists until the electrodes are connected to a common ground. Top: XMCD measurements show an emergent spin polarisation in the π^* states (<290 eV) at room and low temperature for the charged state. (b) Top: The XMCD for the initial, charged (post-bias), and discharged (grounded) state measured at room temperature. Bottom: Dependence of the carbon K-edge in remanence following the application of out of plane fields. The position of the emergent LUMO* peak tends towards the pristine LUMO energy as the out of plane field is increased. In both figures, the spectra have been normalised following a background subtraction. Adapted from [149] where the original data features in the thesis of T. Moorsom [150] and was measured by TM and the author, MR.

The energy dependence of the LUMO* orbital with magnetic field was studied by applying out of plane magnetic fields and then measuring at remanence. The most significant energy shift in the position of the emergent LUMO* is observed when the Co electrode is saturated in-plane. Applying increasingly higher out of plane fields before measuring at remanence leads to domain formation and demagnetisation of the cobalt electrode. This causes the LUMO* peak to shift towards the pris-

4.2 Transport characterisation of metal-oxide /molecule devices

tine LUMO. This experiment demonstrates the strong coupling on the accumulation of spin-polarised charge in the molecule with the magnetisation of the cobalt electrode.

The interpretation of these measurements is in good agreement with density functional theory (DFT) calculations (further discussed in section 4.5). Simulations show spin-splitting of the interfacial states which lead to a spin-dependent accumulation of charge in the molecular layers. It is the purpose of this study to further elucidate upon the nature of this effect through spectroscopic techniques such as XAS/XMLD and LE- μ SR. By understanding the criticality of these effects on the choice of constituent materials in these heterostructures, we can rationalise this remarkable observation, connecting it to a coherent theory.

In this chapter, the work attributed solely to the author was all RT transport and PL spectroscopy measurements. All sample design, fabrication and data analysis related to the LE- μ SR measurements was also performed solely by the author. LE- μ SR measurements were performed on the LEM beamline at PSI, with the assistance of; O. Céspedes, S. Lee, R. Stewart, M. Flokstra and local contact T. Prokscha. XAS, XMCD and XLD measurements were performed on the BOREAS beamline at the Alba synchrotron, with the assistance of; T. Moorsom, F. Al Ma'Mari, O. Céspedes and the local contacts P. Gargiani and M. Valvidares. The author and T. Moorsom performed the sample fabrication and data analysis related to these measurements.

4.2 Transport characterisation of metal-oxide /molecule devices

For the duration of this study we consider hybrid molecule/metal-oxide heterojunctions with two typical device architectures. These are:

- [Co(10-30 nm)/ Al₂O₃(1.6 nm)/ C₆₀(20-100 nm)/ MnO_x(2.5-5 nm)/Al(1.2 nm)]
- [MnO_x(10 nm)/ C₆₀(20-100 nm)/ Co(10-30 nm)/ Al(1.2 nm)]

The metal-oxide used in this chapter is grown by plasma oxidation of sputtered Mn (see section 3.1). Using this method we form a non-stoichiometric phase of

4.2 Transport characterisation of metal-oxide /molecule devices

manganese oxide. This is informed by Raman spectroscopy characterisation where there is some indication of the presence of both Mn_2O_3 and MnO_2 . Consequently, the metal-oxide layer is referred to as MnO_x . XRR critical edge measurements performed by N. Alosaimi conclude that $x = 1.5 - 2$. This is confirmed by TEM-EDX measurements performed by the author and discussed in section 4.6. The inclusion of MnO_x into electrically charged devices will undoubtedly lead to the migration of oxygen atoms throughout the film during voltage application.[151] Both Mn_2O_3 and MnO_2 are expected to manifest semiconductor properties. MnO_2 is an n-type semiconductor whereas Mn_2O_3 is a p-type semiconductor.[152]

In some samples, the Co is replaced with Cu. This allows us to compare the effect of the magnetic electrode on the polarisation of accumulated charge. Using a tunnel barrier determines whether there is spin conserved injection from the ferromagnetic electrode in the C_{60} LUMO, as understood from the conductivity mismatch problem.[153] More critically, the use of an insulating barrier quenches any charge transfer from the metallic electrode, which dramatically affects the doping of the C_{60} film.[154] The typical room temperature DC-IV curves for these devices, shown in Fig. 4.2, demonstrate the different electronic properties between the two device structures. For both architectures, there is direct contact between the metal-oxide (MnO_x) and molecular layer (C_{60}). At this interface, C_{60} -O bonding gives rise to an interfacial dipole layer, which generates a strongly rectifying barrier. The potential well which forms here also limits charge transport due to the efficient trapping of charge. Similar observations have been made for organic devices that utilise interfacial polar layers such as LiF to modulate the energy level alignment at the interface.[155; 156]

The room temperature DC-IV curves for the two typical device structures are shown in Fig. 4.2. For the device structure which excludes the insulating barrier, there is greater n-doping of the C_{60} from the cobalt film.[154; 157] This leads to a rectifying diode device with a highly asymmetric dark IV curve. When this sample is illuminated, a photo-current is generated without the application of bias. In C_{60} the exciton binding energy is 0.5 eV.[158] The observed photovoltaic effect requires that the inbuilt potential formed between the MnO_x and C_{60} is large enough to dissociate

4.2 Transport characterisation of metal-oxide /molecule devices

the generated electron-hole pair. When the insulating barrier is in place, charge transfer from the Co layer is quenched, and the efficiency of the photovoltaic is negligible. For the dark IV in this configuration, a characteristic curve for trap-limited transport in heterojunctions is observed under the positive bias.[155] Under illumination, the IV under positive bias completely changes shape, and an enhancement in the conductivity of the C_{60} is observed due to the photo-generation of carriers into the molecular LUMO.

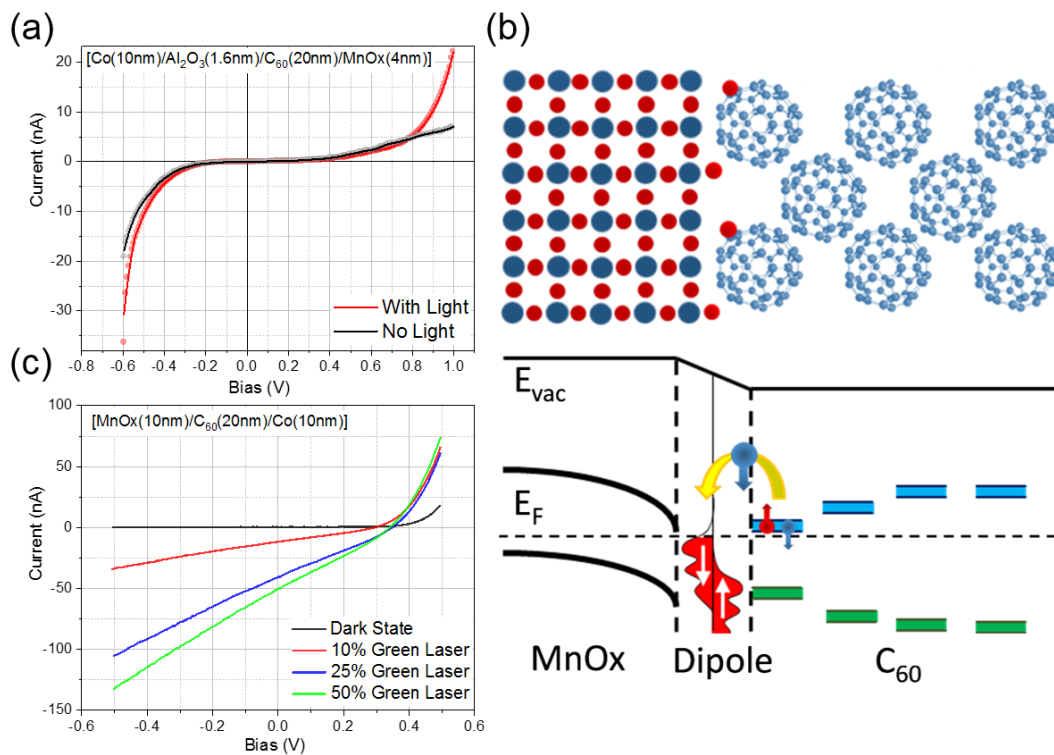


Figure 4.2: Transport characteristics for devices used in this study. (a) DC-IV for a junction with an alumina barrier. The structure here is the same as that used for XAS in Fig. 4.1. The barrier quenches the photovoltaic effect. A considerable change in the conductivity is observed with light exposure due to photoexcitation of carriers into the LUMO. (b) A schematic of the band structure at the MnO_x/C_{60} interface. The MnO_x/C_{60} interface forms a rectifying junction where the interfacial potential leads to significant band bending. The C_{60} -O dipole layer generates a potential well which leads to trap-limited charge transport. (c) When the device has no alumina barrier the increased doping from the cobalt electrode leads to a highly asymmetric IV and an increased efficiency of the photovoltaic.

4.2 Transport characterisation of metal-oxide /molecule devices

Under low bias, the electronic transport through devices grown as described in section 3.1 is non-uniform. The current pathways through these devices were characterised by measuring the photoluminescence (PL) at the active device location while simultaneously applying a bias. PL is a direct probe of the quantum efficiency for exciton recombination in an organic semiconductor. It is, therefore, sensitive to many external stimuli such as temperature, magnetic and electric fields and trapping of exciton states.[159; 160] Of particular use is the effect of negative luminescence. In the presence of some electrical bias, the electron-hole pair will decouple from each other, separating due to the applied electric field. This reduces the chance of recombination and hence the quantum yield of the system. Thus, a reduction in the luminescence of the molecule is observed.[161]

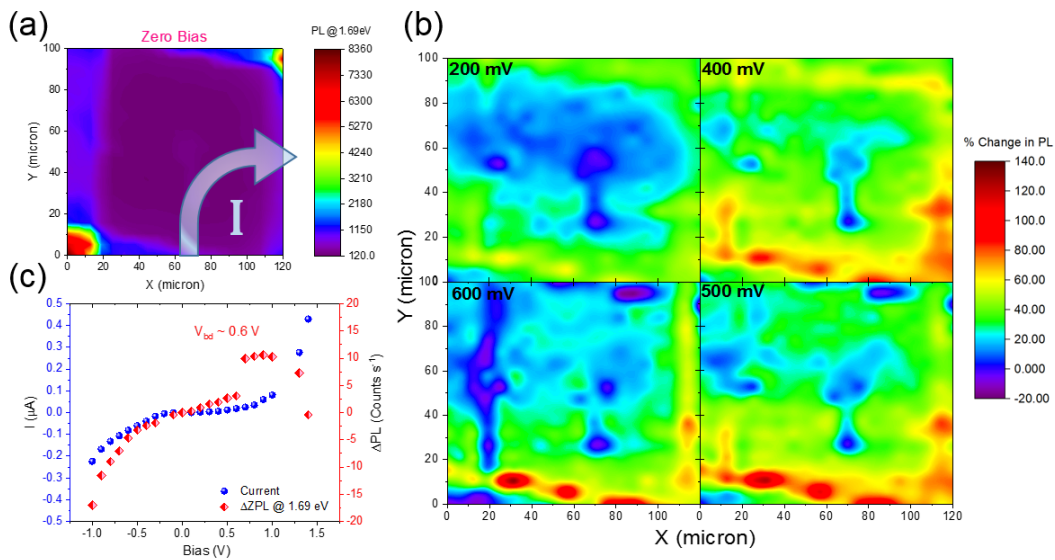


Figure 4.3: Dependence of the photoluminescence (PL) upon sample bias. (a) The zero-phonon PL emission is measured in zero bias over a device where the structure is $\text{SiO}_2//\text{Co}(30)/\text{Al}_2\text{O}_3(1.6)/\text{C}_{60}(15)/\text{MnO}_x(2.5)$ - film thicknesses in brackets are in nm. The active junction area ($100 \times 100 \mu\text{m}^2$) is the purple area of lowest luminescence. This is due to the quenching of the PL through charge transfer. (b) The spatial maps of the PL over the junction as the device is in operation shows areas of current crowding within the device, as areas where the luminescence increases/decreases more than the surrounding area. (c) The bias dependence of the PL is plotted with the DC-IV data from the same device. Here, a sudden increase in PL is seen as a positive 0.6 V is applied to the junction.

PL measurements were taken on a C₆₀ tunnel junction with the structure; [Co(10 nm)/ Al₂O₃(1.4 nm)/ C₆₀(20 nm)/ MnO_x(3 nm)]. Electrical bias was applied to the sample *in situ*. The bias was applied such that in the positive direction, electrons are moving from the cobalt into the molecular layer. Fullerene C₆₀ emits light at 1.69 eV due to the recombination of the Frenkel exciton with phonon-assisted recombination occurring at 1.65, 1.6 and 1.5 eV.[162] The spatial dependence of the luminescence at the zero-phonon line (ZPL@1.69 eV) is shown in Fig. 4.3(a). The device area can be distinguished as the area where the PL is reduced due to electron transfer.[163]

As demonstrated in Figs. 4.3(b, c) hot electron injection over the tunnel barrier creates secondary excitations which boost the luminescence signal. In Fig. 4.3(c) this is observed as a step feature in the ZPL line at around 0.6 V as carriers possess enough energy to tunnel directly into the LUMO of the C₆₀. This predominantly takes place at the corners of the device where the current density is largest.[164–166]

4.3 XAS of C₆₀ junctions

To confirm the generation of interfacial charged states in MnO_x/C₆₀ interfaces, the electronic band structure for devices whose structure deviate from that shown in Fig. 4.1 were obtained. XAS measurements were performed of the carbon K-edge with an electrical bias for samples that first exclude the manganese oxide layer and secondly have a non-magnetic electrode layer. We are then able to determine the role of these two factors in the generation of spin-polarised trapped charge in the molecular C₆₀ layer. X-ray absorption spectroscopy measurements were therefore undertaken on the following structures:

- [Co(30 nm)/Al₂O₃(1.4 nm)/C₆₀(15 nm)/CuO_x(2.5 nm)/Al(2 nm)]
- [Cu(30nm)/Al₂O₃(1.4 nm)/C₆₀(15 nm)/MnO_x(2.5 nm)/Al(2 nm)]

All junctions were prepared with active areas of 100×100 μm² and deposited onto glass. When fabricating these devices on thermally oxidised Si, current shunting becomes unavoidable due to the comparable resistance of the C₆₀ barrier relative to

the substrate.

Fig. 4.4 demonstrates the changes in the NEXAFS for devices comprising a magnetic electrode and a CuO_x/C_{60} interface. These devices are expected to have similar transport properties to those seen in Fig. 4.2(a) as there will also be an O- C_{60} dipole layer forming, limiting the charge transport across the interface in this system. Yet, when these devices undergo electrical charging with a small bias (50-200 mV), comparable to that used in the experiment shown in Fig. 4.1, only minor changes in the NEXAFS are observed. Unlike the original experiment, after the application of a bias, there are no observable changes in the position of the LUMO. In this first control structure, there is also no measurable XMCD, which was observed for the original device featuring the MnO_x/C_{60} interface. This experiment alludes to the importance of the band structure of the MnO_x in the formation of the emergent spin-polarised states seen in Fig. 4.1.

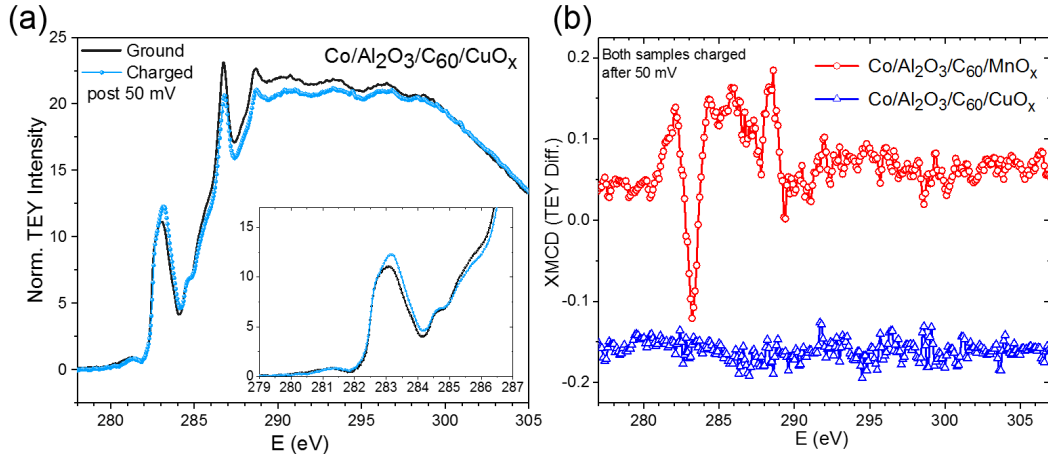


Figure 4.4: Spectroscopy measurements of a control device without MnO_x . (a) The XAS for a device of structure $SiO_2// Co(30)/ Al_2O_3(1.6)/C_{60}(15)/CuO_x(2.5)$ - film thicknesses in brackets are in nm. The spectra have been normalised following a background subtraction. In the absence of the MnO_x , only minor changes in the NEXAFS carbon K-edge is observed before and after bias. (b) the XMCD for a device of this type clearly shows no effect when compared to that which includes the MnO_x/C_{60} interface.

Fig. 4.5 demonstrates the effect of electrical charging on a sample which excludes the ferromagnetic bottom electrode but still includes the MnO_x/C₆₀ interface. Fig. 4.5(a) displays the observed changes in the NEXAFS for this second control structure. It can be seen that after the application of 200 mV to the sample, a shoulder emerges at roughly 1 eV below the LUMO-derived band. The feature is typically seen for partially filled, hybridised interfacial LUMO states.[62] The onset of this molecular orbital is once again reversible as the original carbon edge can be recovered upon grounding of the sample. However, no measurable XMCD was observed in either the charged or discharged state for this system. The orientation of the emergent orbital was analysed by measuring the linear polarisation dependence of the carbon K-edge. In Fig. 4.5(b) the absorption edges obtained at a grazing incidence (45°) for vertically and horizontally polarised x-ray light is shown. A complex XLD signal can be observed over the entire edge. There is a significant dependence of polarisation for the absorption into the emergent hybrid shoulder at around 282 eV which is not present when the sample is in the discharged state, as seen in Fig. 4.5(c). Great care must be taken in the measurement of linear polarisation dependent absorption at the carbon edge as a common artefact in the normalisation of these signals will arise due to the contribution of carbon contaminants on beam line mirrors and normalisation grids which show large XLD effects.[167] The fact that the XLD only emerges following the charging of the device demonstrates that the XLD observed at the emergent hybrid edge state is no artefact of the measurement procedure.

Linearly polarised X-rays can determine the axial orientation of orbitals by directly probing the quadrupole moment of a local charge distribution around an absorbing atom. For highly anisotropic charge distributions such as orbitals with σ or π symmetry, a maximum in the absorption into these valence states will be achieved when the electric field vector of the incoming light \mathbf{E} is parallel to the direction of maximum charge density.[168] This forms the basis for the characterisation of molecular orientations on surfaces through a ‘searchlight effect’.

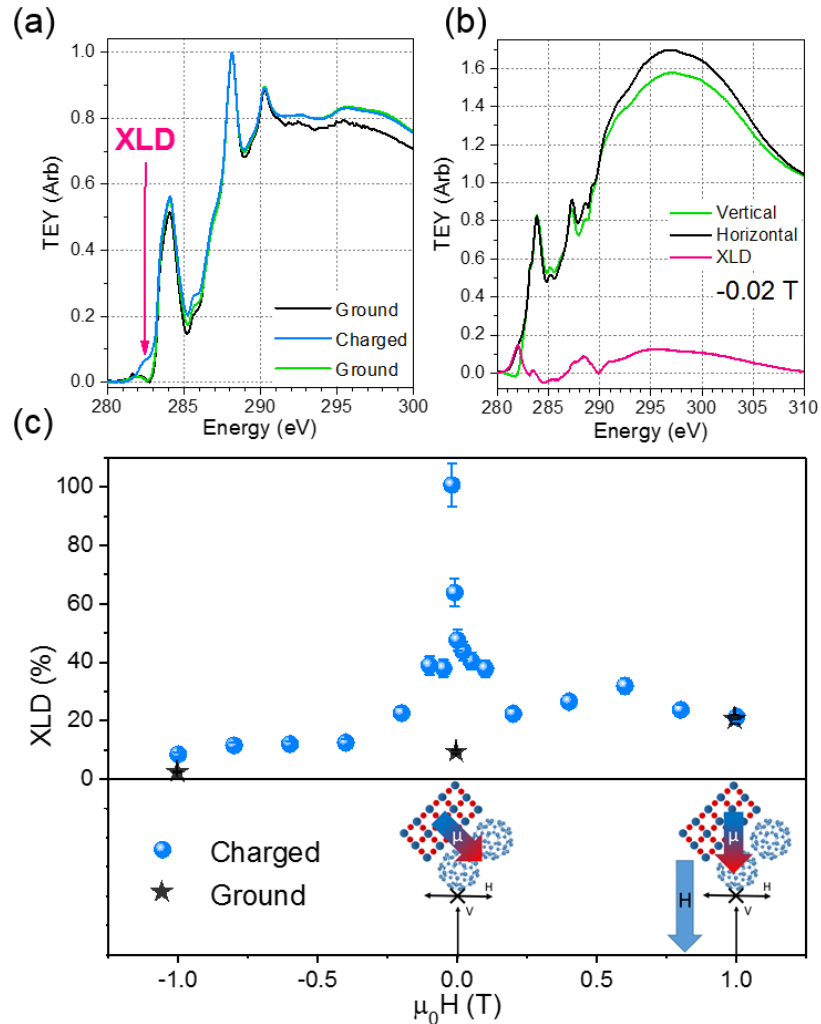


Figure 4.5: X-ray absorption spectroscopy measurements of a control device in the absence of the ferromagnetic Co electrode. All spectra have been normalised following a background subtraction. (a) The NEXAFS measurements show the emergence of a hybrid edge roughly 1 eV below the LUMO band after a 200 mV bias has been applied to a device with structure $SiO_2// Cu(30)/ Al_2O_3(1.6)/ C_{60}(15)/ MnO_x(2.5)$ - film thicknesses in brackets are in nm. (b) XLD measurements taken at a grazing angle (45°) show dichroism in this emergent edge. (c) XLD measured as a function of field, demonstrates the ability to re-orientate the emergent moment with an applied magnetic field.

The size of the linear dichroism at the hybrid peak was studied with magnetic field. The application of a large field applied parallel to the X-ray \mathbf{k} vector, eliminates the dichroism as shown in Fig. 4.5(c). Such a strong magnetic field dependence in this

system is very surprising. As previously stated, in the absence of spin order, linear dichroism in the absorption edge indicates a large charge anisotropy and is dependent upon the symmetry of valence orbitals. However, in magnetic systems, there may also exist some XLD effect due to the alignment of the polarisation vector with the spin axis.[169] The X-ray magnetic linear dichroism effect is particularly useful in the characterisation of anti-ferromagnetic systems. Here, there is no net magnetic moment but merely a preferential magnetic axis. Spatially symmetric charge distributions will undergo some deformation due to the ordering of local atomic spins via the spin-orbit interaction.[170] This is why XMLD is particularly useful for imaging domain structures in anti-ferromagnets but also in characterising the magneto-crystalline anisotropy of metallic systems. For 3d metals, only a small XMLD effect ($\sim 10\%$ maximum) can be expected due to the relatively small size of the spin-orbit coupling, and resultant small charge anisotropy. The system we measure here will have an even smaller SOC strength, and so an XLD signal of 100% is surely unlikely to arise from SOC induced distortions of the valence orbital. Instead, what we observe is the complete reorientation of the dipole formed at the interface between MnO_x/C₆₀. The peak in the XLD is observed in zero field. This implies an out of plane anisotropy of these orbitals in the charged state, as would be expected for a $\pi-d_z$ hybrid orbital.[171]

The XAS observations of these devices are indeed complex as various phenomena can contribute towards dichroism effects, particularly in covalently bonded systems such as C₆₀. By performing these studies on control structures, it has been made clear of the significance of the MnO_x/C₆₀ interface in the manipulation of the C₆₀ orbital structure after charging the interface with a small electrical bias. XMCD measurements in the original device showed polarisation dependence in the emergent sub-LUMO edge state. K-edge dichroism involves s to p dipole transitions. Consequently, it mainly probes the orbital polarisation in the final state. This is however intimately linked to the spin polarisation of the orbital moment in the final state through spin-orbit coupling.[172] The measurements of XLD of the charged MnO_x/C₆₀ interface demonstrate the intrinsic dependence of the hybrid orbital moment with the applied magnetic field.

4.4 LE- μ SR studies of spin trapping at MnO_x/C₆₀ interface

To investigate the presence of any emergent magnetic effects in a MnO_x/C₆₀ heterojunction, low energy muon spin rotation (LE- μ SR) was used to provide a magnetic profile of active devices while the samples were electrically charged and optically irradiated *in situ*. A beam of almost fully polarised positive muons (μ^+) is moderated to the keV energy range so that their stopping distribution can be tuned approximately over a range of 10-100 nm.[129; 173] As these experiments are taking place on devices with electrical contacts, the implantation of the muon beam was solely tuned by the potential difference across the moderator. High voltages were therefore not applied to the sample plate, avoiding any potential for crosstalk between the sample and transport electronics. The time evolution of the muon spin polarisation is a highly sensitive probe of local magnetisation (see Section 3.6 for further detail). LE- μ SR has been successfully used in the characterisation of spin-dependent charge transport in organic spin valves and molecular magnetic effects.[21; 45; 65] As demonstrated in Section 3.6, the bound muonium state is particularly sensitive to the electronic properties of C₆₀ and local magnetic fields.

4.4.1 LE- μ SR with electrical charging

In this study, we probe a large area junction with the structure: [Glass(Substrate)// Co(20 nm)/ Al₂O₃(2 nm)/ C₆₀(50 nm)/ MnO_x(3 nm)/ C₆₀(50 nm)/ Au(25 nm)]. The bottom (top) C₆₀ layer probes for the emergence of magnetic states close to (decoupled from) the cobalt substrate.

4.4 LE- μ SR studies of spin trapping at $\text{MnO}_x/\text{C}_{60}$ interface

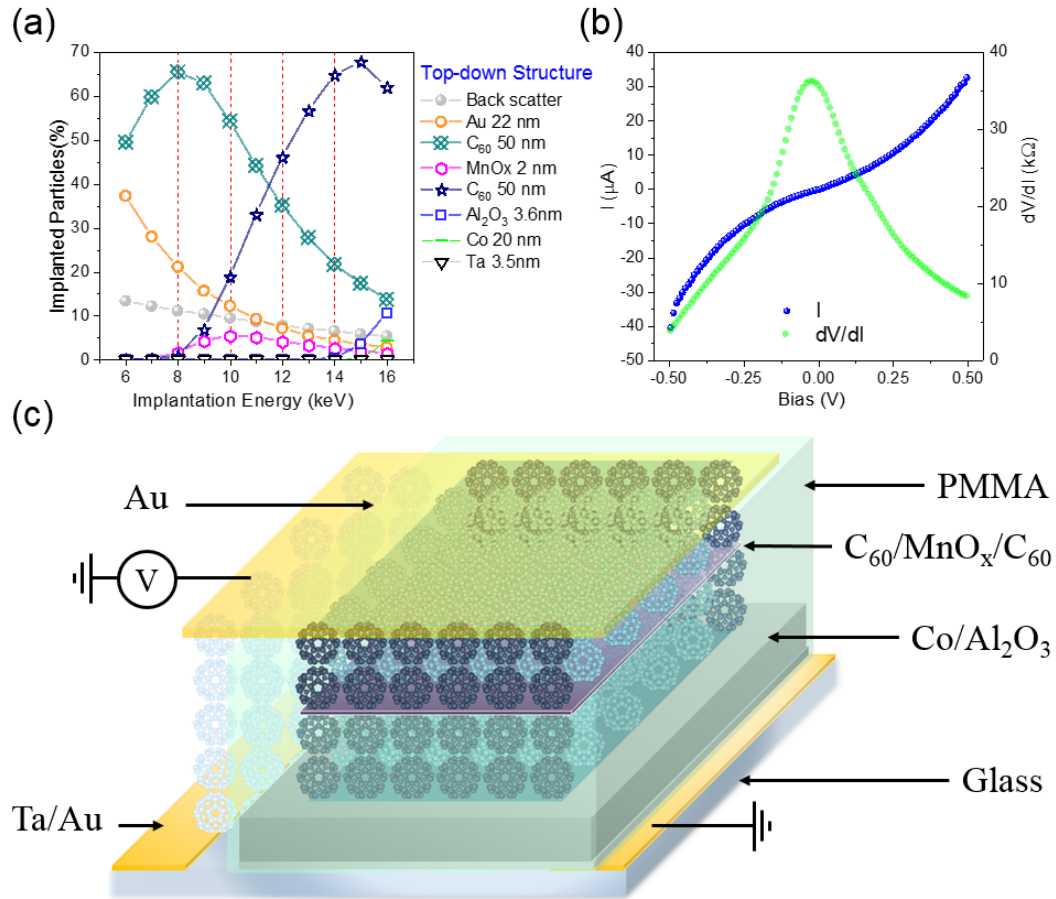


Figure 4.6: Wide-area molecular junctions for muon spin rotation measurements with electrical charging. (a) Energy dependence of the proportion of muons stopping within each layer of the fabricated wide-area molecular junction. (b) Room temperature charge transport characteristics of the wide-area junction show a non-linear dependence of the resistance with voltage as would be expected for tunnelling across the Al_2O_3 barrier. (c) A schematic of the finished device is shown.

On the LEM beamline at PSI, there is a broad muon beam (~ 20 mm in diameter) and low flux ($\sim 4500 \mu^+/\text{s}$). Consequently, to allow for reasonable measurement times, the LE- μ SR technique requires large area samples. Therefore, wide-area molecular junctions, with roughly 200 mm^2 active areas, were fabricated. Firstly, Ta/Au contacts were deposited onto Corning Eagle XG glass substrates. The ferromagnetic electrode and tunnel barrier, $\text{Co}(20 \text{ nm})/\text{Al}_2\text{O}_3(2 \text{ nm})$, was then deposited through a shadow mask. Here, the Al_2O_3 not only acts to protect the ferromagnet against oxidation

4.4 LE- μ SR studies of spin trapping at $\text{MnO}_x/\text{C}_{60}$ interface

between fabrication steps, but it will also become part of the tunnel barrier, ensuring spin conserved tunnelling of charges from the Co into the molecular layer. In vertical junctions, inhomogeneous current distributions can occur when the barrier resistance is comparable to that of the electrode resistance within the same area. Therefore, the use of a thick (~ 100 nm) C_{60} barrier ($R \sim 10^3 \Omega$) combined with thick (~ 20 nm) metal electrodes ($R \sim 1 \Omega$) leads to greater uniformity of the current flow through the device.[174] In addition, variations in the electric field around the edge of the cobalt electrode can lead to short circuits and current crowding. To avoid this, the active junction area was defined with an optical lithography step. A 200 nm layer of PMMA A4950K was spun over the whole device. A 200 μm^2 window was then exposed to UV and ozone. This was finally developed in acetone and exposed to an Ar plasma to etch any residual PMMA and to leave a clean Al_2O_3 surface. The remainder of the device was then deposited using the methods outlined in Section 3.1 to yield wide-area molecular junctions. A schematic of such a device is shown in Fig. 4.6 with the corresponding fraction of the muons stopping throughout the device. After using these processing methods, the DC I-V data shows a non-linear dependence of the resistance with voltage. This is to be expected for transport dominated by tunnelling. The resistance of the devices also increases at lower temperatures, suggesting that charge carriers indeed tunnel into the C_{60} LUMO, undergoing the expected variable-range hopping transport.

Measurements were carried out at 250 K, in zero field (ZF) and a 150 G applied transverse field (TF). In the TF configuration, we are only sensitive to the time evolution of the diamagnetic μ^+ particle whose polarisation is initially perpendicular to the applied field. From the experiments carried out in Section 3.6.2, we have established that the muon particles that thermalise within the molecular layer are expected to form a muonium bound state. The oscillation signal for muonium corresponds to transitions between μ^+e^- spin configurations, the frequency of which is governed by hyperfine coupling. In a field of 150 G, the timescale of these transitions (> 100 MHz) cannot be resolved by the timing instrumentation and so averages to zero. Therefore, in TF there is no contribution to the measured signal from bound muonium, only the μ^+ particle. In the ZF configuration, there will be no precession of the μ^+ particle. Consequently, any observed oscillation signal is attributable only to the

4.4 LE- μ SR studies of spin trapping at MnO_x/C₆₀ interface

two C₆₀ muonium bound states. These are either the endohedral Mu@C₆₀ state or the exohedral MuC₆₀ radical state. The ZF measurements were carried out at 250 K. At this temperature, the time-scale for the molecular rotation ($\sim ps$) is occurring much faster than the muon decay time ($\sim \mu s$). Therefore, at this temperature we do not observe the radical MuC₆₀ state.[134] We are, however, able to observe the low frequency 0.1-0.4 MHz ZF oscillation, which has been previously assigned to an axially asymmetric endohedral Mu@C₆₀ state for charged C₆₀. [21; 65] The state behaves similarly to the endohedral sub-MHz oscillation observable in C₇₀, where the precession frequency is highly sensitive to changes in magnetic texture owing to the Zeeman splitting of the hyperfine coupling.[175; 176] It has been previously reported that the emergence of weak magnetic states in C₆₀ based interfaces give rise to a coexistence of signals owing to the endohedral muonium state with a second low-frequency precession, attributed to magnetic interfacial C₆₀. [21; 65]

In this system, the broad internal field distribution generated by the stray field of the magnetic cobalt electrode imparts a large depolarisation upon the muonium states. As shown in Fig. 4.7(b), when higher implantation energies are used the measured Mu@C₆₀ depolarisation rate increases monotonically owing to the increasing distribution of stray field originating from the cobalt electrode. Due to these high depolarisation rates of the Mu@C₆₀ state, we elected to apply two separate fitting procedures to the data. In the first model, we have simplified the system, restricting the fitting theory to simulate a single highly damped Mu@C₆₀ oscillation. A non-oscillating depolarising function is incorporated to represent slowly relaxing mechanisms, such as the interaction of the μ^+ with nuclear moments within the sampling environment. For this single frequency model, the resulting ZF- μ SR data are fitted with *musrfit* (see Section 3.6) to the following function[130]

$$A_S(t) = A \cos(\varphi + 2\pi\nu_{Mu@C_{60}}t) \exp(-\lambda_{Mu@C_{60}} \cdot t) + A_{tail} \exp(-\lambda_{tail} \cdot t) \quad (4.1)$$

Here, $\nu_{Mu@C_{60}}$ corresponds to the frequency associated with hyperfine transitions of the axially anisotropic endohedral Mu@C₆₀ state. A is the decay asymmetry which parametrises the portion of the precession signal attributable to the corresponding muon state. The phase angle, φ , denotes the angle between the muon spin and the

4.4 LE- μ SR studies of spin trapping at $\text{MnO}_x/\text{C}_{60}$ interface

positron detector at $t = 0$. The decay constant, λ , is the depolarisation rate determined by the polarisation loss mechanisms. Numerous measurements taken for separate voltage states permits us to fix to the average Mu@C_{60} asymmetry A , phase angle φ and slow depolarisation rate λ_{tail} . This allows us to fit, with reduced uncertainty, only for the frequency of the muonium state and the corresponding depolarisation rate ($\nu_{\text{Mu@C}_{60}}$ and $\lambda_{\text{Mu@C}_{60}}$).

The results obtained using the single frequency model are shown in Fig. 4.7. Application of high voltages applied across the moderator yield the four implantation energies shown in the simulated stopping profiles Fig. 4.7(a). As the energy of implantation increases, there is an increase in the frequency of the Mu@C_{60} oscillation owing to the increasing strength of the stray field from the cobalt electrode. With the application of a 200 mV bias applied, such that electrons flow from the bottom Co electrode toward the top Au electrode, there is no discernible change in the depth dependence of the frequency obtained through the muonium precession fits. However, after the application of a voltage, when the sample is left in the charged state, a change in the trend is observed as a peak at 12 keV in the Mu@C_{60} frequency now appears. In the original NEXAFS study, presented in Fig. 4.1, the spin-polarised emergent state was only seen after the application of a bias. The changes in Mu@C_{60} frequency are only observed for the 10 - 12 keV implantation energy range. This coincides with the maximum number of particles stopping the $\text{MnO}_x/\text{C}_{60}$ interface.

4.4 LE- μ SR studies of spin trapping at $\text{MnO}_x/\text{C}_{60}$ interface

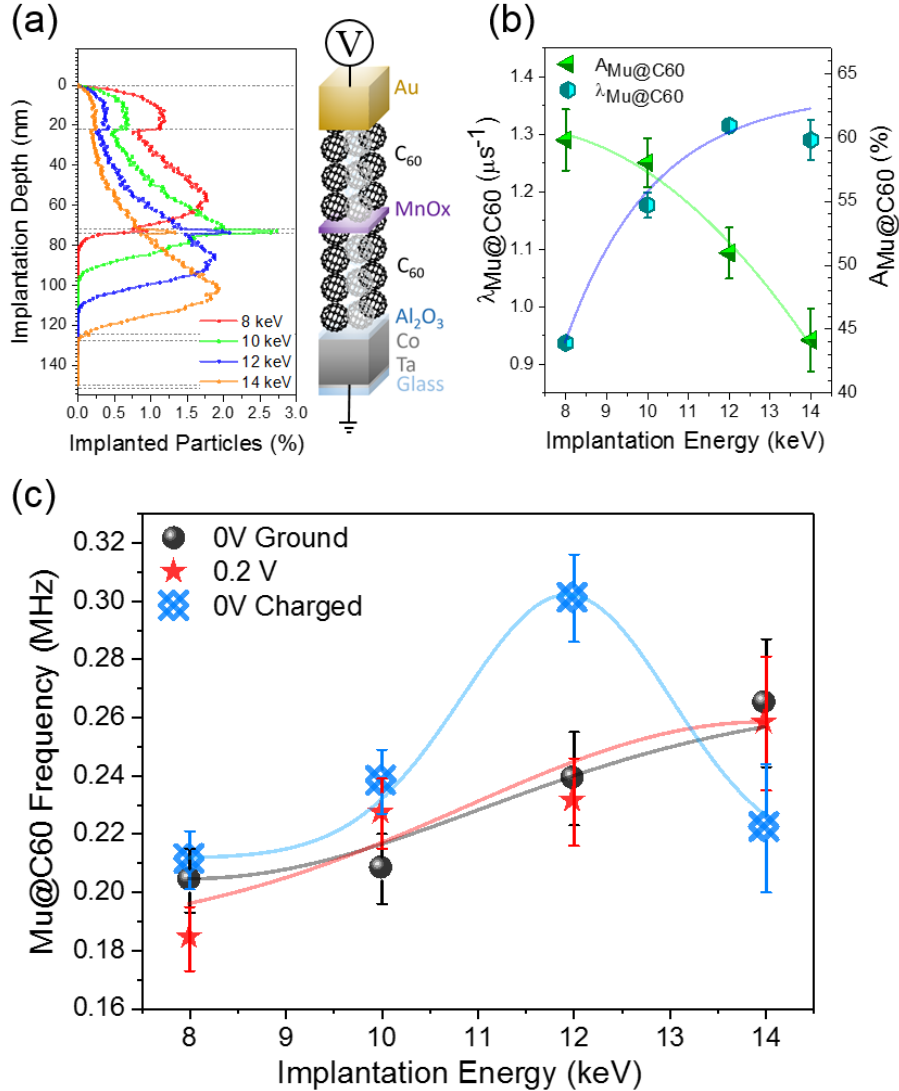


Figure 4.7: Local magnetic probing of the $\text{MnO}_x/\text{C}_{60}$ interface in zero field (ZF). (a) Calculated penetration profiles for the energies used in the LE- μ SR experiment. (b) The average Mu@C_{60} precession asymmetry $A_{\text{Mu@C}_{60}}$ and depolarisation rate $\lambda_{\text{Mu@C}_{60}}$ are shown as a function of implantation energy in ZF. (c) At 10 and 12 keV in ZF the frequency of the Mu@C_{60} state increases in the charged state after applying a voltage. Guides to the eye have been added in (b) and (c) for clarity.

The ZF Mu@C_{60} frequency is increased after the application of a bias by $26 \pm 9\%$ (0.06 ± 0.02 MHz) and $14 \pm 8\%$ (0.03 ± 0.02 MHz) for 12 and 10 keV, respectively. These small, but statistically significant, changes in muonium frequency could be

4.4 LE- μ SR studies of spin trapping at MnO_x/C₆₀ interface

interpreted in two ways. Firstly, as the device charges and accumulates some spin polarisation at the MnO_x/C₆₀ interface, the emergent magnetic state produces an increase in the local magnetic field. This gives rise to an increase in the Zeeman term of the hyperfine Hamiltonian which describes the C₆₀ muonium state. Secondly, as charge accumulates at the trap states localised at the MnO_x/C₆₀ interface, the charged molecular cages become distorted via Jahn-Teller distortion, leading to an increase in the anisotropy of the hyperfine tensor and a larger splitting of the triplet hyperfine levels in zero field.

As previously stated, we expect the emergence of a second muonium frequency for spin-polarised charged C₆₀. Therefore, a second model was produced to fit the ZF- μ SR data as

$$A_S(t) = A_{fast} \exp(-\lambda_{fast} \cdot t) + \sum_{i=1}^2 A_i \cos(\varphi + 2\pi\nu_i t) \exp(-\lambda_i \cdot t) \quad (4.2)$$

Here, A_i accounts for the typical anisotropic Mu@C₆₀ state with a frequency of 0.2-0.4 MHz, but it also accounts for a second oscillation that we attribute to spin polarised charged C₆₀ denoted as Mu@C₆₀^{*}. The fitting of this model is challenged by the large depolarisation and loss of asymmetry due to the stray field of the cobalt while also introducing larger uncertainty values due to the increase in free parameters. Rather than averaging over all the C₆₀ molecules for the penetration profile of the muons, the model can now fit separately those which are charged and may become spin-polarised. Despite the larger uncertainties produced in the fitting, the onset of some emergent frequency line is indeed detected at 10 and 12 keV implantation energies. The emergent signal is shown in Fig. 4.8. For the 10 and 12 keV implantation energies, systematic fitting shows that what is effectively an almost flat ($\nu < 0.05$ MHz, $\lambda = 0$) background function, with small asymmetry, picks up a 0.19 ± 0.01 and 0.28 ± 0.03 MHz oscillation frequency at 10 and 12 keV respectively. In the charged state of the sample, the emergent oscillation function remains constant at 8 and 14 keV (further away from the interface) despite undergoing the same analytical methodology. The emergent muonium oscillations at 10 and 12 keV possess respective depolarisation rates of

4.4 LE- μ SR studies of spin trapping at $\text{MnO}_x/\text{C}_{60}$ interface

0.6 ± 0.2 and $1 \pm 0.3 \mu\text{s}^{-1}$. The increase in the depolarisation rate in this instance represents a broadening in the distribution of sampled hyperfine coupling strengths at these implantation energies. This is likely caused by enhanced local magnetic field distribution, generated at the $\text{MnO}_x/\text{C}_{60}$ interface after the application of a voltage to the sample.

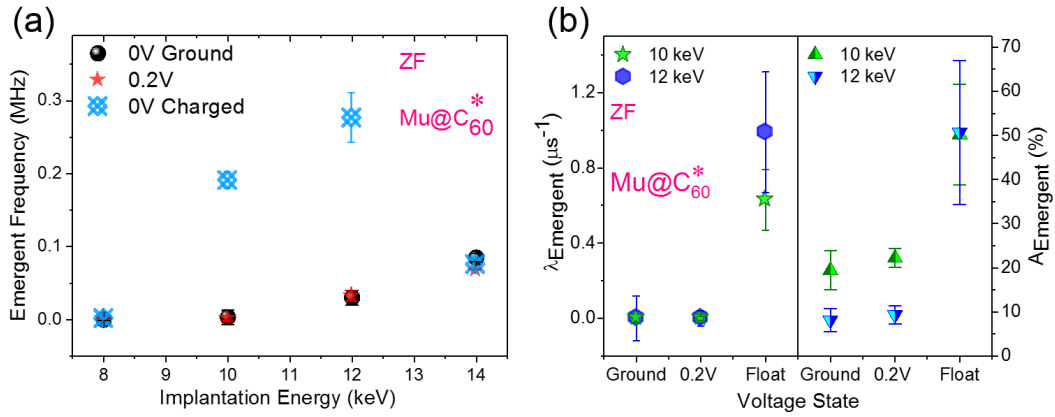


Figure 4.8: Emergent magnetic states probed by LEM with electrical charging. The ZF data has been fit using a two-frequency model. (a) The frequency of the emergent, charged (Mu@C_{60}^*) is seen to increase by over an order of magnitude at the MnO_x interface (10 and 12 keV) after the device has been left charged. (b) Increased Mu@C_{60}^* depolarization rate and oscillation amplitude in the charged state at 10 and 12 keV.

4.4.2 Transverse field measurements

ZF- μ SR measurements of a molecular junction with electrical charging have given clear evidence of changes to the C_{60} muonium precession close to the $\text{MnO}_x/\text{C}_{60}$ interface following the application of a bias across the sample. As previously stated, the frequency at which coupled μ^+e^- states will transition between different spin configurations is sensitive to not only the presence of local magnetic fields, but also changes to the anisotropic hyperfine tensor which governs the solutions for the Hamiltonian which describes the muonium hyperfine levels. Such changes can be brought about through distortions of the molecular cage, causing reductions in symmetry. It is expected that when fullerene C_{60} accepts additional electrons into the triply degenerate LUMO, a Jahn-Teller type distortion will lift this

4.4 LE- μ SR studies of spin trapping at $\text{MnO}_x/\text{C}_{60}$ interface

degeneracy.[121; 177] As is the case for anionic C_{60}^- and photoexcited states.[178; 179]

To assign these observations to the onset of some magnetic interfacial state, we must disentangle the observations of changes to the Mu@C_{60} precession from small changes in the molecular symmetry due to varying charge distributions over the portion of the sample probed by the muons. Therefore, μ^+ precession was measured in a transverse field (TF- μ SR) configuration. For TF- μ SR, a 150 G field is applied orthogonally to the initial muon polarisation. For such a field, transitions between hyperfine levels occur at time scales below that which can be detected with the sensitivity of the apparatus due to Zeeman splitting. Consequently, TF- μ SR is only sensitive to the precession of the diamagnetic unbound μ^+ particle and is particularly sensitive to variations in inhomogeneous field distributions owing to the faster muon precession about the applied field.

In transverse field, we model only the precession of the μ^+ in a static local magnetic field \bar{B}_{local} . The TF- μ SR data is therefore fitted with the function:

$$A_s(t) = A_{\mu^+} \cos(\gamma_{\mu} \cdot \bar{B}_{local} \cdot t + \varphi) \exp(-\lambda_{TF} \cdot t) \quad (4.3)$$

where $\gamma_{\mu} = 2\pi * 135.5 \text{ MHz T}^{-1}$ is the muon gyromagnetic ratio. Once again λ_{TF} accounts for depolarisation mechanisms of the μ^+ .

The results obtained through the fitting to the above TF model are shown in Fig. 4.9. It is once again made clear the effect of the stray field of the Co electrode on the μ^+ relaxation as the depolarisation rate increases as the average depth of the implanted muons increases. It can be seen in Fig. 4.9(a) that at 12 keV, we measure an increase in λ_{TF} of the TF- μ^+ particle from $0.43 \pm 0.03 \mu\text{s}^{-1}$ in the grounded state to $0.51 \pm 0.03 \mu\text{s}^{-1}$ in the charged state. Where the local field is small, or there is a broad distribution of local fields, such as in a spin glass, changes to the magnetic environment will be detected by the depolarisation of the μ^+ particle. Indeed, increases to the λ parameter of a similar magnitude have been attributed to the onset of some spontaneous magnetism in weakly ferromagnetic systems.[180; 181] Once more, the change brought about through the electrical charging of the device is greatest at the implantation energy localised to the bottom $\text{MnO}_x/\text{C}_{60}$ interface. To gain further understanding of the

4.4 LE- μ SR studies of spin trapping at $\text{MnO}_x/\text{C}_{60}$ interface

magnetic landscape of the sample, we can study the depth dependence of the extracted \overline{B}_{local} parameter. No statistically significant changes to the local field were observed here due to electrical charging of the interface. For this reason, the \overline{B}_{local} parameters have been averaged over the three charge states of the sample and shown in Fig. 4.9(b). The average local field is shown to peak at the bottom $\text{MnO}_x/\text{C}_{60}$ interface, which supports the existence of spin-split interface states there.

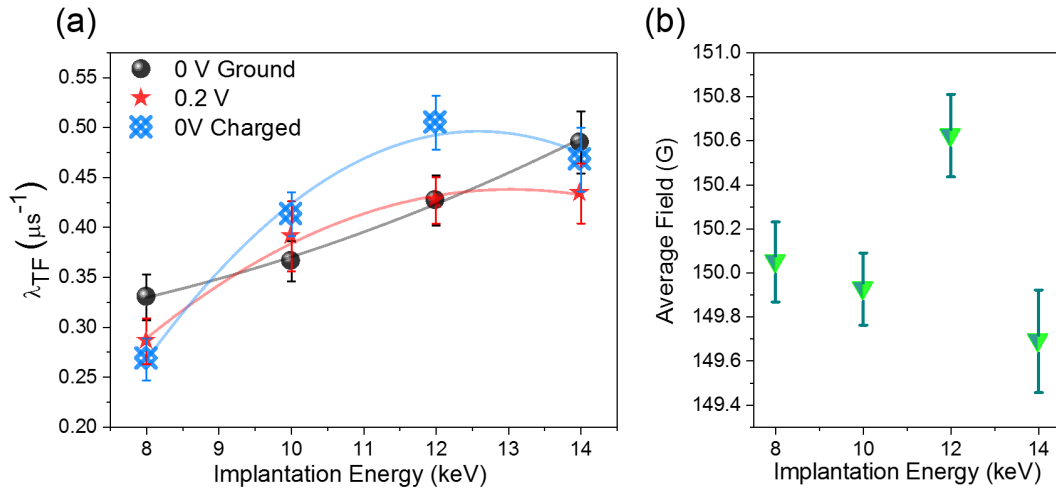


Figure 4.9: Implantation energy dependent measurements of the diamagnetic μ^+ precession in 150 G transverse field. (a) The muon depolarisation rate at the bottom $\text{MnO}_x/\text{C}_{60}$ interface is seen to increase by 18% in the charged state. (b) The local field averaged over the different electrical states with a maximum at the $\text{MnO}_x/\text{C}_{60}$ interface. Guides to the eye have been added in figure (a) for clarity.

4.4.3 LEM with optical excitation

It is clear from the study of metal-oxide/ C_{60} heterostructures with electrical charging that the use of LE- μ SR can provide invaluable information regarding the electronic and magnetic properties of the interfacial C_{60} following some perturbation, while also generating an understanding of the spatial localisation of these effects. In the electrically charged experiment, we have observed a $26 \pm 9\%$ increase in the $\text{Mu}@C_{60}$ frequency at the $\text{MnO}_x/\text{C}_{60}$ interface (12 keV). TF- μ SR measurements have indicated that in the charged state, a broadening of local magnetic field distribution at the $\text{MnO}_x/\text{C}_{60}$ interface has emerged following the application of a bias. This is supported

4.4 LE- μ SR studies of spin trapping at $\text{MnO}_x/\text{C}_{60}$ interface

by a $0.08 \pm 0.04 \mu\text{s}^{-1}$ increase in the μ^+ depolarisation rate at 12 keV. However, in TF we have not observed a measurable increase in the internal static field that can account for the increased ZF $\text{Mu}@C_{60}$ frequency through Zeeman splitting. The small changes observed in the previous experiment combined with the complexity of constructing tunnel junctions with the areas appropriate for muon measurements leaves room for some uncertainty regarding the significance of these results. As demonstrated in the measurements of photoluminescence over similar junctions with bias (see Fig. 4.3), current crowding in vertical junctions due to the relatively large lateral resistance of nm thick films is inevitable. It is likely then that current flow through the large area samples will be very inhomogeneous, with regions of the sample area becoming charged and contributing toward the changes in muonium precession frequency.

For this reason, a follow-up experiment was proposed to utilise the photovoltaic (PV) properties of the $\text{MnO}_x/\text{C}_{60}$ interface and the ability to illuminate a device with a wide laser beam spot (~ 2 cm diameter beam spot) without interfering with the μ SR technique. For this study, a PV sample was fabricated using similar methods to those described previously but with the structure: [Glass(Substrate)// Ta(5)/ Co(20)/ Ta(5)/ $\text{MnO}_x(10)$ / $\text{C}_{60}(100)$ / Cu(5)/ Au(15)] - thicknesses in brackets are in nm. The junction area for the device used in this experiment was $\sim 300 \text{ mm}^2$. The Ta(5 nm) spacer is added to decouple the MnO_x from the Co and to provide a cap against oxidation between fabrication steps. The use of the Cu(5 nm) layer ensures sufficient doping through surface charge transfer to obtain a photo-active device. During the μ SR experiment a blue laser ($\lambda = 470 \text{ nm}$) with an intensity of roughly $100 \text{ mW}\cdot\text{cm}^{-2}$ illuminates the sample while the photocurrent generated by the sample was recorded *in situ*.

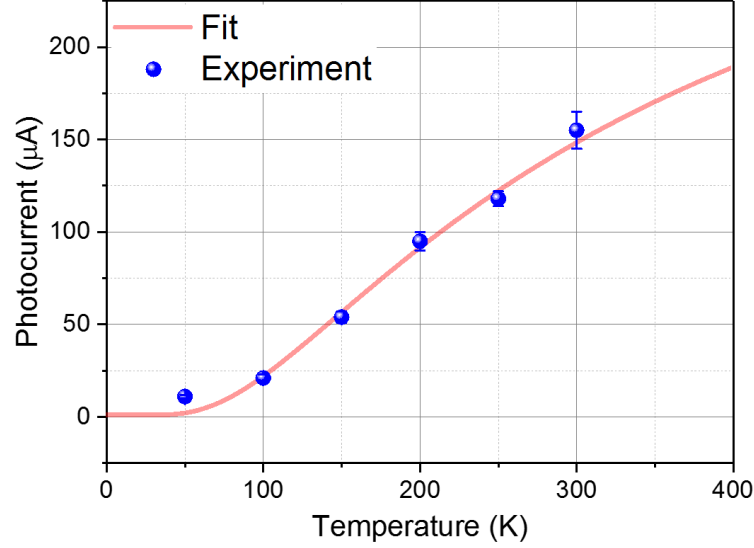


Figure 4.10: The temperature dependence of the short-circuit photo current for the sample used in the LEM experiment where a line of best fit with $\Delta = 25 \pm 1$ meV has been added in red.[182]

Fig. 4.10 shows the temperature dependence of the photocurrent measured simultaneously to the μ SR measurements. The observed temperature dependence is typical for the electronic transport properties of a molecular absorber material. Charge-carrier transport in molecular films such as C_{60} is characterised by variable-range hopping and is, therefore, thermally assisted. For these systems, the mobility is temperature dependent while the recombination of excitons on traps will negatively influence the photocurrent. In this case, the temperature dependence of the mobility should not affect the generated photocurrent under steady-state conditions. The strong temperature dependence should instead result from the liberation of charge carriers from trap states in the absorber material.[182] To show this, the data was fitted to the expression

$$I_{SC} = I_0 \cdot \exp\left(\frac{-\Delta}{k_B T}\right). \quad (4.4)$$

Here, I_{SC} is the short-circuit current, I_0 is a pre-exponential factor comprising the photogenerated charge-carrier density, their mobility and the electric field. Δ is the trap depth, k_B is the Boltzmann constant and T the temperature. Through fitting the data, an activation energy for traps of $\Delta = 25 \pm 1$ meV was obtained and a maximum

4.4 LE- μ SR studies of spin trapping at $\text{MnO}_x/\text{C}_{60}$ interface

generated photocurrent of $I_0 = 390 \pm 20 \mu\text{A}$ ($J_0 = 1.28 \pm 0.07 \text{ Am}^{-2}$) for this light intensity. The activation energy calculated here is in consonance with previously measured activation energies for studies of photogenerated charge carrier dynamics in C_{60} and other organic semiconductors.[183; 184]

With the expected behaviour obtained for the temperature dependence of a molecular photovoltaic, the sample was probed with implanted muons to study the effect of light irradiation upon the Mu@C_{60} precession. For this experiment, three implantation energies were chosen at 10.4, 13.65 and 15.25 keV. As shown in the simulated implantation profiles in Fig. 4.11(a), at 10.4 keV the implanted μ^+ particles sample only the molecular layer far away from the active interface. As the implantation energy is increased up to 15.25 keV, we approach the $\text{MnO}_x/\text{C}_{60}$ interface. It is made apparent by the depth dependence of the Mu@C_{60} precession shown in Fig. 4.10(c) that the closer proximity of the probed C_{60} layers to the FM electrode gives rise to substantial muonium precession frequencies ($\sim 1 \text{ MHz}$) close to the interface. The data here has been fitted with the single frequency model (Eqn. 4.1). The absence of a bias for this sample allows for the accumulation of charge during illumination also. When probing the $\text{MnO}_x/\text{C}_{60}$ interface with the 15.25 keV implantation energy, the zero field Mu@C_{60} precession frequency increases from $0.83 \pm 0.06 \text{ MHz}$ in the initial ground state up to $1.6 \pm 0.1 \text{ MHz}$ after illumination. This $90 \pm 10\%$ growth in the ZF Mu@C_{60} frequency represents a much more significant effect than what was observed for the electrically charged sample, where only a $26 \pm 9\%$ increase was observed. We attribute the improvement in the size of the effect to the higher density of accumulated spin-polarised charge owing to the greater uniformity in the way we charge the sample.

4.4 LE- μ SR studies of spin trapping at $\text{MnO}_x/\text{C}_{60}$ interface

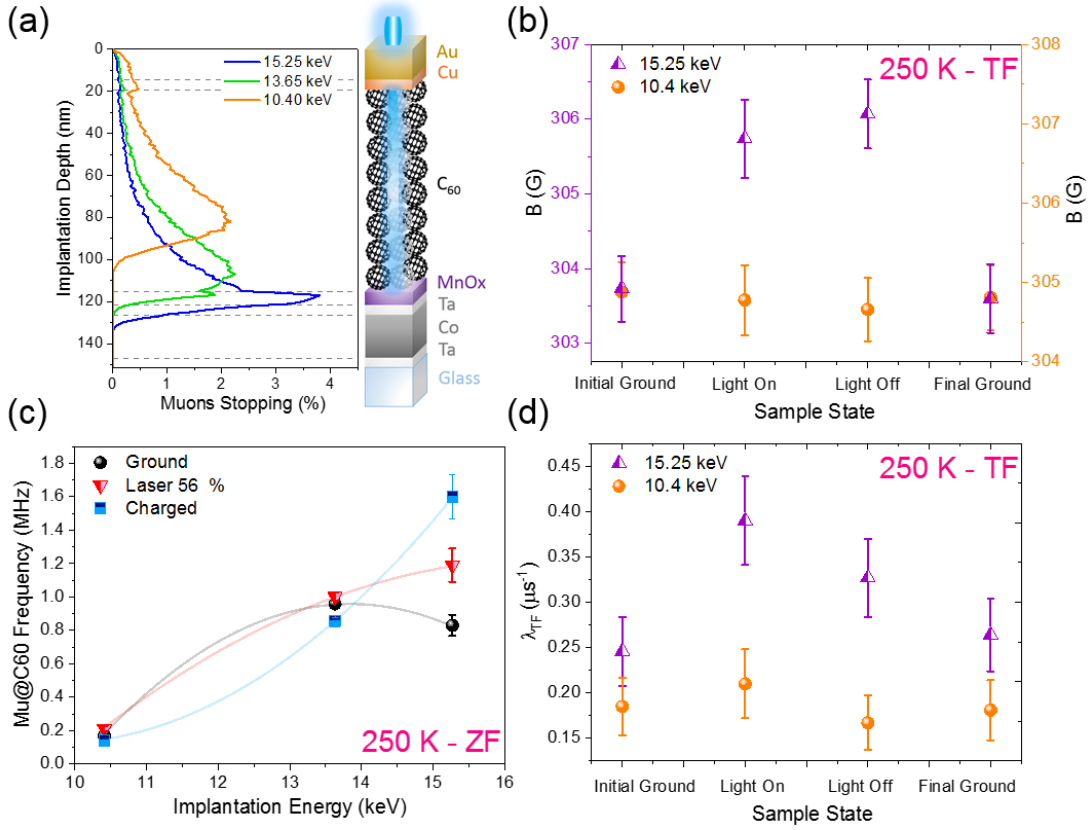


Figure 4.11: LE- μ SR on photovoltaic samples with optical irradiation. (a) The depth-dependent distribution of the implanted muons is shown for 10.40, 13.65, and 15.25 keV implantation energies. (b) The measured local field in a 300 G applied transverse field for different charge states of the sample. (c) The corresponding change in the zero field frequency of the Mu@C₆₀ precession, where changes are mainly observed at the MnO_x/C₆₀ interface (15.25 keV). (d) Changes in the depolarisation rate of the transverse field signal are shown with charge state. All measurements shown here were taken at 250 K. Guides to the eye have been added to (c) for clarity.

Measurements were taken in a transverse magnetic field of 300 G and are shown in Figs. 4.9(b, d). They reveal that the increase in Mu@C₆₀ frequency is accompanied by an increase in the local magnetic susceptibility at 15.25 keV. During and following the generation of a photocurrent, an increase in the local static field, \overline{B}_{local} , of 2.3 ± 0.6 G was detected at the implantation energy that correlates to the MnO_x/C₆₀ interface - corresponding to ordered moments $\sim 0.2 \mu_B$. [180] In this part of the sample ordered moments generate an increase in the local field which gives rise to a 0.20 ± 0.05 MHz

4.4 LE- μ SR studies of spin trapping at $\text{MnO}_x/\text{C}_{60}$ interface

increase in the μ^+ precession. Simultaneous measurements at 10.4 keV, where we are probing the centre of the C_{60} layer, showed no discernible change in the local magnetic susceptibility due to the generation of photocarriers. As shown in Fig. 4.12, control measurements on a sample without the MnO_x layer also showed no increase in the muonium precession due to illumination. Critically, these measurements once more demonstrate the reversibility of the effect. For the final grounded measurement both the local internal field and TF depolarisation rate return to their initial values.

To simultaneously assess the temperature dependence and reproducibility of this effect, further TF- μ SR data was taken with 15.25 keV for temperatures of; 50, 100, 300 and 200 K. For each measured temperature, \overline{B}_{local} was first measured in the initial ground state. Fig. 4.12 shows the changes in local field, $\Delta\overline{B}_{local}$, calculated w.r.t. the initial ground state measurement for each temperature. It can be seen that there is no conclusive temperature dependence. Instead, there is a dependence on the accumulation of spin-polarised charge on the number of read/write cycles performed, analogous to the read/write cycles used within standard flash memory. It can be seen that for the first three cycles, measured at 250, 50 and 100 K, the local static field is systematically larger in the charged (programmed) state than in the initial ground (erased) state. In the charged state, increases in \overline{B}_{local} of 2.6 ± 0.7 G and 1 ± 0.6 G are seen at 50 and 100 K respectively. After this, the device no longer shows any changes due to charge accumulation. This is likely due to photo-assisted degradation of the molecular film from the short wavelength laser used. Where data points are missing in the read/write cycle plot, muon precession data was not measured, but the sample still underwent the necessary grounding/illumination for the relevant read/write cycle.

4.4 LE- μ SR studies of spin trapping at $\text{MnO}_x/\text{C}_{60}$ interface

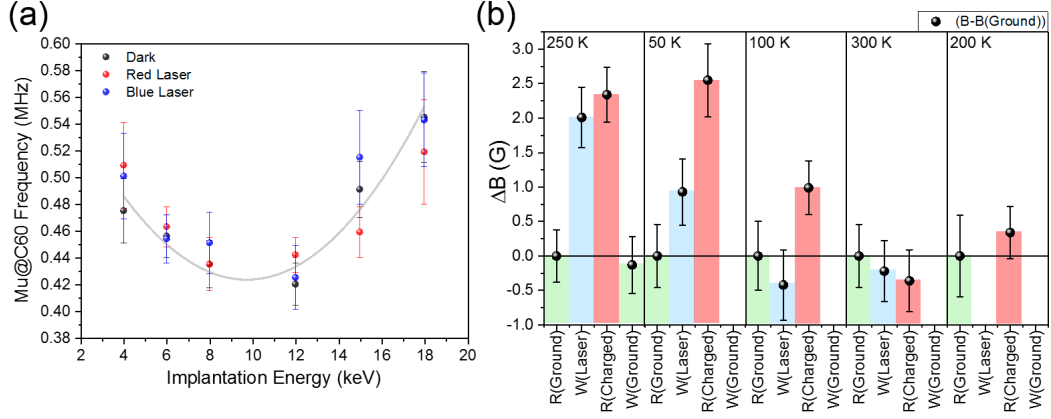


Figure 4.12: LE- μ SR on a multilayer thin film and photovoltaic device with optical irradiation. (a) The Mu@C_{60} frequency is measured for a heterostructure without MnO_x . The structure used here is $[\text{Si(Sub)}/\text{Ta}(3)/\text{Cu}(4)/\text{C}_{60}(110)/\text{Cu}(4)/\text{Au}(15)]$ where the thicknesses in brackets are in nm. The data presented here will be discussed in greater detail in Section 5.3. What is relevant for the discussion within this chapter, is the observation that the MuC_{60} frequency, for C_{60} molecules that are interfaced with a normal metal, is unchanged following optical irradiation. (b) Read/write cycles measured at different temperatures shows the reproducibility of the measured increase in \overline{B}_{local} , due to accumulated spin-polarised charge. For three read/write cycles, a larger \overline{B}_{local} is seen in the charged state than the initial grounded state.

The data gathered here is consistent with the emergence of spin-polarised states at the $\text{MnO}_x/\text{C}_{60}$ interface. The LEM studies presented here have been performed for two different device architectures and utilise two distinct methods of exciting the interface. In the electrically charged experiment, the 26% (~ 0.06 MHz) increase in the Mu@C_{60} frequency, measured at 12 keV, cannot decisively be attributed to Zeeman splitting originating from the accumulation of spin-polarised charge. Even though changes in magnetic texture at 12 keV are detected through the $0.08 \mu\text{s}^{-1}$ increase in μ^+ depolarisation rate, a measurable increase in the local static field is missing. This is in contrast to the optically charged experiment where a 90% (~ 0.8 MHz) increase in the Mu@C_{60} frequency was measured at the implantation energy corresponding to the $\text{MnO}_x/\text{C}_{60}$ interface (15.25 keV). In this case, we can confidently attribute the increased oscillation frequency to Zeeman splitting of the hyperfine coupling as a sizeable increase in \overline{B}_{local} of ~ 2 G was measured at 15.25 keV, whereas no change was seen elsewhere in the device. These results, therefore, provide compelling evidence

for the generation of spin-polarised states at the interface between MnO_x and C_{60} .

4.5 Discussion

We have observed profound changes in the orbital structure of C_{60} due to the trapping of charge in localised states at the $\text{C}_{60}/\text{MnO}_x$ interface. X-ray absorption measurements of the carbon K-edge show the generation of some hybrid orbital moment due to this trapped charge. XLD measurements show that the polarisation axis of this orbital responds to the application of a magnetic field. Room temperature DC-IV measurements of $\text{MnO}_x/\text{C}_{60}$ heterojunctions show interface-limited transport due to the formation of an interfacial dipole, which provides a mechanism for charge trapping by electrical or optical irradiation. Local magnetic characterisation of the charged state by LE- μ SR exhibited increases in the μ^+ precession, arising from emergent static fields of ~ 2 G, localised at the $\text{MnO}_x/\text{C}_{60}$ interface after optical irradiation. There was also an accompanying increase in the muonium oscillation frequency due to Zeeman splitting of the $\text{Mu}@C_{60}$ hyperfine levels. These observations demonstrate the direct measurement of static local magnetic fields generated by the spin-polarised accumulated charge.

To aid with the interpretation of this remarkable effect, density functional theory (DFT) calculations were performed by G. Teobaldi et al. Simulations were performed on a $\text{C}_{60}/\beta\text{-MnO}_2(110)\text{-}2\times 2$ interface. After the chemisorption of molecular C_{60} on the surface of $\beta\text{-MnO}_2(110)$ half-metallicity is observed in the MnO_2 band structure. The Fermi energy for spin down electrons is situated in an empty region of the density of states (DOS) but with available conduction states for spin-up electrons. The first monolayer of C_{60} that contacts the MnO_2 is conducting and spin-polarised, whereas the second C_{60} layer is only weakly bound to the first by van der Waals interactions and so retains its bulk band structure, with a gap between the HOMO and LUMO states. After the addition of 0.6 electrons per cage (in line with typical capacitance measurements of these systems) DFT calculations show that the molecular orbital states for the second molecular layer are downshifted by roughly 0.8 eV. This is in strong agreement with the emergence of the LUMO* peak in the NEXAFS measurements.

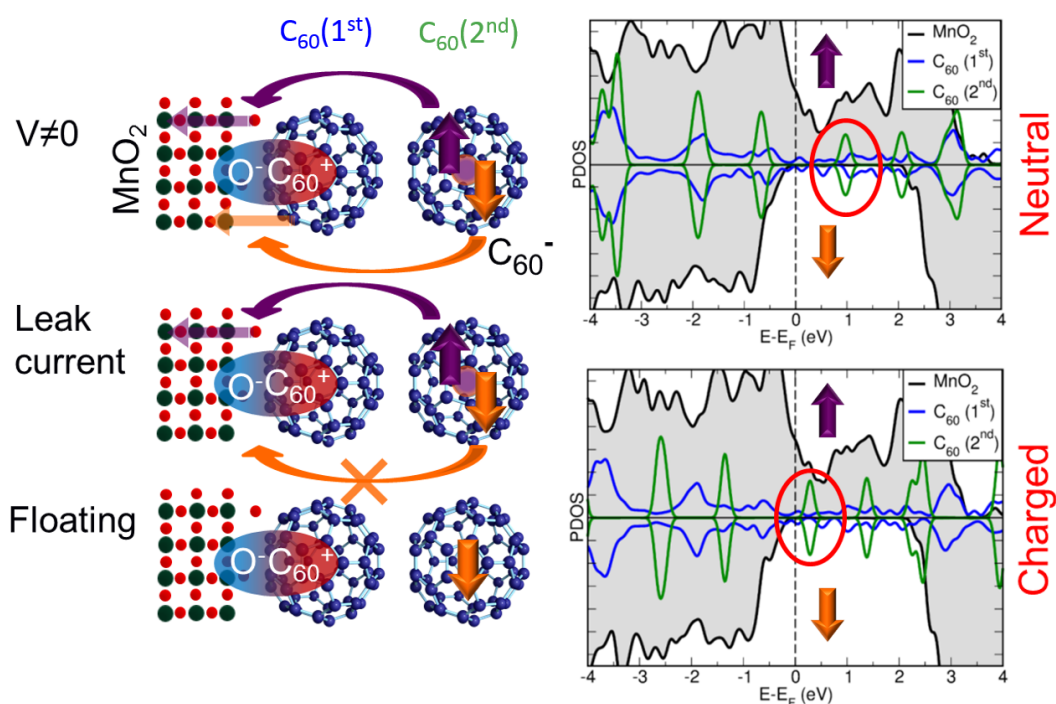


Figure 4.13: DFT calculations describing an ideal C_{60}/MnO_2 interface. The spin-polarised density of states is shown for pristine (neutral) and with $0.6 e^-$ added to the interface (charged). The formation of a $C_{60}-O$ bond at the interface leads to a strong interfacial dipole and the generation of half-metallic interface states which contribute to the accumulation of spin-polarised charge. Following the addition of $0.6 e^-$ to the system, the LUMO of the second C_{60} layer is downshifted by ~ 0.8 eV. Adapted from [149] where the calculations have been performed by G. Teobaldi et al.

It is possible then to use this idealistic model of the MnO_x/C_{60} interface to construct a mechanism by which spin-polarised charge is accumulated at this interface. Under an electric gradient charges will diffuse across the interface. When the voltage is removed, the shift in the LUMO close to the Fermi energy in the second C_{60} layer, coupled to the half-metallicity of the interface will lead to trapped spin down electrons as these cannot leak through the interface due to the absence of available spin down states. This is in contrast to the allowed diffusion of spin up electrons into the conducting DOS of the interface for spin up states. The device is therefore effectively acting as a capacitor where the accumulated charge, stabilised by the interfacial dipole, undergoes some spin-dependent leakage into the oxide with a decay time $\tau = RC$, where R

is the resistance and C is the capacitance. At low bias, the conductivity ($\sigma \propto \frac{1}{R}$) is governed by the transfer rate of electrons from interfacial C_{60} layers to the electrode.[185] For a spin conserving process such as a hopping event, we can approximate the spin-dependent transfer rate by Fermi's golden rule allowing the calculation of the zero bias conductivity for an electron moving from the C_{60} into the interface.[186] This is given as

$$\sigma = \sum_{\uparrow\downarrow} G^{\uparrow\downarrow}(E_F) = \frac{2\pi e^2}{\hbar} \sum_{\uparrow\downarrow} |T_{21}^{\uparrow\downarrow}|^2 \rho_2^{\uparrow}(E_F) \rho_1^{\downarrow}(E_F). \quad (4.5)$$

Here, $G^{\uparrow\downarrow}(E_F)$ is the spin-dependent conductivity, $T_{21}^{\uparrow\downarrow}$ is the transmission matrix element for an electron with spin \uparrow in the 2nd C_{60} layer tunnelling into the spin \downarrow band in the interface. $\rho_1^{\downarrow}(E_F)$ ($\rho_2^{\uparrow}(E_F)$) is the spin-split DOS in the initial (final) state. The conductivity for charges that are trapped and have the same spin polarisation as the minority band in the half-metallic interface will, therefore, be zero. This is the case for an idealised system, but the minority spin conductance will remain low for a spin-split interface. Measurements of the C_{60} K-edge showed a return to the pristine orbital structure for the C_{60} with increasing disorder of the magnetic cobalt electrode. Furthermore, XLD measurements of a device without a magnetic electrode demonstrated how the emergent orbital moment, formed after charge was trapped at the interface, could be aligned with the application of magnetic fields. It appears that the magnetisation of the magnetic electrode is critical to the accumulation of spin-polarised charge in this system. Future studies should include μ SR measurements of the charged state in samples that discard the magnetic electrode to provide a full picture of the role of the Co in the polarisation of the accumulated charge.

4.6 Outlook

In this chapter, we have devised a system which shows photovoltaic, spin filtering and capacitive behaviour. Critical to the described phenomena is the O- C_{60} bonding at the interface. The band bending due to the resultant dipole layer dramatically affects the optical and electronic properties of this system. It is known that transition metal oxides (TMOs) such as MnO_2 can be used for resistive switching memory devices.[187] The migration of oxygen ions in TMOs under an applied electric field leads to bistability

in the resistance of these systems. First achieved by Hewlett-Packard labs in 2008, this behaviour was seen for devices that included TiO_2 spacer layers.[188] This was the first demonstration of the proposed memristor device. After a decade of worldwide research on the topic, memristors have remained a hot topic as these two-terminal memory devices are believed to be applicable in the design of neuromorphic computing elements.[189]

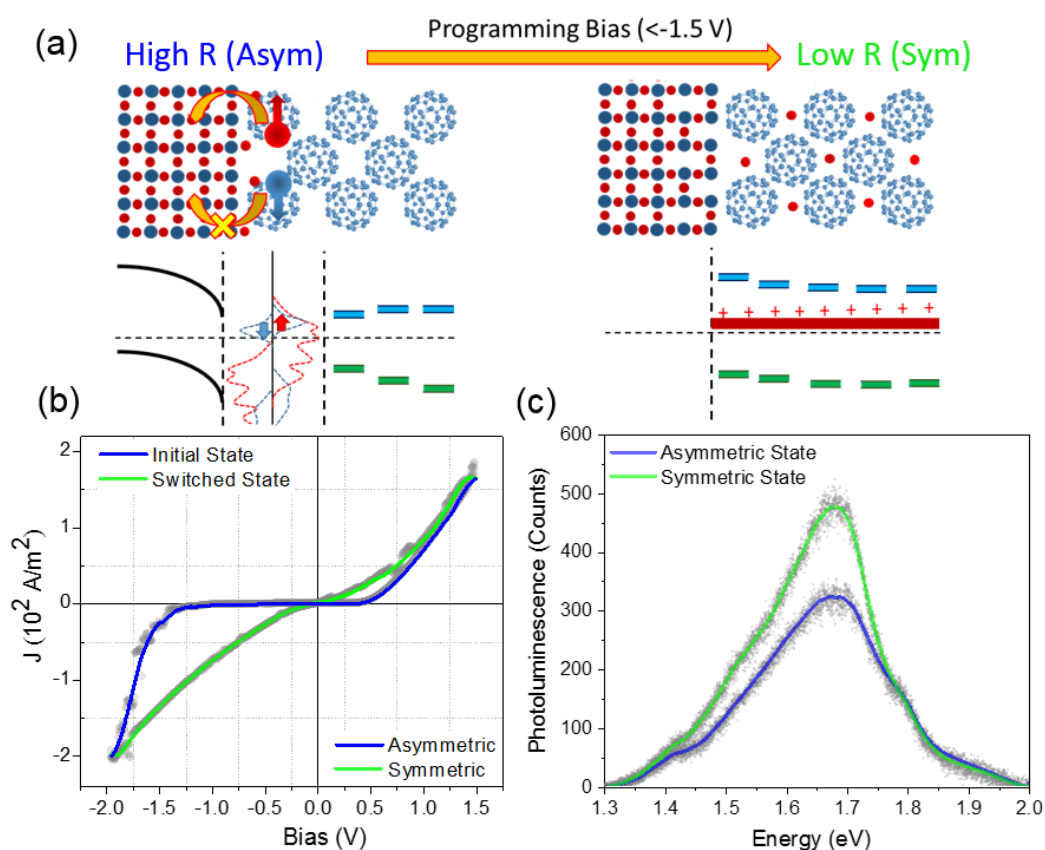


Figure 4.14: Tuning the energy level alignment of molecule/metal-oxide junctions with electro-migration of oxygen. (a) A schematic of the band structure before and after the application of a programming bias large enough to migrate surface oxygen away from the interface into the bulk of the molecular film. (b) RT DC-IV curve of a device which shows this resistive switching effect. (c) The measured C_{60} photoluminescence in the two states. The destruction of the interfacial potential after electro-migration of oxygen leads to a higher rate of radiative recombination.

The ability to manipulate the chemistry of TMO interfaces via the electro-migration of oxygen ions provides us with additional functionality for the $\text{MnO}_x/\text{C}_{60}$ system. As shown in Fig. 4.14, we are indeed able to change the electrical properties of the $\text{MnO}_x/\text{C}_{60}$ interface through the application of a programming voltage (~ 1.5 V), and reversibly switch from an initial asymmetric high resistance state (HRS) to a more symmetric low resistance state (LRS). The change in the DC-IV, shown in Fig. 4.14(b), demonstrates the destruction of the rectifying interfacial barrier and hence in-built potential. As shown in Fig. 4.14(c), measurements of the C_{60} photoluminescence at the junction area, in the two resistance states, confirm this. When the device is in the HRS, there is roughly $\sim 70\%$ of the luminescence measured as compared to the system in the LRS. When the sample is in the asymmetric HRS and is photo-active, the inbuilt potential at the $\text{MnO}_x/\text{C}_{60}$ interface separates excited e-h pairs reducing the efficiency of radiative recombination and hence the measured photoluminescence. These resistance changes are similar to what might be expected in a prototypical memristor device.[187]

The increased luminescence over the entire $100 \times 100 \mu\text{m}$ junction area in the LRS alludes to the uniform migration of oxygen into the C_{60} layer as opposed to the generation of metallic filaments within the oxide layer. In order to confirm this, transmission electron microscopy (TEM) was performed on $50 \mu\text{m}$ cross-sections, taken from devices that had been prepared into the two resistance states. The results of these measurements are shown in Fig. 4.15. For a sample in the LRS, shown in Fig. 4.15(b), There are no discernible variations in contrast within the MnO_x layer. The generation of metallic filaments would likely produce areas of greater density within the oxide. Elemental analysis provided by energy-dispersive X-ray spectroscopy (EDX) indeed shows a significant reduction in the oxygen atomic percentage for the LRS sample. The average stoichiometric ratio of oxygen to manganese appears to half in the interfacial oxide layer for a device that has been pre-prepared into the symmetric LRS prior to the creation of the TEM cross-section.

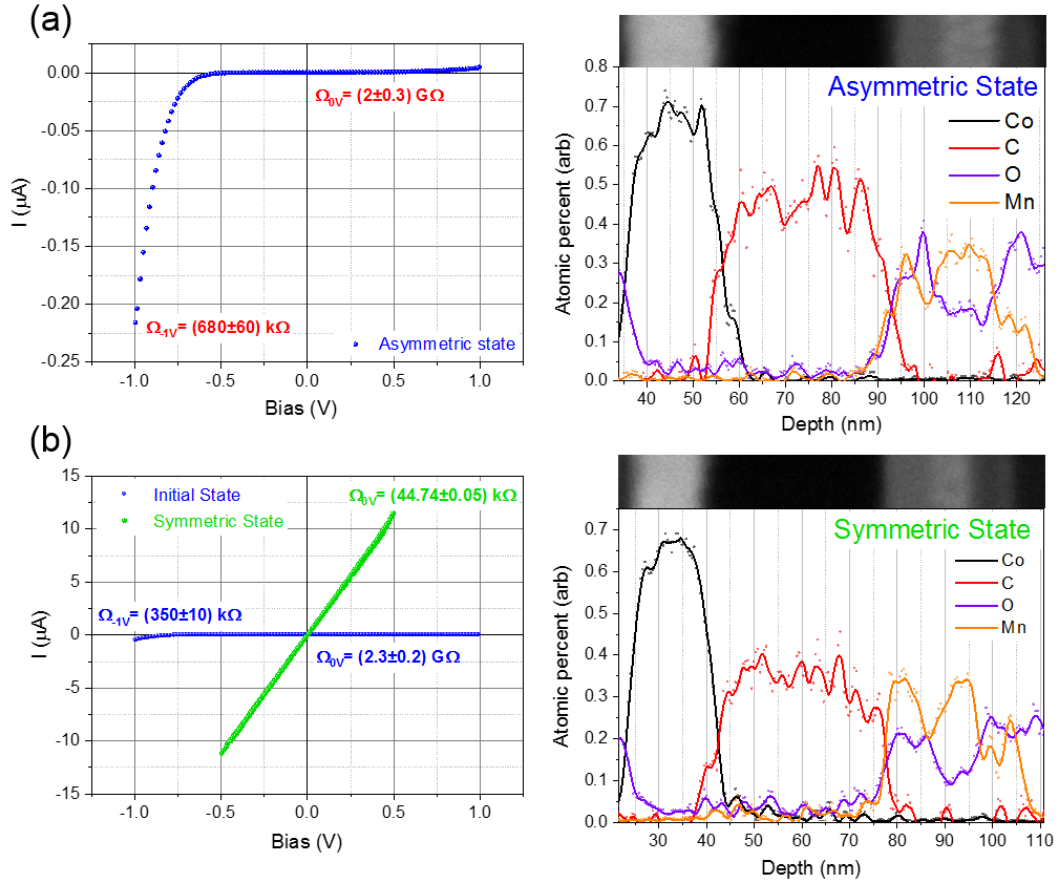


Figure 4.15: TEM-EDX measurements of devices in the two resistance states. (a) This first sample has been measured in the highly asymmetric resistance state before the programming voltage has been applied. (b) The second sample has been measured in the symmetric resistance state after the application of a programming voltage. A change in the oxygen concentration at the interface is observed which supports our model for electro-migration of molecular oxygen.

Through the electro-migration of oxygen in this system, we can tune the electrical properties of this interface by the elimination of the interfacial barrier and inbuilt potential. We can experimentally demonstrate the effect that this has on the optical properties of the device in Fig. 4.16. Photovoltaic maps were gathered by scanning a 633 nm laser, with an approximate beam spot size of 5 μm , over the device, while simultaneously recording the generated photocurrent. Through the application of bipolar programming voltage pulses between measurements, the device was prepared into the four resistance states shown in Fig. 4.16(b). It is clear from the spatial

dependences of the photocurrent, shown in the 3D plots in Fig. 4.16(c), that we can reliably turn on and off the photovoltaic efficiency through the migration of ionic oxygen away from the interface. Surprisingly, this happens very uniformly over the full device and so it may also be prepared into intermediate states where the diode behaviour is not entirely destroyed, such as in Fig. 4.16(c-ii). Such multi-switch behaviour is particularly critical in the formation of synaptic weights in neuromorphic computing as these have the role of assigning some probabilistic weighting to the amplitude of signals at each node within the network. This is analogous to the biological case where the signal strength across two neurons within a synapse is maintained by the composition within the synapse.[190] The gained advantage of producing a memristor which includes photovoltaic properties is the ability to read out the devices resistance state (synaptic weighting) in a non-destructive manner, such that there is minimised risk in the resistance state changing, which would ultimately lead to the degradation of stored data.[191]

It is typical for oxide materials, in particular, manganates such as LSMO, to be used as injector electrodes for organic spintronic devices, due to their large spin polarisations and resilience to ambient exposure. There have been multiple reports of the existence of resistance switching in such devices.[192; 193] It has also been suggested that the migration of oxygen into quinoline barrier layers is vital to the observed manipulation of the magnetoresistance strength. Interstitial oxygen in organic spacer layers leads to the formation of a valence band which is critical to the mechanism which governs the spin transport in the organic layers.[194; 195] It is clear then that such systems can display multiple phenomena where interfacial effects, such as those presented within this thesis, can be tuned through the electrical control of the interfacial chemistry. Future studies on such systems should, therefore, utilise the techniques discussed here to evaluate the non-volatile manipulation of spin-dependent hybrid interface states through the ionic control of the interface chemistry.

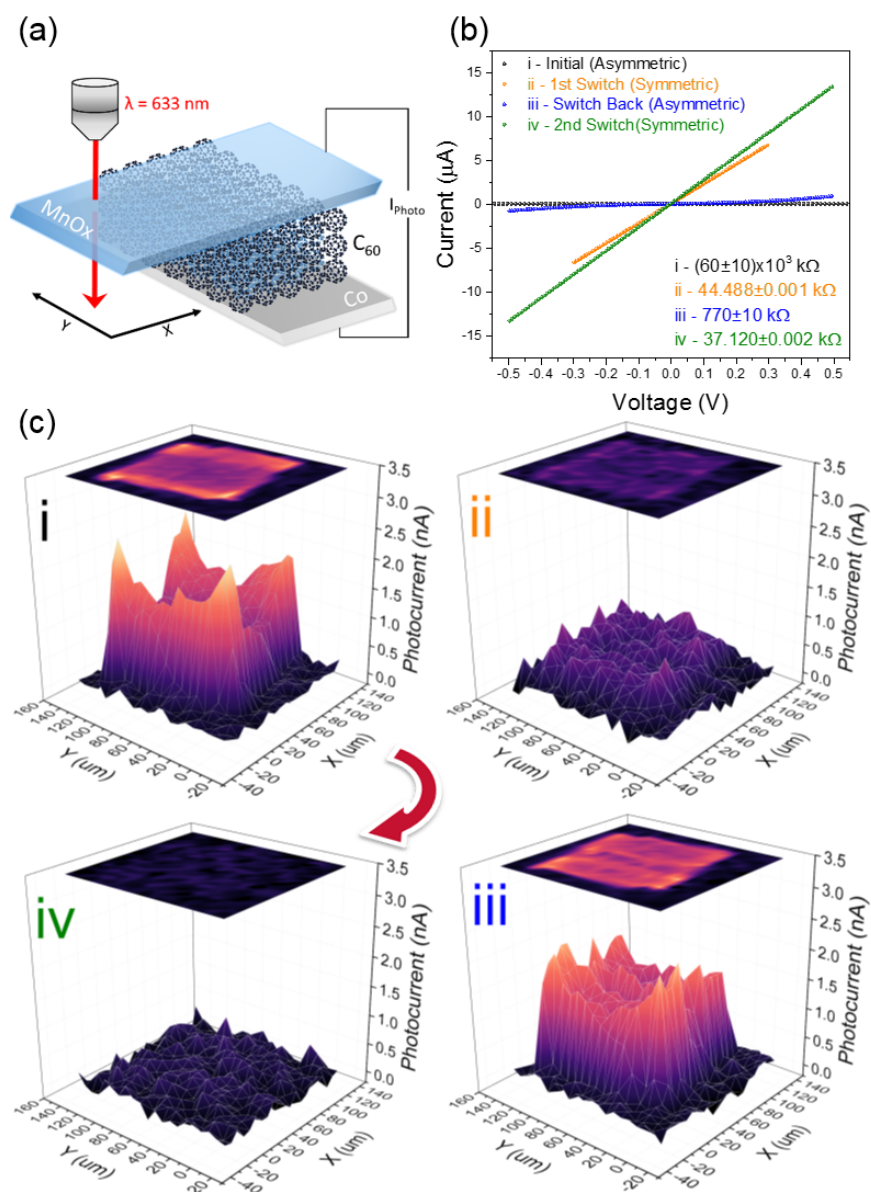


Figure 4.16: Manipulation of the photovoltaic efficiency through electro-migration of oxygen. (a) The experiment schematic shows how the laser map is taken over the active area of the device. (b) The four programmed resistance states for which the spatial dependence of the photocurrent was measured. (c) 3D plots of the photocurrent produced over the active junction area for the four resistance states. It is shown that the photovoltaic effect can be reliably tuned through ionic migration.

CHAPTER 5

Incorporation of spin-active metal/C₆₀
interfaces for superconducting
spintronics

5.1 Introduction

Spintronics typically relies on the manipulation of both charge and the quantum mechanical spin of the electron. In some systems, the transfer of spin can occur in the absence of a charge current. This provides a means to reduce energy losses generated through Joule heating.[196] Combining spintronics and superconductivity within the field of super-spintronics allows for the incorporation of phenomena that are only possible in a superconducting condensate such as spin-polarised supercurrents. The consolidation of these two fields would potentially enable much lower energy spin transfer and magnetic switching owing to the dissipation-less nature of quasi-particle mediated currents.[10] The realisation of super-spintronic devices requires the coalescence of both superconducting and ferromagnetic long-range order in a single system. According to conventional theories regarding the superconducting condensate, ferromagnetism and superconductivity are antagonistic states of matter. This is due to the ferromagnetic exchange field imparting a pair breaking effect upon spin-singlet superconducting pair correlations that possess opposing spin. Despite this, the theoretical prediction of spin-triplet pair states that may be produced through the design of superconductor/ferromagnet (S/F) interfaces, allows for a complete synergy between superconductivity and spintronics.

The possibilities of generating spin-triplet superconducting correlations in conventional S/F systems were first explored in the 2001 works of Bergeret et al.[8] and Kadigrobov et al.[9] and the 2003 work of Eschrig et al.[197]. Between these authors, a consensus was met that magnetic inhomogeneity at an S/F interface could theoretically promote the generation of a long-range $S_Z = \pm 1$ spin-triplet component (LRTC). Unlike spin-singlet and $S_Z = 0$ spin-triplet pairs, the LRTC facilitates the superconducting proximity of ferromagnetic layers. Being a fully spin-polarised paired state, they are also able to carry dissipation-less spin information, a very desirable property for the field of spintronics.

This chapter aims to show that the field of molecular spintronics can provide a novel contribution to the design of hybrid superconducting spintronic devices. Promise has already been shown in the synthesis of compounds where layers of

5.2 Low-temperature transport of SC-Molecular proximity structures

organic superconducting molecules and ferromagnetic metal complexes are used to chemically design material classes where superconductivity and magnetism are shown to coexist.[198] Nevertheless, the use of molecular spin-active interfaces coupled to conventional s-wave superconductors has not yet been explored. Within this chapter, hybrid superconductor/molecule/normal metal (S/M/N) systems are studied using transport measurements to show that the molecular C₆₀ layer can mediate the leakage of Cooper pair states via the proximity effect. A superconductor/molecule/spin-active-interface (S/M/I_{SA}/M/N) system is then probed by LE- μ SR in order to detect changes in superconducting pair correlations via an anomalous Meissner screening signal. In literature, similar screening signals have been assigned to the generation of odd-frequency spin-triplet pairs.[98–100] In the S/M/I_{SA}/M/N system, the spin-active ferromagnetic layer is provided by the weakly ferromagnetic state generated at the interface between C₆₀ and Cu (see Section 2.4.1).[21] In all instances, the superconducting film is chosen to be niobium as it is a conventional s-wave elemental superconductor, with a high T_C (relative to other elemental SCs) of around 9 K.

In this chapter, the work attributed solely to the author was all sample depositions, low-temperature characterisation, X-ray characterisation and fitting of μ SR data. LE- μ SR measurements were performed on the LEM beamline at PSI with the assistance of; O. Céspedes, S. Lee, R. Stewart, F. Al Ma’Mari, H. Bradshaw and local contact T. Prokscha.

5.2 Low-temperature transport of SC-Molecular proximity structures

The objective of this thesis chapter is to examine the use of thin-film C₆₀ based, spin-polarised metallo-molecular interfaces for the creation of spin-triplet superconducting correlations. To see if this goal can be met, we must first demonstrate the ability of thin film C₆₀ to mediate the leakage of Cooper pair states via the proximity effect. In order to observe the leakage of Cooper states into molecular structures and quantify the length scale over which the phase coherence is maintained, modifications of the SC gap energy via the inverse proximity effect were measured as a suppression in

5.2 Low-temperature transport of SC-Molecular proximity structures

the transition temperature. This technique has been routinely used to study proximity effects in S/N bilayer for several decades.[199]

The superconducting critical temperature (T_C) of S/M/N proximity stacks were obtained and normalised to that of a control Nb film ($S_{Control}$) that was grown on the same $8 \times 8 \text{ mm}^2$ Si/SiO₂(100 nm) substrate at the same time in the growth as the Nb layer used for the S/M/N stack. By using shadow masks, C₆₀(t) and Au(20 nm) films were deposited onto one of the Nb films to create the proximity stack, where $t = 0$ -80 nm. A 2 nm Al film is used to coat the whole substrate. This Al film oxidises in the atmosphere to create a passivated continuous film of alumina that will protect the uncovered Nb from oxidation and hence from changes in T_C due to the uncontrolled reduction in the effective thickness of the SC layer. A schematic of the $8 \times 8 \text{ mm}^2$ chip featuring both the S/M/N and $S_{Control}$ films is shown in Fig. 5.1(a). In this system, the normal metal has been chosen for its desirable properties for low energy muon spectroscopy, of which more shall be discussed in Section 5.4. As shown in Fig. 5.8, the superconducting coherence length for the sputtered Nb grown in this study has a typical value of $\xi = 9.32 \pm 0.06 \text{ nm}$, which is in consonance with literature values for thin-film Nb.[80; 81] The choice of a 50 nm Nb layer ensures that the two SC films will have the same superconducting properties prior to the addition of the C₆₀/Au layers. Films that are closer in thickness to ξ would have a greater sensitivity to proximity induced changes in the SC energy gap, and would, therefore, show a greater percentage T_C suppression. However, preliminary experiments that used thin (25-35 nm) films of Nb showed large (up to 5%) inconsistencies between the measured T_C s of the two films. As this fluctuation is of the same order of magnitude as the suppression in T_C we are trying to observe, 50 nm films of niobium were chosen in order to provide consistent control measurements.

5.2 Low-temperature transport of SC-Molecular proximity structures

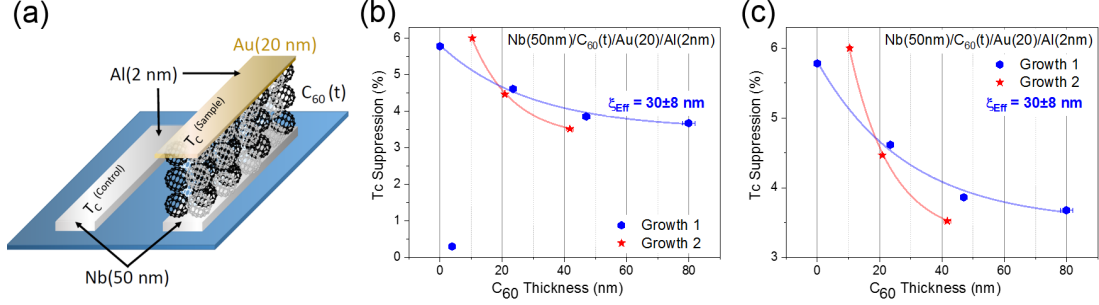


Figure 5.1: Low-temperature characterisation of hybrid superconductor/molecular heterostructures. (a) A schematic showing the fabricated sample which is grown alongside a control Nb film. (b) The dependence upon the T_C suppression with C_{60} thickness for Nb(50 nm)/ C_{60} (t)/Au(20 nm)/Al(2 nm) stacks. The modification of the SC gap energy via the inverse proximity effect is greatest for the sample without C_{60} . As a fullerene barrier layer is introduced and its thickness increased, the T_C never fully recovers to its pristine value. Therefore, there is a leakage of Cooper pair states into the C_{60} and through to the Au, where an effective length scale for the propagation cooper pairs has been found $\xi_{Eff} = 30 \pm 8$ nm. (c) A zoomed in version of Fig. (b).

The current biased, four-point resistance was measured as the samples were swept, at a rate of 0.2 K/minute, through the superconducting transition. The transition temperature for each sample was taken as the temperature at which the sample shows 50% of the normal state resistance. The uncertainty is then derived as the width of the transition, that is the temperature difference between 90% and 10% of the normal state resistance. The suppression in transition temperature has been expressed as a percentage difference w.r.t. the $S_{Control}$ film and is shown in Fig. 5.1(b). The results obtained for ‘Growth 1’ are shown in blue for 5 different C_{60} thicknesses (10 samples in total). For the sample with no molecular layer, where the C_{60} thickness is zero, a $5.78 \pm 0.01\%$ suppression in T_C is observed. As the molecular layer thickness is increased, the T_C suppression decays exponentially. Data gathered for a very thin layer of C_{60} ($t = 3.9 \pm 0.1$ nm) shows almost no T_C suppression. Sublimated C_{60} films of a thickness that is much less than 10 nm (~ 7 lattice units) will be expected to form islands and be discontinuous.[200] Indeed, for the devices grown for Chapter 4 the minimum C_{60} barrier thickness needed to obtain a working device is around 10 nm. It is very surprising that even though the C_{60} will be discontinuous, the leakage of Cooper pairs into the Au layer should be so suppressed. For this reason, this data

5.2 Low-temperature transport of SC-Molecular proximity structures

point has been left out of the fit (solid blue line). We have assumed a simple decay of the superconducting order parameter within the C_{60} as is appropriate according to G-L theory (as discussed in Section 2.6.2). This yields an effective coherence length within the molecular layer of $\xi_{Eff} = 30 \pm 8$ nm. It is evident that repeating this experiment (as depicted by ‘Growth 2’ on Fig. 5.1) yields reproducible results. However, it is clear that the decay length scale for ‘Growth 2’ is shorter than the first. In fact, $\xi_{Eff} \sim 10$ nm for ‘Growth 2’.

In order for superconducting phase information to be mediated through the molecular layer, there must be Andreev reflection occurring at the Nb/ C_{60} interface. The process requires that charge carriers in the C_{60} layer pair with electron states in the superconductor through the retroreflection of a hole (see Section 2.4). Therefore, the pair density on the molecular layer will be highly influenced by the presence of impurities, a tunnel barrier or any energetic boundaries. An interface transparency characterises such properties of an S/N interface. A perfect ohmic contact would have a highly transparent interface $T \simeq 1$. Whereas an S/N interface with some energetic barrier or higher impurity concentration would possess an interface transparency $T < 1$. The variation observed between ‘Growth 1’ and ‘Growth 2’ could then be in part due to inconsistencies of T and ξ_{Eff} between the two sample sets, perhaps due to slight differences in the morphology of the C_{60} layer, arising from inconsistencies in growth conditions. It is interesting to note that the observed quenching of the SC proximity for samples where the C_{60} is discontinuous could very likely be due to a decreased interface transparency where the molecular islands disrupt the Andreev reflection process. Therefore, future studies of this system should aim to replicate this trend with much greater thickness resolution between 0-20 nm in order to confirm whether a continuous C_{60} is, in fact, necessary for the propagation of Cooper pair states from the Nb substrate into the Au film.

The leakage of Cooper states has been observed in single molecule C_{60} .^[201] However, the effective length scale over which the phase coherence decays has not been studied in such depth. The band gap of C_{60} in bulk is about 2.3 eV. As an insulating material, it is then very surprising that Cooper pairs can maintain coherence up to 30 nm. It is expected that the electronic properties of C_{60} will be very different from the

5.3 Characterisation of the emergent magnetism at a Cu/C₆₀ interface by LE- μ SR

bulk when interfaced with metal surfaces owing to the metallisation of molecules due to charge transfer.[157; 202; 203] Indeed, the devices grown in Chapter 4 show dramatic variations in electrical properties between C₆₀ layers interfaced with metals or oxides. From the G-L derived description of the proximity induced phase coherence in a normal conductor, we expect the effective coherence length to be related to the electrical properties of the normal conductor:

$$\xi_{Eff} = \sqrt{\frac{\hbar v_F l}{6\pi k_B T_C}} \quad (5.1)$$

where v_F is the Fermi velocity. In the metallic alkali-doped fullerenes, mean free paths (l) between 0.6-1 Å have been reported.[204–206] This distance is considerably less than the C₆₀-C₆₀ separation of around 10 Å.[75] Therefore, even in these metallic fullerene systems, the carriers are highly localised and so the free electron model cannot really be applied. Nevertheless, if we were to apply such calculations to our system, estimating that l is comparable to the intermolecular lattice constant ($a \sim 1.4$ nm), a Fermi velocity, $v_F \sim 1.4 \times 10^7$ ms⁻¹ would be obtained. This corresponds to a carrier concentration in the molecular film of the order of 10²⁸ m⁻³. Consequently, the molecular layer appears to be highly doped in this system. Unfortunately, it is not possible to characterise the electronic properties of the C₆₀ layer here with transport measurements. In order to isolate the electrical properties of the molecular film from the metallic substrates, vertical junctions would need to be made. However, this would still not allow for Hall measurements to be taken to extract the real carrier concentration as any applied measurement current would shunt through the Au and Nb layers.

5.3 Characterisation of the emergent magnetism at a Cu/C₆₀ interface by LE- μ SR

This chapter utilises the emergent magnetic order produced in non-magnetic/molecular interfaces which have been studied within the thesis of F. Al Ma’Mari [207]. Previous studies on transition metal/fullerene interfaces have negated the presence of magnetic impurities and have highlighted the importance of interfacial coupling to the emergence of the magnetic state. Nevertheless, attempts made to attribute the magnetic

5.3 Characterisation of the emergent magnetism at a Cu/C₆₀ interface by LE- μ SR

signal to the C₆₀ film or transition metal by X-ray spectroscopy or polarised neutron reflectivity have been unsuccessful due to the lack of sensitivity and inability to probe deep within the sample. In this study, LE- μ SR has been used to provide a profile of the magnetism in a thin film Cu/C₆₀ system. Muons are highly sensitive to local field distributions and can come to rest at specified depths, determined by the use of transport voltages applied along the beam chamber. By using LE- μ SR, a full depth dependence of the magnetic texture can be obtained for these heterostructures.

For this study, a sample structure of [Si(Sub)/Ta(3)/Cu(5)/C₆₀(114)/Cu(5)/Au(14)] was used, where the thicknesses in brackets are in nm. Here, the Ta layer seeds the growth of the Cu film. The thickness of the Au layer was chosen to provide adequate moderation of the muon beam, whilst also protecting the sample against oxidation. As can be seen in Fig. 5.2(a), the molecular layer is of sufficient thickness to allow a highly resolved depth dependence of any effect of the Cu/C₆₀ interface upon the endohedral Mu@C₆₀ signal (see Section 3.6.2). The sample size used for this experiment was 15×15 mm². Counting times were reduced as this is comparable to the muon beam width ($d \sim 20$ mm), yet it is small enough for the thickness of the molecular layer to be homogeneous over the full film. Measurements were taken at 250 K, where the time scale of the rotation of the C₆₀ is short enough that the exohedral MuC₆₀ radical state does not contribute to the observed signal (see Section 3.6 for more details). During deposition, the sample was grown in a field of around 20 mT. The sample was first measured in zero field before any other magnetic field was applied to the sample. The time-dependent polarisation of the muonium state in ZF has been fitted with the damped oscillatory function used in Eqn. 4.1 in Section 4.4.1. This yields a muonium frequency, $\nu_{Mu@C_{60}}$, related to the transition between hyperfine levels (as discussed in 3.6.1). The depolarisation rate, $\lambda_{Mu@C_{60}}$, is also obtained. $\lambda_{Mu@C_{60}}$ characterises the distribution of hyperfine oscillations contributing towards the signal at any given implantation energy.

5.3 Characterisation of the emergent magnetism at a Cu/C₆₀ interface by LE- μ SR

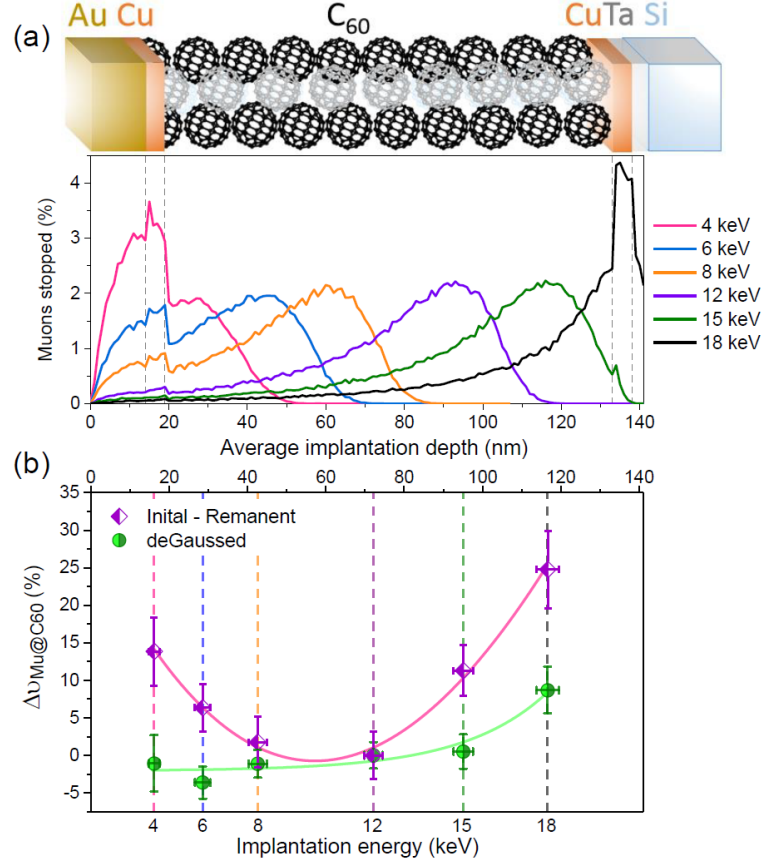


Figure 5.2: ZF-LEM measurements of the C₆₀ muonium frequency depth profile in a thin-film heterostructure. (a) The simulated implantation profile for a structure of [Si(Sub)/Ta(3)/Cu(5)/C₆₀(114)/Cu(5)/Au(14)], where the thicknesses in brackets are in nm. At the 4 and 18 keV implantation energies, a considerable percentage ($\sim 57\%$ and 34% respectively) of muons stop in the metal layers. As the measurement was performed in ZF, these are not expected to contribute to the oscillating signal. (b) The obtained depth dependence of the relative change in Mu@C₆₀ oscillation frequency, $\Delta\nu_{Mu@C60}$, for the initial state measurement and following a degauss of the sample and magnet. $\Delta\nu_{Mu@C60}$ has been calculated relative to the Mu@C₆₀ frequency at 12 keV.

Fig. 5.2(b) shows the dependence of the percentage change in Mu@C₆₀ frequency, $\Delta\nu_{Mu@C60}$, with implantation depth. The average implantation depth has been calculated from the simulated stopping profiles shown in Fig. 5.2(a). $\Delta\nu_{Mu@C60}$ has been calculated relative to the Mu@C₆₀ frequency obtained at 12 keV, as this is the implantation energy that captures the centre most region of the stack. In the initial

5.3 Characterisation of the emergent magnetism at a Cu/C₆₀ interface by LE- μ SR

measurement, where the sample is in the as-grown state, a curved profile of muonium frequency is observed with depth. $\nu_{Mu@C_{60}}$ is higher at the top and bottom interfaces by $14\pm 5\%$ and $25\pm 5\%$ respectively. From this measurement alone, it is clear that towards the C₆₀/Cu interfaces, there is a change in the hyperfine splitting between Mu@C₆₀ spin configurations. It is known that at C₆₀/metal interfaces, chemical interactions, in addition to lattice reconstruction of the metal surface, lead to charge transfer from the metal into the first monolayer of the fullerene.[208–211] As the neutral C₆₀ LUMO is triply degenerate, the addition of charge will be accompanied by a molecular distortion that will act to break this degeneracy through the Jahn-Teller effect.[121] The reduced symmetry brought about by the molecular distortion would then impart some anisotropy onto the hyperfine coupling tensor, which describes the energy splitting in zero field of the triplet muonium spin configurations. This is the cause of the observable 0.7 MHz ZF oscillation in the oblate molecule, C₇₀.[175]

There are two considerations for the interpretation of the initial state measurement. Firstly, it could be that charge-induced distortions of the molecules cause the upturn in muonium frequency towards the metal/C₆₀ interfaces due to an increased anisotropy in the hyperfine tensor. Secondly, as we expect a magnetic interface to form for continuous films of Cu in contact with C₆₀, this profile in the muonium frequency could be directly related to the magnetic field profile within the sample where the muonium hyperfine levels now experience some Zeeman splitting. These considerations need not be mutually exclusive, as both may contribute to the observed muonium frequency profile. In order to examine these possibilities, an in-plane magnetic field of 30 mT was applied to sample. This field is much greater than the typical coercive field ($H_C \sim 5\text{-}10$ mT) seen in these systems.[65] The field was then degaussed back to zero field in order to demagnetise the sample. Following this degauss procedure, the depth profile of the muonium frequency dramatically changes. As shown in Fig. 5.2(b), $\nu_{Mu@C_{60}}$ now remains almost constant throughout the molecular layer increasing only by $9\pm 3\%$ at the depth closest to the bottom Cu/C₆₀ interface. The fact that there is no change in $\nu_{Mu@C_{60}}$ at the top Cu/C₆₀ interface in this new magnetic state suggests that the charge-induced distortions of the interfacial molecules do not have a sizeable effect on the measured muonium signal. This leads us to the conclusion that the increased $\nu_{Mu@C_{60}}$ frequency in the interfacial regions of the sample is a direct

5.3 Characterisation of the emergent magnetism at a Cu/C₆₀ interface by LE- μ SR

consequence of Zeeman splitting of the muonium hyperfine levels due to stray field originating at the Cu/C₆₀ interface. Indeed, the guide to the eye shown in Fig. 5.2(b) (solid pink line) has been obtained through a 3rd order polynomial fit which would be expected for a dipolar field that originates at and is highly localised to, the Cu/C₆₀ interface. Following the degauss, the remaining $9\pm 3\%$ increase in $\nu_{Mu@C_{60}}$ at the bottom Cu/C₆₀ interface is likely to be due to some residual magnetisation, where the interfacial moments have not been entirely disordered.

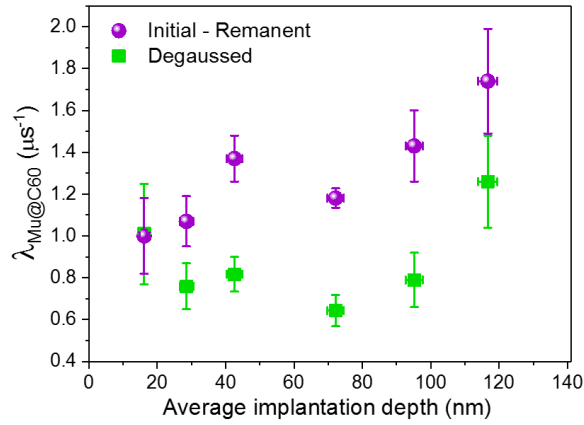


Figure 5.3: ZF-LEM measurements of the C₆₀ muonium frequency depth profile in a thin-film heterostructure. The depth dependence of the Mu@C₆₀ depolarisation rate, $\lambda_{Mu@C_{60}}$, for the initial state measurement and following a degauss of the sample and magnet.

The behaviour of the depolarisation rate within this sample is shown in Fig. 5.3. $\lambda_{Mu@C_{60}}$ characterises the distribution in hyperfine coupling strengths over the stopping profile at a given implantation energy. An increase in $\lambda_{Mu@C_{60}}$ could, for instance, be generated when the internal field is changing with depth (stray field) or if the shape of the C₆₀ molecules are not constant within the probed depths due to molecular distortions. The degauss procedure has a clear effect on the depth dependence of $\lambda_{Mu@C_{60}}$. The main observation is a reduction in $\lambda_{Mu@C_{60}}$ of up to $0.5\pm 0.1 \mu s^{-1}$ for the central part of the sample. We have established that for the initial measurement, the trend in the data arises from a decaying magnetic field within the C₆₀ layer. The reduction in $\lambda_{Mu@C_{60}}$ over the central molecular region can, therefore, be understood as a reduction in the field distribution at these depths. This is further

5.3 Characterisation of the emergent magnetism at a Cu/C₆₀ interface by LE- μ SR

evidence that it is a stray field, originating at the interface, which causes the divergence in muonium oscillation frequency for the initial state measurement.

Despite the evidence for the allocation of this muonium frequency profile to emergent magnetic effects arising at the Cu/C₆₀ interface, this study raises questions regarding the formation of magnetic domains within these structures. If a ferromagnetic thin film has been demagnetised, then all that has taken place is the formation of domains, as is required to reduce the overall magnetostatic energy. The magnetisation of each domain would be of the same size as the saturation magnetisation. Therefore, at the length scale over which a muon senses its magnetic environment, there should be little change in the local field magnitude for a demagnetised state compared to a remanent one. The fact that in this system, local fields are eliminated through demagnetisation suggests that the system is a disordered magnetic system such as a spin glass or superparamagnet. As we are using the C₆₀ muonium state to sense such changes in local fields, the size of the individual magnetic units must be of the same order as the C₆₀ molecule itself ($d \sim 1$ nm). The increase in the depolarisation rate towards the Cu/C₆₀ interfaces for the degaussed state is characteristic of disordered local moments.

In our previous work, thin-film scandium interfaced with C₆₀ demonstrated thermal hysteresis in ZFC-FC magnetometry measurements. Such behaviour is indicative of metastable magnetic systems such as superparamagnets or spin glasses.[65] In previous studies on Cu/C₆₀ interfaces, on the other hand, behaviour that is more characteristic of ferromagnetism is displayed. The interfaces formed for this study are unlike those used before as they only comprise a single C₆₀ interface.[21] Therefore, the sample does not produce a magnetic moment large enough to be measured by SQUID VSM magnetometry. This means that the mechanism governing the magnetism shown in this experiment cannot simply be studied using SQUID VSM magnetometry techniques. Future work could aim to characterise in greater depth the spin relaxation processes at these interfaces with LE- μ SR. However, the apparent blocking temperature for these systems, being above room temperature, is in a range that is incompatible with the μ SR technique.[65]

5.4 Anomalous screening effects measured by LE- μ SR

We have so far shown that in S/M/N heterostructures, where the molecular layer is C_{60} and the normal metal is Au, a superconducting state can be induced within the C_{60} over an effective coherence length of around 30 nm. We have also explored the magnetic texture of the emergent magnetic state that forms at C_{60} /Cu interfaces with low energy muons. We, therefore, have a system that can support the leakage of superconducting correlations whilst also generating a spin-active interface under the right conditions. In the following study, we aim to demonstrate that the combination of these two systems supports the coexistence of the two states of matter. The diffusion of Cooper pairs through a spin-active interface has been shown to lead to the generation of spin-polarised odd-frequency pairs.[212; 213] Odd-frequency pairs allow for the coexistence of ferromagnetism and superconductivity as the parallel spin alignment of the triplet pair is not susceptible to the pair breaking effect due to the exchange field within the ferromagnet. In order to experimentally determine the effect of a spin-active molecular interface on the diffusion of Cooper pairs through C_{60} films, we have elected to measure these systems with LE- μ SR. Low energy muons have been used for the characterisation of many superconducting systems as they can be tuned to particular depths, giving very high magnetic sensitivity and spatial resolution. In S/F bilayers the emergence of spin-polarised correlations among other exotic screening effects have been successfully examined by the LE- μ SR method.[100–102]

For this study, two multi-layered heterostructures were deposited on $15 \times 15 \text{ mm}^2$ Si/SiO₂ substrates. The samples had nominal structures of:

1. S/M/N:

Nb(50)/ C_{60} (30)/Au₁(10)/ C_{60} (20)/Au₂(10)/ C_{60} (20)/Au₃(10)

2. S/M/I_{SA}/M/N:

Nb(50)/ C_{60} (15)/Cu(4)/ C_{60} (15)/Au₁(10)/ C_{60} (20)/Au₂(10)/ C_{60} (20)/Au₃(10)

where thicknesses in brackets are in nm. The thickness of the Nb layer was chosen to be less than the expected penetration depth ($\lambda \sim 90 \text{ nm}$). This ensures that the contribution to the μ^+ precession signal from the conventional Meissner effect is minimised and guarantees that no vortices are able to form in-plane. These effects

5.4 Anomalous screening effects measured by LE- μ SR

would convolute any interpretation of magnetic signals measured below the Nb critical temperature. For this experiment, we have inserted three 10 nm Au films into the structure. This is because muons that stop within these layers will exhibit a slow depolarisation of the μ^+ spin. A muon that has been implanted into a normal metal (absent of magnetism) shall be depolarised by the nuclear moment, intrinsic to that metal. The nuclear moment for Nb is large at $6.17 \mu_N$, μ_N being the nuclear magneton. Whereas, the nuclear dipole moment for Au is much less at $0.15 \mu_N$.^[214] When combined with its high density, Au becomes a very attractive material for studies involving low energy muons. The high density leads to a very narrow stopping distribution for the muon beam within the metal whilst the low nuclear moment means that a thermalised μ^+ particle can undergo numerous precession periods about a local static field without becoming depolarised. Through the use of 10 nm Au layers in these heterostructures, we generate deterministic stopping sites for the muon beam where we can very sensitively measure small changes in local field distributions due to superconducting screening effects. In both structures, there are three possible Au layers available to probe any screening effects. Nevertheless, this study only examines the Au layer that is closest to the SC layer (Au₁).

The second sample used in this study has a very similar structure to the first but now includes the continuous spin-active film of Cu/C₆₀. The thickness of the C₆₀ layers in both samples have been designed such that the separation between Au and Nb in both structures are very similar. A 15 nm C₆₀ film has been deposited either side of the Cu film as this ensures a continuous, smooth molecular film for the Cu deposition. The choice of this thickness has also been engineered with consideration for the extracted coherence length of C₆₀ (30 nm). If the molecular layer were much thicker than this, then no Cooper pairs would arrive in the Au probe layer and hence no screening effects would be observed.

The magnetic and structural properties of the two samples were characterised by SQUID VSM and XRR prior to the muon measurements. Characterisation measurements were performed on ‘sister samples’ grown at the same time as the LEM samples but on $4 \times 4 \text{ mm}^2$ substrates, suitable for the XRR and SQUID VSM instrumentation. The obtained X-ray reflectivity curves and moment vs field data for the sample

5.4 Anomalous screening effects measured by LE- μ SR

with(without) Cu is shown in blue(pink) within Fig. 5.4. The solid line in the XRR curve has been obtained by fitting the data with GenX.[114] The structural parameters obtained through fitting are displayed in table 5.1. The lattice constant for C₆₀ is around 14 Å. The obtained rms roughness (σ_{rms}) for all layers within each stack possess an intrinsic roughness of around one lattice unit of C₆₀ when deposited on the fullerene. Importantly, the Cu layer thickness is greater than $2\sigma_{rms}$ and so is continuous. Another critical outcome of the fitting is the fact that there is very little change in morphology in the Au₁ layer. As we shall be comparing the screening currents within this layer, having structural consonance between the two samples is vital. The GenX fits obtained for the two samples describes the data sets remarkably well with minimal deviation from the nominal structures. Using these structural parameters, we can perform Monte-Carlo simulations to accurately describe the muon stopping profile using TrimSP.[215]

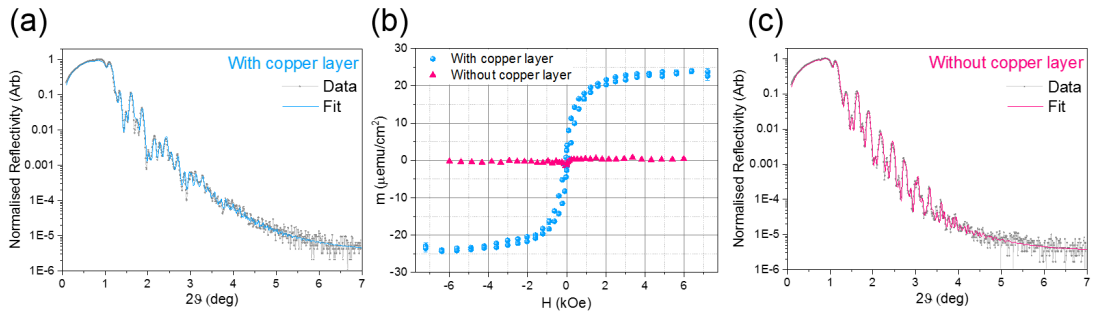


Figure 5.4: Characterisation performed on the ‘sister samples’ of those measured by low energy muons. (a) The normalised XRR measurement is shown for the sample with a magnetic Cu layer. (b) SQUID VSM data is shown for the two sister samples, where a linear background has been subtracted. The sample with a Cu layer has an emergent moment per unit area, $m = 24 \pm 1 \mu\text{emu}\cdot\text{cm}^{-2}$. The sample without a Cu layer has a moment, $m = 0.4 \pm 0.2 \mu\text{emu}\cdot\text{cm}^{-2}$, that is likely an artefact of the measurement. The magnetic moment has been normalised to the film surface area as the true thickness of the magnetic layer cannot be guaranteed. (c) The normalised XRR for the sample without the Cu layer. For both films, a fit to the XRR data has been achieved with GenX.[114]

5.4 Anomalous screening effects measured by LE- μ SR

	S/M/I _{SA} /M/N		S/M/N	
	d[σ] (nm)	Density (%)	d[σ] (nm)	Density (%)
Au₃	10.1[0.6]	97 \pm 1	9.8[1]	98 \pm 1
C₆₀	20.3[1]	73 \pm 20	20[1.7]	87 \pm 9
Au₂	9.5[1]	100 \pm 1	9.3[1]	96 \pm 3
C₆₀	20.9[1]	96 \pm 1	20.6[1.7]	110 \pm 30
Au₁	10.4[0.9]	103 \pm 9	10.8[0.9]	100 \pm 3
C₆₀	15.7[1]	131 \pm 3	32.4[1.6]	100 \pm 10
Cu	4.1[2]	106 \pm 60	N/A	N/A
C₆₀	16.9[2]	127 \pm 30	N/A	N/A
Nb	53.2[0.9]	96 \pm 1	53.3[0.8]	90 \pm 4

Table 5.1: Structural parameters obtained for the S/M/I_{SA}/M/N and S/M/N hybrid proximity stacks, fabricated for study with low energy muons. The XRR data has been fitted with GenX to find the film thickness (**d**), rms roughness (σ) and density. The density has been presented as a percentage w.r.t. the bulk. Importantly, it is seen that there is very little change in the morphology of layer Au₁ after the addition of the thin Cu layer.

The RT magnetometry data in Fig. 5.4(b) shows how the addition of the thin Cu layer leads to an emergent magnetic signal. Here, the moment has been normalised to the sample area as the effective thickness of the magnetic layer depends on the localisation of the magnetic ordering. This is something that, experimentally, has been difficult to probe. There is strong theoretical support for the magnetic hardening of Cu substrates due to a combination of lattice expansion and π -3d_z hybridisation with accompanied charge transfer.[211] Whilst the observations from LEM in Section 5.3 support this, the observation of a spin-split C₆₀ LUMO by XMCD in a similar transition metal/fullerene system suggests that the magnetism could also be located at the interfacial states produced between these two materials.[65] The sample with the Cu/C₆₀ possesses a moment per area, $m = 24 \pm 1 \mu\text{emu}\cdot\text{cm}^{-2}$, which equates to a volume magnetisation of $60 \pm 3 \text{emu}\cdot\text{cm}^{-3}$ if one assumes the magnetic order is

5.4 Anomalous screening effects measured by LE- μ SR

purely localised to the Cu layer. The sample without Cu shows a background signal of $m = 0.4 \pm 0.2 \mu\text{emu}\cdot\text{cm}^{-2}$ which is of the same magnitude as the resolution of the instrument. It is, therefore, considered to be an artefact of the measurement.

LE- μ SR measurements were performed on the two samples. In both cases, screening currents are generated by the application of a 300 G transverse field. In transverse field, the transitions between different spin configurations of the muonium state happen on a time-scale that is shorter than the resolution of the timing instrumentation. Therefore, we are only sensitive to the precession of the diamagnetic μ^+ particle. For all LEM measurements, the sample was cooled through T_C in the applied transverse field. The time-dependent polarisation ($A_S(t)$) of the muon can be described as

$$A_s(t) = A_{\mu^+} \cos(\gamma_{\mu} \cdot \bar{B}_{local} \cdot t + \varphi) \exp(-\lambda_{TF} \cdot t), \quad (5.2)$$

to yield the local field (\bar{B}_{local}), depolarisation rate (λ_{TF}), asymmetry (A_{μ^+}) and phase (φ). φ is the starting phase of the μ^+ spin polarisation at time $t = 0$. This initial μ^+ spin polarisation depends on the time of flight of the accelerated μ^+ particle which in turn depends on the implantation energy. A_{μ^+} will also be energy dependent as it parametrises the magnitude of the μ^+ precession signal. For implantation energies where a greater proportion of the muons thermalise within C_{60} , a reduction in A_{μ^+} would be expected due to the formation of muonium. As both of these parameters are expected to be independent of temperature (they were indeed verified to be so), they could be fixed at the value obtained in the normal state for each implantation energy.

Measurements were performed at 9, 12 and 20 keV. These energies were chosen to probe local screening effects in the Au_1 layer and within the Nb. Table 5.2 shows the simulated fractions of muons stopping within each layer of the sample for 9, 12 and 20 keV. At 9 keV, there are a similar fraction of muons stopping within the Au_1 layer for both samples. There will also be contributions to the signal from μ^+ particles stopping in layers Au_2 and Au_3 , while none are stopping in the Nb layer. The rest of the muons are expected to stop in the molecular layers and as such do not contribute to the TF signal due to the formation of muonium (see Section 3.6.2). This shows that at 9 keV, we are probing almost identical environments within the two samples whilst being unaffected by the Nb layers. Therefore, with this choice of implantation energy,

5.4 Anomalous screening effects measured by LE- μ SR

we are able to decouple the signal arising from screening within the Au probe layer from the superconducting substrate. At 20 keV there is only a small contribution to the signal from the Au layers and so the TF signal will be dominated by the Nb layers. At this energy, there is a 10% difference in the number of muons stopping within the Nb layers of each sample due to the inclusion of the Cu layer. We will later show that this discrepancy can be accounted for when interpreting the screening effects in the two Nb layers, using the analysis conveyed in Fig. 5.8.

	Muon stopping fractions (%)						TF signal contribution (%)					
	S/M/I _{SA} /M/N			S/M/N			S/M/I _{SA} /M/N			S/M/N		
	9 keV	12 keV	20 keV	9 keV	12 keV	20 keV	9 keV	12 keV	20 keV	9 keV	12 keV	20 keV
Au₃	4	3	1	4	3	1	9	7	1	9	8	1
C₆₀	15	7	2	15	7	2	0	0	0	0	0	0
Au₂	13	6	2	13	6	2	31	15	4	30	18	3
C₆₀	34	24	5	33	23	5	0	0	0	0	0	0
Au₁	25	26	4	26	25	3	60	64	6	61	72	5
C₆₀	2	21	7	3	31	16	0	0	0	0	0	0
Cu	0	6	3	N/A	N/A	N/A	0	14	5	N/A	N/A	N/A
C₆₀	0	3	13	N/A	N/A	N/A	0	0	0	N/A	N/A	N/A
Nb	0	0	58	0	1	68	0	0	84	0	2	91

Table 5.2: Simulated fractions of muons stopping within each layer of the sample for 9, 12 and 20 keV acceleration voltages. The transverse field signal contribution is the percentage of muons stopping within each layer normalised to the sum of particles stopping in metallic layers, as particles which stop in the molecular layers are not expected to contribute to the TF signal. The values highlighted in red clarify which layers dominate the TF signal at 9 and 20 keV.

The dependence of \overline{B}_{local} with temperature for the sample without the spin-active Cu/C₆₀ interface is shown in Fig. 5.5(a). At 20 keV there is a clear reduction in the internal field arising from the conventional Meissner effect as the sample is cooled through the critical temperature ($T_C \simeq 8.7$ K). The base temperature for the cold finger cryostat used in this experiment is around 2.7 K. At this temperature there has been a 2.41 ± 0.08 G reduction in the internal field w.r.t. to the normal state measurement at 10 K. When probing the Au layer at 9 keV, the internal field shows no significant change

5.4 Anomalous screening effects measured by LE- μ SR

until the lowest temperature measured where a 0.21 ± 0.08 G reduction in field is observed. Although this reduction is small, it exceeds the statistical error derived through the fitting of the data. As the distance between the Nb substrate and Au layer is comparable to the effective coherence of the proximitised C_{60} , it would be expected that any leakage of Cooper pair states into the Au would be small. For a larger Meissner signal, a sample where the thickness of C_{60} is far smaller than ξ_{Eff} should be measured. Ideally, a cryostat that can obtain lower base temperatures than 2.7 K would also be used. The size of the local screening current should theoretically increase with the amplitude of the superconducting order parameter which would be expected to increase with reducing temperature.[216]

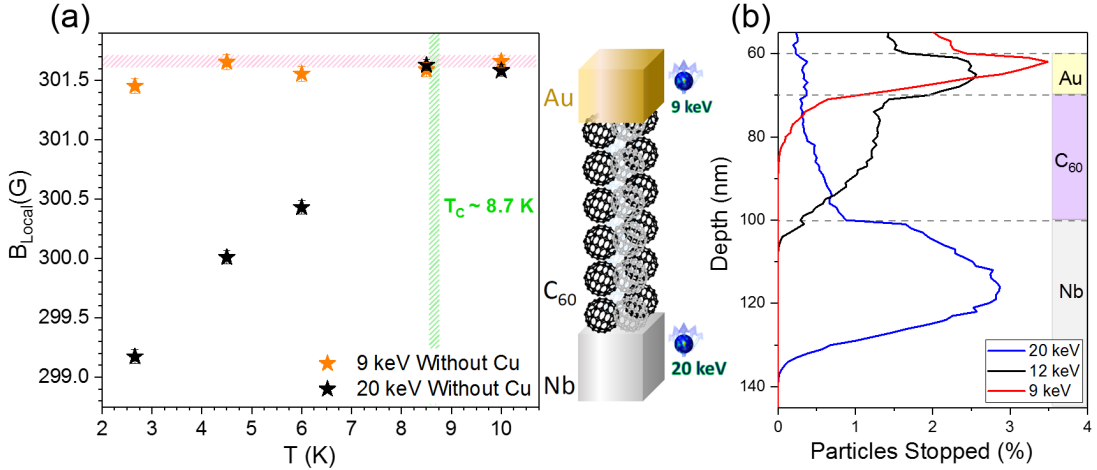


Figure 5.5: LEM measurements of screening effects in a hybrid proximity stack without a Cu layer, where the full structure is shown in table 5.1. (a) The temperature dependence of the measured local field in a 300 G applied transverse field. Far below the niobium T_C (~ 8.7 K), a small reduction in \overline{B}_{local} is observed at a 9 keV implantation energy. This small Meissner screening originates from the leakage of Cooper pair states through the C_{60} and into the Au layer. At 20 keV, muons are predominantly stopping in the Nb layer. Therefore, a large conventional Meissner effect is observed. (b) Simulated stopping profiles show that at 20 keV muons mostly stop in the Nb film. At 9 keV the muons mainly stop within the closest Au layer. Importantly, at the lower energy, no muons are implanted into the Nb film.

Fig. 5.6 shows the temperature dependence of \overline{B}_{local} for the sample that contains the spin-active Cu/ C_{60} interface. There is a clear suppression in the size of the Meissner screening measured at 20 keV. The reduction in the local field at 20 keV

5.4 Anomalous screening effects measured by LE- μ SR

is now 0.96 ± 0.08 G. However, the 9 keV measurements now show a paramagnetic signal as an increase in local field of 0.28 ± 0.08 G is observed. This sample also shows an anomalous temperature dependence of the Meissner effect. The T_C of this sample was measured to be comparable to the control sample without Cu ($T_C \simeq 8.7$ K). Nevertheless, at T_C , there isn't an immediate reduction in the local field as would be expected from the onset of the superconducting gap and creation of singlet Cooper pair states. Instead, at 20 keV there is a possible small increase in field just below T_C (8-8.5 K) which eventually becomes diamagnetic below 6 K. The 9 keV data, by contrast, appears to show what could perhaps be an oscillating dependence but one that is out of phase with the 20 keV measurements. Due to a lack of adequate statistical fidelity, we cannot assert any behaviour in the data between ~ 7 -8.5 K as the size of these changes is equal to that of the uncertainty in the fits.

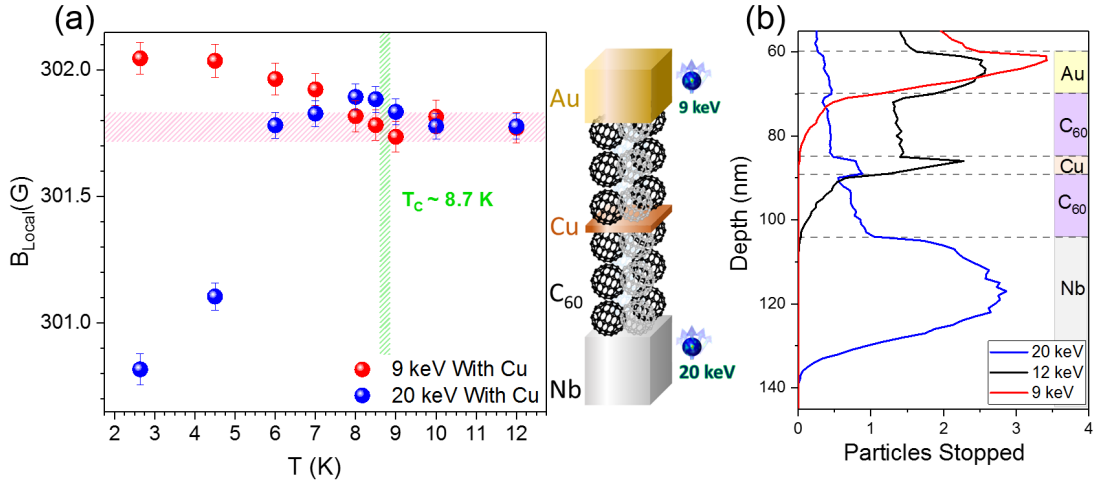


Figure 5.6: LEM measurements of screening effects in a hybrid proximity stack with a magnetic Cu layer, where the full structure is shown in table 5.1. (a) The temperature dependence of the measured local field in a 300 G applied transverse field. Below the niobium T_C (~ 8.7 K), an increase in \overline{B}_{local} is observed at 9 keV implantation energy. This paramagnetic Meissner screening appears to slightly oscillate below T_C and then saturate at around 5 K. At 20 keV, a conventional Meissner effect is still observed, but the magnitude of the reduction in \overline{B}_{local} is roughly half compared to the sample without the magnetic Cu layer. (b) Simulated stopping profiles show that the depth dependence of the muon implantation is unaffected by the inclusion of the Cu layer.

5.4 Anomalous screening effects measured by LE- μ SR

We can obtain further information regarding the local field distribution by analysing the depolarisation rates of the μ^+ particle. Fig. 5.7 shows the temperature dependence of λ_{TF} for both samples for 9 and 20 keV. The effect of the Nb nuclear moment upon the muon polarisation can be seen as in the normal state, $\lambda_{TF}(9 \text{ keV}) \sim 0.04 \mu\text{s}^{-1}$. Whereas, $\lambda_{TF}(20 \text{ keV}) \sim 0.2 \mu\text{s}^{-1}$. From the temperature dependence, it again appears that the conventional Meissner response has been suppressed until lower temperatures for the sample with Cu. For the 20 keV measurement, $\lambda_{TF}(6 \text{ K})$ is very similar to that obtained for $\lambda_{TF}(T_C)$. In contrast, $\lambda_{TF}(6 \text{ K})$ is roughly $0.04 \mu\text{s}^{-1}$ larger than $\lambda_{TF}(T_C)$ for the system without Cu. The temperature dependence of λ_{TF} for the 9 keV data is too noisy to interpret. There seems to also be an upwards trend in λ_{TF} below T_C for both samples. However, this only implies a broadening of the field distribution at this part of the sample. At such close proximity to the Nb substrate, λ_{TF} can be influenced by the redistribution of flux within and outside the SC layer. Therefore, the temperature dependence of λ_{TF} at 9 keV is inconclusive.

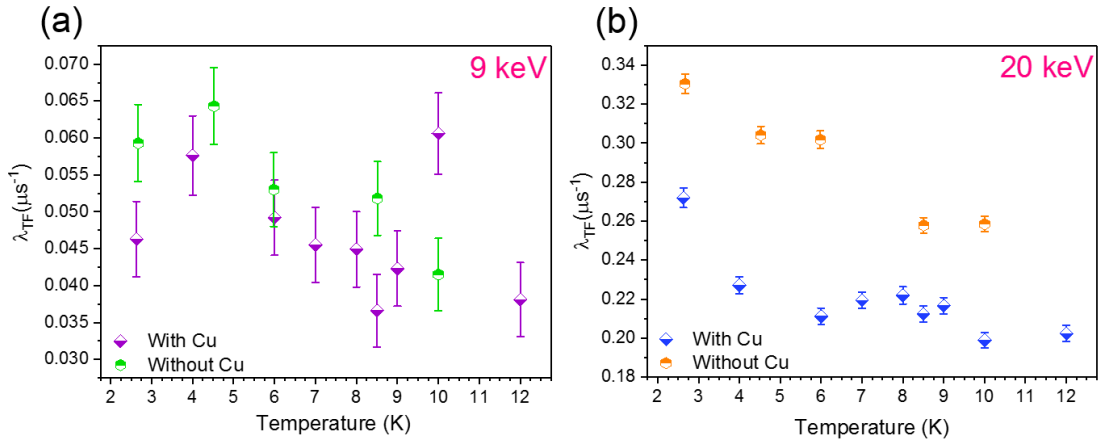


Figure 5.7: LEM measurements of screening effects in hybrid proximity stacks, where the full structures are shown in table 5.1. (a) The temperature dependence of the μ^+ depolarisation rate, λ_{TF} , for the 9 keV measurements for both structures. (b) The temperature dependence of the μ^+ depolarisation rate for the 20 keV measurements. In the superconducting state, increases in the muon depolarisation rate are expected due to a broadening in the field distribution at the μ^+ site arising from the screening currents at the surface of the superconductor.

5.4 Anomalous screening effects measured by LE- μ SR

It is possible to model the observed flux expulsion measured within the superconductor. Following on from the London equation (see Section 2.6.1), the expected flux profile within the superconductor is given by

$$B(x) = B_0 \cosh\left(\frac{x}{\lambda(T)} - \frac{d_s}{2\lambda(T)}\right) \cosh\left(\frac{d_s}{2\lambda(T)}\right)^{-1} \quad (5.3)$$

where x is the position within the superconducting film, $x = 0$ corresponding to the top surface. d_s is the Nb thickness, given by the GenX XRR fitting parameters found in table 5.1. B_0 is the flux outside the superconductor, which in this case has been obtained from the normal state measurement at 12 K.[101] In these systems, the muons stop over a very broad range of depths. In order to obtain the values of x for which we wish to simulate the expelled flux, the stopping distribution inside the Nb has been evaluated with a Gaussian fit where the peak position has been interpreted as the most probable stopping site of the muon. Fig. 5.8(b) shows the simulated muon stopping distribution for the two samples. For the sample without Cu, a modal stopping depth of $x_{WithoutCu} = 14.3 \pm 0.2$ nm is obtained. Whereas, for the sample with Cu, $x_{WithCu} = 10.8 \pm 0.2$ nm is obtained. It is clear that the addition of the thin Cu layer merely acts to shift the implantation profile by 3.5 ± 0.3 nm.

For superconducting films, the temperature dependence of the penetration depth is critically dependent upon the electrical properties of the material. To know which behaviour we are to expect, we must first establish whether we are in the diffusive (dirty) or ballistic (clean) regime (see Section 2.7). Through the fitting of the temperature dependence of the out of plane critical field, $H_{C2\perp}(T)$, the Ginzburg-Landau (GL) coherence length at 0 K, ξ_{GL} , can be extracted:[217]

$$H_{C2\perp}(T) = \left(\frac{\phi_0}{2\pi\xi_{GL}^2}\right) \left(1 - \frac{T}{T_C}\right), \quad (5.4)$$

where ϕ_0 is a flux quantum. Fig. 5.8(a) shows the $H_{C2\perp}(T)$ phase diagrams for a batch of nominally 50 nm niobium films. We obtain an average GL coherence length of $\xi_{GL} = 9.32 \pm 0.06$ nm. We may also estimate the mean free path (l) in our films through the relationship,[218]

$$\frac{1}{\xi(l)} = \frac{1}{\xi_0} + \frac{1}{l}. \quad (5.5)$$

5.4 Anomalous screening effects measured by LE- μ SR

Here, the coherence length for pure niobium (Pippard coherence length) $\xi_0 = 38$ nm.[219] We obtain a mean free path $l = 12.3 \pm 0.1$ nm which is in line with reported values for sputtered niobium.[220] These Nb films are, therefore, in the diffusive regime (dirty limit: $l < \xi_0$). The temperature dependent field penetration depth $\lambda(T)$ in the dirty limit is given by

$$\lambda(T) = 0.62\lambda_0 \left(\frac{\xi_0}{l} \right)^{\frac{1}{2}} \left(\frac{T_C}{T_C - T} \right)^{\frac{1}{2}}. \quad (5.6)$$

Combining Eqns. 5.3 and 5.6 allows for the simulation of the flux expulsion within the superconducting layer. We have now established values for; x_{WithCu} , $x_{WithoutCu}$, ξ_0 , l and d_s . Only λ_0 , the zero kelvin field penetration depth, remains to be evaluated.[221]

Fig. 5.8(c) displays the collated temperature dependence of the local field obtained for both samples where the local field has now been normalised to the normal state value (B_0). There are only three data points gathered below T_C for the 20 keV measurement of the sample without Cu. Consequently, it is inappropriate to fit for λ_0 . However, we may estimate a suitable range for $\lambda_0 \simeq 145 \pm 10$ nm, being appropriate values of the field penetration depth for niobium films of this thickness, that are in the diffusive regime.[222] It is evident from the pink shaded region that the observed flux expulsion for the sample without Cu can be successfully simulated with physically appropriate parameters. The blue shaded region on the same figure utilises the same model, assuming the identical range of values which λ_0 can take. For this simulation, the position in x has just been shifted by 3.5 nm towards the niobium top surface as evident from Fig. 5.8(b). From the significant disparity between the measured data for the sample with Cu at 20 keV and the model, it is clear that the minor shift in the muon stopping profile cannot fully explain the large observed suppression in the Meissner screening in the near surface region of the Nb film.

5.4 Anomalous screening effects measured by LE- μ SR

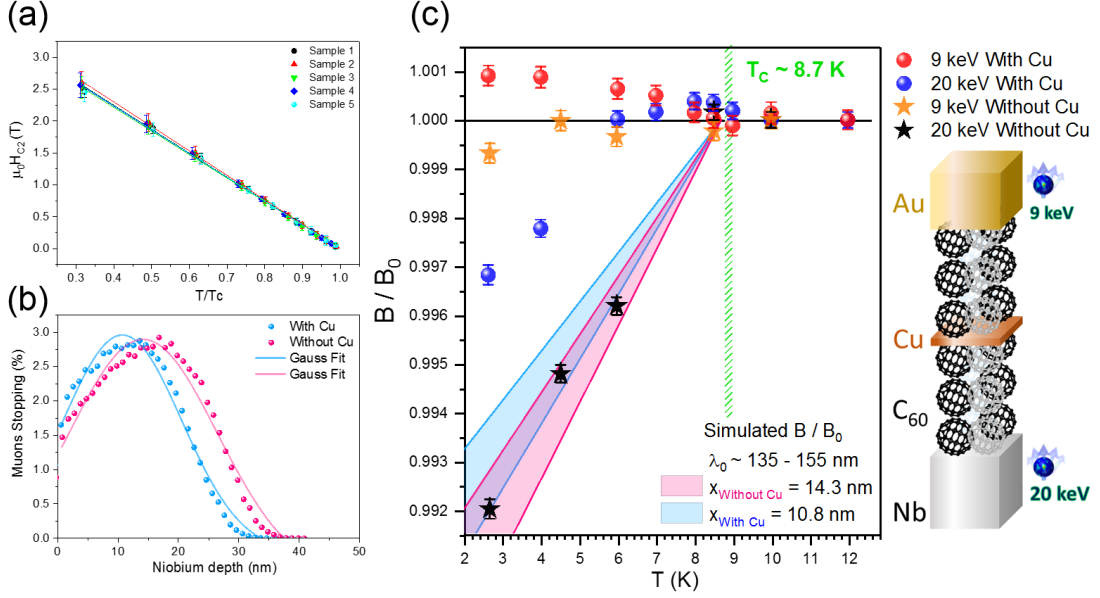


Figure 5.8: Simulating the expulsion of magnetic flux from the near-surface regions of samples measured with LEM. a) $H_{C2\perp}(T)$ phase diagrams for nominally 50 nm films used to extract the effective coherence length $\xi_{GL} = 9.32 \pm 0.06$ nm and hence the mean free path $l = 12.3 \pm 0.1$ nm via Eqn. 5.5. b) The stopping distributions for LEM samples using the structural parameters given in table 5.1. Only the distribution of muons stopping in the SC layer is shown. Through a Gaussian fit of the implantation profile, it can be seen that the distribution is shifted towards the top surface for the sample with Cu by 3.5 ± 0.3 nm. c) The collated temperature dependent \bar{B}_{local} measurements for the LEM samples where the blue(pink) shaded areas show the simulated expulsion of flux for the sample with(without) Cu, assuming a λ_0 between 135 and 155 nm.

It has been suggested the creation of spin-triplet pairing states at S/F interfaces can suppress the magnitude of the conventional Meissner effect.[98] The London theory provides the famous expression for the supercurrent density, \mathbf{j} , due to a magnetic vector potential, \mathbf{A} (see Section 2.6.1). \mathbf{j} can be rewritten in terms of singlet (n_s) and triplet (n_t) densities:[223]

$$\mathbf{j} = -\frac{e^2(n_s - n_t)\mathbf{A}}{mc}. \quad (5.7)$$

Therefore, in a system where purely odd-frequency correlations exist, a paramagnetic susceptibility ($\chi > 0$) can be expected.[99] The observation a paramagnetic

5.4 Anomalous screening effects measured by LE- μ SR

screening signal by Di Bernardo et al. in Nb/Ho/Au stacks was indeed interpreted as a spatially varying change in $(n_s - n_t)$.[100] This study lacks the systematic temperature dependence of the effect which has been captured in the presented experiment. In the theoretical proposal of this effect by Yokoyama et al. an oscillatory dependence on temperature is expected.[98] Such an anomalous dependence has indeed been observed in this case. This gives strong support for the creation of odd-frequency spin-triplet pairs at a spin-active molecular interface.

We can aid the interpretation of the paramagnetic signal arising due to the creation of odd-frequency pairs by attempting to rule out other possibilities that could contribute to such an effect. One such possibility is that we are observing flux which has been trapped due to inhomogeneities in the niobium crystal lattice.[224] Pinned flux in mesoscopic superconducting systems have indeed produced an observable paramagnetic screening signal.[225–227] However, the trapped flux is only metastable and is understood to be due to sample morphology rather than being an intrinsic property of the condensate. In our samples, we have shown with XRR that there is no measurable difference in the morphology of the metallic layers between both samples. Therefore, as no such effect was observed in the sample without the spin-active interface, this effect is unlikely to be due to flux pinning in the SC layer for the spin-active sample.

Moreover, we observe the strongest paramagnetic signal in the Au layer, where we are not sensitive to the screening effects from the Nb. The addition of vortex cores or trapped flux in the near surface region of the niobium layer would undoubtedly lead to a broadening of the field distribution below T_C . We would, therefore, expect a larger depolarisation rate to be seen below T_C for the spin-active sample both at 9 and 20 keV. As shown in Fig. 5.7, this is not the case. There is no statistically significant difference in λ_{TF} between the two samples at 9 keV. While at 20 keV, λ_{TF} is smaller in the spin-active sample at all temperatures. Therefore, the paramagnetic effect we observe cannot be attributed to penetrating vortex cores or flux compression.

5.4 Anomalous screening effects measured by LE- μ SR

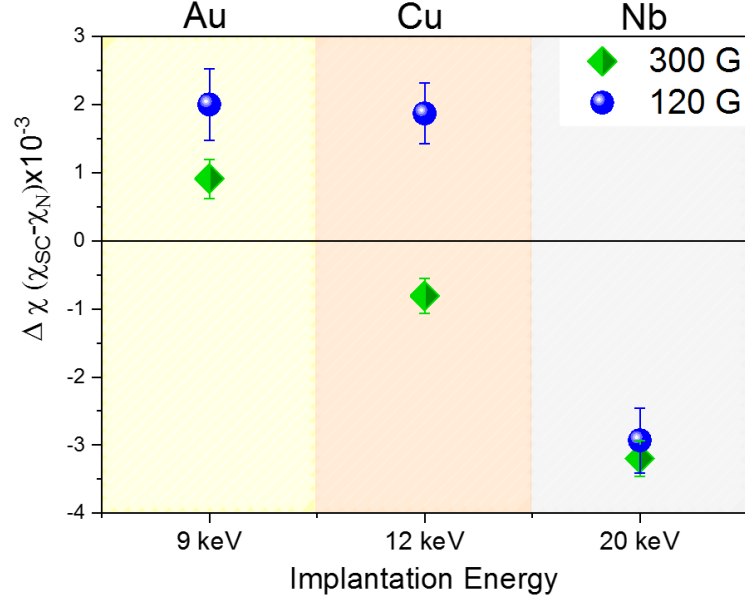


Figure 5.9: Change in local magnetic susceptibility ($\Delta\chi$) for a spin-active sample measured by LEM for 9, 12 and 20 keV implantation energies with fields of 120 G and 300 G applied. Inside the Nb at 20 keV the screening response is linear with field, yet the paramagnetic response in Au is non-linear whilst at 12 keV the screening shows a sign reversal at higher fields.

In order to explore the reproducibility of this effect, whilst characterising the field dependence, the local field was measured at both 2.7 K (SC state) and 10 K (N state) with 120 G transverse field. Fig. 5.9 summarises the obtained changes in susceptibility ($\Delta\chi$) found for 9, 12 and 20 keV implantation energies. The change in magnetic susceptibility has been calculated as $\Delta\chi = (B_{SC} - B_N)/B_N$. Immediately obvious is the linear dependence on applied field for the flux expulsion at 20 keV which from Eqn. 5.3, should be expected. Despite this, the susceptibility for the Au layer at 9 keV is non-linear with field. A larger χ is observed with the use of a lower field. This suggests that the $(n_s - n_t)$ component also has a non-linear dependence on field. At the intermediate energy of 12 keV, a small diamagnetic response is measured when 300 G is applied. At the lower field of 120 G, $\Delta\chi$ shows a complete sign reversal, most likely arising from the reduced influence of the Meissner response within the Nb layer. For 12 keV implantation energy, the signal is a superposition of the μ^+ precession possibly within all three layers and as such if the signal inside Au saturates at a field less than 300 G, then the conventional diamagnetic response at the boundary of

5.4 Anomalous screening effects measured by LE- μ SR

the Nb layer could act to suppress the average field for 12 keV and even change its sign.

The results presented here demonstrate a reproducible paramagnetic screening response that we attribute to the generation of odd-frequency spin-triplet states at the magnetic Cu/C₆₀ interface. The anomalous response of the sample flux profile in the superconducting state to both temperature and magnetic field provides a compelling case for unconventional screening effects in a hybrid metal/molecule superconducting system.[98–100]

CHAPTER 6

Conclusions and future work

For the sustainable growth of the ICT sector to continue, advancements in both room-temperature and superconducting spintronics might be required. Critically, the research into both fields should not just aim to improve upon existing device architectures but explore devices with new functionalities. Molecular spintronics is a promising field within which to develop new multifunctional devices due to the rich optical, electrical and magnetic phenomena that they can cooperatively exhibit. In particular, controlling the interfacial spin polarisation at metallo-molecular interfaces may lead to new classes of devices where the functionalised interfaces play an active role and are controlled via the molecules response to optical, electrical or chemical stimuli.[22]

In this thesis, we have utilised the spin-dependent interface phenomena present at C_{60} interfaces to explore new functionalities for both room-temperature and low-temperature applications. First, we have developed a novel room-temperature multifunctional spintronic device. Optical or electrical charging of an MnO_x/C_{60} interface leads to an equilibrium spin-polarisation that is controlled by the interface spin-dependent density of states and stabilised by the formation of a C_{60} -O dipole layer. The magnetic response to electrical and optical stimuli of these devices has been explored with XAS/XMCD/XLD and LE- μ SR. Room-temperature transport and photoluminescence spectroscopy methods have been used to elucidate upon the electrical properties of the devices and to characterise the chemical responsiveness of this system, as the electrical and optical properties of the device are manipulated through ionic migration. Second, we have shown that the emergent magnetic phenomena present at the interface between non-magnetic Cu and C_{60} can be incorporated into a superconducting proximity heterostructure in order to produce long-range triplet Cooper pair states, a key ingredient in the advancement of superconducting spintronics. Low-temperature transport was used to characterise the superconducting properties of thin film heterostructures and LE- μ SR was used to characterise screening effects throughout the sample, which provide information about the superconducting correlations present in the structure.

In Chapter 4, RT transport measurements confirmed that at the interface between C_{60} and MnO_x , O- C_{60} bonding creates an interfacial dipole layer that generates a rectifying barrier. The in-built potential formed at this interface and hence photovoltaic efficiency is determined by choice of metallo- C_{60} interface. When Co or Cu is used as the second electrode, the devices exhibit a photovoltaic effect. The insertion of an alumina tunnel barrier between the metal and C_{60} significantly reduces the efficiency of the photovoltaic interface such that the open-circuit voltage and photocurrent are negligible. This is most likely due to the charge transfer expected at the interfaces of Cu/C_{60} and Co/C_{60} .^[21; 63] The presence of the C_{60} -O dipole layer is supported by the DFT calculations performed by G. Teobaldi et al.^[149] and is similar to effects seen in LiF polar interfaces.^[155]

XAS was used to study the electronic structure of the C_{60} within these devices before and after the application of electrical stimuli. In the pre-existing study, conveyed in Fig. 4.1(a), upon the addition of electric charge to the MnO_x/C_{60} interface, a suppression in the LUMO derived orbital takes place, and a new spin-polarised orbital (LUMO*) emerges roughly 1 eV closer to E_F . In this thesis, we have systematically examined with XAS devices of varying constituent electrodes to show that the presence of the MnO_x/C_{60} interface is imperative to the emergence of the charged LUMO* orbital.

Most notably, we observe in devices that include the MnO_x/C_{60} interface but exclude the magnetic electrode, the emergence of a hybrid shoulder after a 200 mV bias has charged the interface. In this device, the shoulder once again appears roughly 1 eV below the LUMO. However, in this device the LUMO orbital does not show a similar suppression as is seen in the original experiment, nor does it display circular dichroism. The lack of these features could be due to the contribution from surface contaminants to the signal, or from C_{60} molecules that do not contribute to the effect being simultaneously probed due to restrictions of the beam focus. Astonishingly, the hybrid shoulder that emerges post bias shows a very strong (<100%) linear dichroism at RT. Due to the experiment geometry, we conclude that an electric dipole moment with an out of plane polarisation is the cause for the XLD signal. Critically, the XLD signal was seen to be very sensitive to an applied magnetic field as the application

of a ~ 500 mT field aligns the dipole moment to the magnetic field vector. Whether such an effect is due to the rotation of the molecules on the surface of the $\text{MnO}_x/\text{C}_{60}$ interface or redistribution of charge within the molecule itself is unknown. However, the effect certainly highlights the strong interfacial hybridisation, and coupling between spin and charge in this system. This observation supports that the distribution of charge on the surface of the $\text{MnO}_x/\text{C}_{60}$ interface is spin dependent. Also, it may explain why the shifts in the C_{60} orbital structure, in the original experiment shown in Fig. 4.1(b), are highly dependent upon the magnetisation of the Co electrode.

LE- μ SR corroborates the XAS/XMCD results. In two wide-area devices, signatures of changes to the internal field distributions are observed at the $\text{MnO}_x/\text{C}_{60}$ interface following electrical and optical stimulation. In the electrical charging experiment, increases of up to $26\pm 9\%$ (0.06 ± 0.02 MHz) are observed in the endohedral C_{60} muonium (Mu@C_{60}) frequency for C_{60} molecules that are in proximity to the $\text{MnO}_x/\text{C}_{60}$ interface after the application of a 200 mV electrical bias. Measurements in transverse field where we are no longer sensitive to the muonium signal show an increase in the μ^+ depolarisation rate of 0.08 ± 0.04 μs^{-1} in the same region of the sample. However, in this geometry, no increases in the static field were observed in the charged state. We enhance the experimental approach, by instead utilising the photovoltaic properties of the $\text{MnO}_x/\text{C}_{60}$ system to more homogeneously charge the interface with a photocurrent. In this optically stimulated geometry, we observed a more significant increase in the Mu@C_{60} frequency of $90\pm 10\%$ (0.8 ± 0.1 MHz), at the implantation energy that corresponds to the $\text{MnO}_x/\text{C}_{60}$ interface. Once more, no measurable changes occur to C_{60} molecules in the centre of the device. Critically, in transverse field, we observed an increased μ^+ precession frequency after charging the device with a photocurrent. This increased precession frequency corresponds to an increase in local field of 2.3 ± 0.6 G. We once more demonstrate that this increased local field does not occur far (10s of nm) away from the $\text{MnO}_x/\text{C}_{60}$ interface and that the original state can be reset through connecting the electrodes to a common ground. Therefore, in the optically excited μ SR study, we can confidently attribute the increased ZF muonium frequency to Zeeman splitting of the C_{60} hyperfine coupling, where the Zeeman field arises due to accumulated spin-polarised charge. In the wide-area photovoltaic device, we were able to generate the equilibrium spin-polarisation

several times before the device no-longer shows any changes. This device fatigue is a likely consequence of photo-assisted degradation of the C_{60} film.

By incorporating spin filtering, dipole formation and photovoltaic effects, we have engineered a system that can trap charge in a spin-dependent manner via electrical bias or light stimulation. We then proceeded to show that using electrical programming voltages (≥ 1.5 V) the properties of the MnO_x/C_{60} interfaces can be reversibly switched between an initial high resistance state where we have the spin filtering, interfacial dipole and photovoltaic properties to a low resistance state where the interfacial dipole is eliminated and the photovoltaic efficiency is suppressed. This was supported by photo-spectroscopy measurements where the photovoltaic efficiency is spatially mapped over the devices in each resistance state. Also, a higher photoluminescence yield is seen in the low resistance state due to the reduced separation of e-h pairs. Elemental analysis gathered through TEM-EDX supports our hypothesis of oxygen migration at this interface. Indeed, in other molecular devices, oxygen migration appears to play an essential role in the observed electrical and spin-dependent properties.[194; 195] In this thesis, we have not directly studied the effect of oxygen migration on the spin filtering properties of the interface. However, from the DFT calculations that describe the presented effect, it is likely that the measured changes in interfacial chemistry induced by the electro-migration of oxygen will yield another way to control these interfaces. The metal-oxide/molecule heterostructure presented in this thesis demonstrates a multifunctional memristor that could form the basis for the development of spin capacitors, spin-dependent photovoltaics and perhaps neuromorphic computing elements.[190; 228]

In Chapter 5 the low-temperature transport measurements of S/M/N proximity heterostructures confirmed that Cooper-pairs leak into C_{60} layers over the length scale of ~ 30 nm. For this to occur through the diffusion of Cooper pairs, the C_{60} must be very highly doped due to charge transfer from the metal surfaces. LE- μ SR was then used to characterise the interfacial magnetic state formed at a non-magnetic Cu/ C_{60} interface. By probing the Zeeman splitting of the $Mu@C_{60}$ hyperfine tensor, we observe a local dipolar field that decays away from the two Cu interfaces. After demagnetising the sample, this field disappears from the top interface and dramatically reduces on

the bottom interface. This suggests that the magnetic state of these interfaces are highly disordered as the domain size must be of a similar order to the C_{60} cage for the muonium signal to change so much in the demagnetised state.

After determining the coexistence of proximity-induced superconductivity and an inhomogenous spin-active interface in C_{60} based heterostructures, the screening effects in these systems were probed by low-temperature TF- μ SR. In the S/M/N system, which excludes the spin-active interface, we observe a small reduction in the local field within the normal metal due to screening currents generated by proximity induced correlations. A conventional Meissner signal is seen in the superconducting layer which is later simulated using geometrical parameters obtained through the in-depth structural characterisation and muon implantation simulations. For this sample, a model is derived using expected values of the penetration depth for thin film Nb that conclusively simulates the temperature dependence of the local field at the depth probed by the muons. For the S/M/ I_{SA} /M/N sample, which now includes the spin-active Cu/ C_{60} interface, the results do not follow such a conventional model. Instead, substantial suppression of the conventional Meissner screening in the superconducting film is observed where the onset of the diamagnetic signal does not begin until ~ 6 K. A paramagnetic signal is measured in the normal metal layer that we attribute to the existence of odd-frequency correlations generated at the spin-active interface. The observations here are similar to proposals made within several theoretical studies,[98; 99; 223] and past observations of such effects in metallic spin-triplet multi-layered systems.[100]

In the measurements taken at 12 keV, a paramagnetic screening signal was observed in the lower field (120 G) whereas, at the higher field (300 G) a conventional diamagnetic screening signal was recovered. This suggests that the depth-dependent field profile throughout the structure does not vary in a conventional manner with the applied magnetic field. In future work, the molecular spin-active system could be studied with greater depth and field dependence to evaluate the sign of the screening field and hence symmetry of the superconducting order parameter throughout the structure. This would confirm the hypothesis used that the formation of spin-triplets is

due to spin-rotation at the Cu/C₆₀ interface. A full parameter space study may be unavailable due to time-constraints intrinsic to muon spectroscopy measurements. A lab-based technique which seeks to detect anomalous screening effects in hybrid proximity stacks via offsets in Fraunhofer patterns produced in coupled Josephson junctions, as suggested by Mironov et al.[\[229\]](#), could perhaps be realised to provide a significantly quicker way to characterise these remarkable effects. Such characterisation would then aid in the advanced theoretical modelling of this system. Further understanding of the spin-triplet generation in hybrid molecular interfaces would be advantageous for the incorporation into super-spintronic memory and logic devices.

REFERENCES

- [1] A. Andrae and T. Edler, “On Global Electricity Usage of Communication Technology: Trends to 2030,” *Challenges*, vol. 6, no. 1, pp. 117–157, 2015.
- [2] N. Jones, “How to stop data centres from gobbling up the world’s electricity,” *Nature*, vol. 561, pp. 163–166, sep 2018.
- [3] Intergovernmental Panel on Climate Change, “GLOBAL WARMING OF 1.5 C,” tech. rep., 2018.
- [4] S. A. Wolf, D. D. Awschalom, R. A. Buhrman, J. M. Daughton, S. Von Molnár, M. L. Roukes, A. Y. Chtchelkanova, and D. M. Treger, “Spintronics: A spin-based electronics vision for the future,” *Science*, vol. 294, no. 5546, pp. 1488–1495, 2001.
- [5] I. Žutić, J. Fabian, and S. Das Sarma, “Spintronics Fundamentals and applications,” *Reviews of Modern Physics*, vol. 76, no. 2, pp. 323–410, 2004.
- [6] W. Chen, A. V. Rylyakov, V. Patel, J. E. Lukens, and K. K. Likharev, “Rapid single flux quantum t-flip flop operating up to 770 GHz,” *IEEE Transactions on Applied Superconductivity*, vol. 9, no. 2 PART 3, pp. 3212–3215, 1999.
- [7] D. S. Holmes, A. L. Ripple, and M. A. Manheimer, “Energy-Efficient Superconducting Computing—Power Budgets and Requirements,” *IEEE Transactions on Applied Superconductivity*, vol. 23, no. 3, pp. 1701610–1701610, 2013.
- [8] F. S. Bergeret, A. F. Volkov, and K. B. Efetov, “Long-range proximity effects in superconductor-ferromagnet structures,” *Physical Review Letters*, vol. 86, no. 18, pp. 4096–4099, 2001.

REFERENCES

- [9] A. Kadigrobov, R. I. Shekhter, and M. Jonson, “Quantum spin fluctuations as a source of long-range proximity effects in diffusive ferromagnet-superconductor structures,” *Europhysics Letters*, vol. 54, no. 3, pp. 394–400, 2001.
- [10] J. Linder and J. W. Robinson, “Superconducting spintronics,” *Nature Physics*, vol. 11, no. 4, pp. 307–315, 2015.
- [11] J. C. Lee and Z. Wen, “Pathways for greening the supply of rare earth elements in China,” *Nature Sustainability*, vol. 1, no. 10, pp. 598–605, 2018.
- [12] C. Banza Lubaba Nkulu, L. Casas, V. Haufroid, T. De Putter, N. D. Saenen, T. Kayembe-Kitenge, P. Musa Obadia, D. Kyanika Wa Mukoma, J. M. Lunda Ilunga, T. S. Nawrot, O. Luboya Numbi, E. Smolders, and B. Nemery, “Sustainability of artisanal mining of cobalt in DR Congo,” *Nature Sustainability*, vol. 1, no. 9, pp. 495–504, 2018.
- [13] J. S. Moodera, B. Koopmans, and P. M. Oppeneer, “On the path toward organic spintronics,” *MRS Bulletin*, vol. 39, no. 7, pp. 578–581, 2014.
- [14] Editorial, “Why going organic is good,” *Nature Materials*, vol. 8, no. 9, p. 691, 2009.
- [15] V. Dediu, M. Murgia, F. C. Matocotta, C. Taliani, and S. Barbanera, “Room temperature spin polarized injection in organic semiconductor,” *Solid State Communications*, vol. 122, no. 3-4, pp. 181–184, 2002.
- [16] A. Cornia and P. Seneor, “Spintronics: The molecular way,” *Nature Materials*, vol. 16, no. 5, pp. 505–506, 2017.
- [17] M. Sun and W. Mi, “Progress in organic molecular/ferromagnet spin interfaces: towards molecular spintronics,” *Journal of Materials Chemistry C*, vol. 6, no. 25, pp. 6619–6636, 2018.
- [18] C. Harris, R. Schlupp, and H. Schuch, “Optically detected electron spin locking and rotary echo trains in molecular excited states,” *Physical Review Letters*, pp. 0–3, 1973.

REFERENCES

- [19] F. Pulizzi, “A new face for organics,” *Nature Materials*, vol. 8, no. 9, pp. 696–697, 2009.
- [20] C. Barraud, P. Seneor, R. Mattana, S. Fusil, K. Bouzehouane, C. Deranlot, P. Graziosi, L. Hueso, I. Bergenti, V. Dediu, F. Petroff, and A. Fert, “Unravelling the role of the interface for spin injection into organic semiconductors,” *Nature Physics*, vol. 6, no. 8, pp. 615–620, 2010.
- [21] F. Al Ma’Mari, T. Moorsom, G. Teobaldi, W. Deacon, T. Prokscha, H. Luetkens, S. Lee, G. E. Sterbinsky, D. A. Arena, D. A. Maclaren, M. Flokstra, M. Ali, M. C. Wheeler, G. Burnell, B. J. Hickey, and O. Cespedes, “Beating the Stoner criterion using molecular interfaces,” *Nature*, vol. 524, no. 7563, pp. 69–74, 2015.
- [22] M. Cinchetti, V. A. Dediu, and L. E. Hueso, “Activating the molecular spinterface,” *Nature Materials*, vol. 16, no. 5, pp. 507–515, 2017.
- [23] Chemical Sciences and Society Summit, “Organic Electronics for a Better Tomorrow: Innovation, Accessibility, Sustainability,” *Royal Society of Chemistry*, no. September, p. 34, 2012.
- [24] S. Blundell, *Magnetism in condensed matter*, vol. 44. Oxford University Press, 2011.
- [25] E. C. Stoner, “Collective Electron Ferromagnetism,” *Proceedings of the Royal Society A: Mathematical, Physical and Engineering Sciences*, vol. 165, no. 922, pp. 372–414, 1938.
- [26] J. S. Miller, “Organic- and molecule-based magnets,” *Materials Today*, vol. 17, no. 5, pp. 224–235, 2014.
- [27] A. S. Edelstein and M. Mandel, “Antiferromagnetic to ferromagnetic transitions in organic free radicals,” *The Journal of Chemical Physics*, vol. 35, no. 3, pp. 1130–1131, 1961.
- [28] S. J. Blundell and F. L. Pratt, “Organic and molecular magnets,” *Journal of Physics Condensed Matter*, vol. 16, no. 24, p. 771, 2004.

REFERENCES

- [29] H. M. McConnell, "Ferromagnetism in Solid Free Radicals," *The Journal of Chemical Physics*, vol. 39, no. 7, pp. 1910–1910, 1963.
- [30] J. S. Miller, A. J. Epstein, and W. M. Reiff, "Ferromagnetic Molecular Charge-Transfer Complexes," *Chemical Reviews*, vol. 88, no. 1, pp. 201–220, 1988.
- [31] K. Itoh and M. Kinoshita, *Molecular Magnetism—New Magnetic Materials*, vol. 27. Cambridge University Press, 2002.
- [32] J. S. Miller, S. R. Chittipeddi, H. Rommelmann, S. R. Chittipeddi, J. H. Zhang, W. M. Reiff, and A. J. Epstein, "Ferromagnetic Behavior of $[\text{Fe}(\text{C}_5\text{Me}_5)_2] \cdot [\text{TCNE}]$. Structural And Magnetic Characterization of Decamethylferrocenium Tetracyanoethenide, $[\text{Fe}(\text{c}_5\text{Me}_5)_2] \cdot [\text{TCNE}] \cdot \text{MeCN}$, and Decamethylferrocenium Pentacyanopropenide, $[\text{Fe}(\text{C}_5\text{Me}_5)_2] \cdot [\text{C}_3(\text{CN})_5]$," *Journal of the American Chemical Society*, vol. 109, no. 3, pp. 769–781, 1987.
- [33] P.-M. ALLEMAND, K. C. KHEMANI, A. KOCH, F. WUDL, K. HOLCZER, S. DONOVAN, G. GRUNER, and J. D. THOMPSON, "Organic Molecular Soft Ferromagnetism in a Fullerene C₆₀," *Science*, vol. 253, no. 5017, pp. 301–302, 1991.
- [34] B. Narymbetov, A. Omerzu, V. V. Kabanov, M. Tokumoto, H. Kobayashi, and D. Mihailovic, "Origin of ferromagnetic exchange interactions in a fullerene-organic compound," *Nature*, vol. 407, no. 6806, pp. 883–885, 2000.
- [35] J. M. Manriquez, G. T. Yee, R. S. McLean, A. J. Epstein, and J. S. Miller, "A room-temperature molecular/organic-based magnet.," *Science (New York, N.Y.)*, vol. 252, no. 5011, pp. 1415–7, 1991.
- [36] N. Zhu, X. Zhang, I. H. Froning, M. E. Flatté, E. Johnston-Halperin, and H. X. Tang, "Low loss spin wave resonances in organic-based ferrimagnet vanadium tetracyanoethylene thin films," *Applied Physics Letters*, vol. 109, no. 8, p. 082402, 2016.
- [37] L. Bogani and W. Wernsdorfer, "Molecular spintronics using single-molecule magnets," *Nature Materials*, vol. 7, no. 3, pp. 179–186, 2008.

REFERENCES

- [38] F.-S. Guo, B. M. Day, Y.-C. Chen, M.-L. Tong, A. Mansikkamäki, and R. A. Layfield, “Magnetic hysteresis up to 80 kelvin in a dysprosium metallocene single-molecule magnet,” *Science*, vol. 0652, p. 10.1126/science.aav0652, 2018.
- [39] G. Szulczewski, S. Sanvito, and M. Coey, “A spin of their own,” *Nature Materials*, vol. 8, no. 9, pp. 693–695, 2009.
- [40] I. Appelbaum, B. Huang, and D. J. Monsma, “Electronic measurement and control of spin transport in silicon,” *Nature*, vol. 447, no. 7142, pp. 295–298, 2007.
- [41] V. I. Krinichnyi, S. D. Chemerisov, and Y. S. Lebedev, “EPR and charge-transport studies of polyaniline,” *Physical Review B*, vol. 55, no. 24, pp. 16233–16244, 1997.
- [42] K. Tsukagoshi, B. W. Alphenaar, and H. Ago, “Coherent transport of electron spin in a ferromagnetically contacted carbon nanotube,” *Nature*, vol. 401, no. 6753, pp. 572–574, 1999.
- [43] O. Céspedes, M. S. Ferreira, S. Sanvito, M. Kociak, and J. M. D. Coey, “Contact induced magnetism in carbon nanotubes,” *Journal of Physics Condensed Matter*, vol. 16, no. 10, pp. L155–L161, 2004.
- [44] M. Cinchetti, K. Heimer, J. P. Wüstenberg, O. Andreyev, M. Bauer, S. Lach, C. Ziegler, Y. Gao, and M. Aeschlimann, “Determination of spin injection and transport in a ferromagnet/organic semiconductor heterojunction by two-photon photoemission,” *Nature Materials*, vol. 8, no. 2, pp. 115–119, 2009.
- [45] A. J. Drew, J. Hoppler, L. Schulz, F. L. Pratt, P. Desai, P. Shakya, T. Kreouzis, W. P. Gillin, A. Suter, N. A. Morley, V. K. Malik, A. Dubroka, K. W. Kim, H. Bouyanfif, F. Bourqui, C. Bernhard, R. Scheuermann, G. J. Nieuwenhuys, T. Prokscha, and E. Morenzoni, “Direct measurement of the electronic spin diffusion length in a fully functional organic spin valve by low-energy muon spin rotation,” *Nature materials*, vol. 8, no. 2, pp. 109–114, 2009.

REFERENCES

- [46] M. S. Ferreira and S. Sanvito, “Contact-induced spin polarization in carbon nanotubes,” *Physical Review B - Condensed Matter and Materials Physics*, vol. 69, no. 3, 2004.
- [47] Z. H. Xiong, D. Wu, Z. V. Vardeny, and J. Shi, “Giant magnetoresistance in organic spin-valves.,” *Nature*, vol. 427, no. 6977, pp. 821–824, 2004.
- [48] M. Galbiati, S. Tatay, C. Barraud, A. V. Dediu, F. Petroff, R. Mattana, and P. Senneor, “Spinterface: Crafting spintronics at the molecular scale,” *MRS Bulletin*, vol. 39, no. July, pp. 602–607, 2014.
- [49] K. V. Raman, A. M. Kamerbeek, A. Mukherjee, N. Atodiresei, T. K. Sen, P. Lazić, V. Caciuc, R. Michel, D. Stalke, S. K. Mandal, S. Blügel, M. Müntenberg, and J. S. Moodera, “Interface-engineered templates for molecular spin memory devices,” *Nature*, vol. 493, no. 7433, pp. 509–513, 2013.
- [50] S. Sanvito, “Molecular spintronics: The rise of spinterface science,” *Nature Physics*, vol. 6, no. 8, pp. 562–564, 2010.
- [51] P. Amsalem, J. Niederhausen, A. Wilke, G. Heimel, R. Schlesinger, S. Winkler, A. Vollmer, J. P. Rabe, and N. Koch, “Role of charge transfer, dipole-dipole interactions, and electrostatics in Fermi-level pinning at a molecular heterojunction on a metal surface,” *Physical Review B - Condensed Matter and Materials Physics*, vol. 87, no. 3, 2013.
- [52] A. J. Maxwell, P. A. Brühwiler, D. Arvanitis, J. Hasselström, and N. Mårtensson, “C 1s ionisation potential and energy referencing for solid C60films on metal surfaces,” *Chemical Physics Letters*, vol. 260, no. 1-2, pp. 71–77, 1996.
- [53] T. R. Ohno, Y. Chen, S. E. Harvey, G. H. Kroll, J. H. Weaver, R. E. Haufler, and R. E. Smalley, “C60 bonding and energy-level alignment on metal and semiconductor surfaces,” *Physical Review B*, vol. 44, no. 24, pp. 13747–13755, 1991.
- [54] A. J. Maxwell, P. A. Briihwiler, A. Nilsson, N. Mkrtensson, and P. Rudolf, “Photoemission, autoionization, anti x-ray-absorption spectroscopy of ultrathin-film C60 on Au(110),” *Physical Review B*, vol. 49, no. 15, pp. 717–725, 1994.

REFERENCES

- [55] S. Braun, W. R. Salaneck, and M. Fahlman, “Energy-level alignment at organic/metal and organic/organic interfaces,” *Advanced Materials*, vol. 21, no. 14-15, pp. 1450–1472, 2009.
- [56] I. G. Hill, A. Rajagopal, A. Kahn, and Y. Hu, “Molecular level alignment at organic semiconductor-metal interfaces,” *Applied Physics Letters*, vol. 73, no. 5, pp. 662–664, 1998.
- [57] H. Fukagawa, S. Kera, T. Kataoka, S. Hosoumi, Y. Watanabe, K. Kudo, and N. Ueno, “The role of the ionization potential in vacuum-level alignment at organic semiconductor interfaces,” *Advanced Materials*, vol. 19, no. 5, pp. 665–668, 2007.
- [58] J. S. Moodera, T. S. Santos, and T. Nagahama, “The phenomena of spin-filter tunnelling,” *Journal of Physics: Condensed Matter*, vol. 19, no. 165202, 2007.
- [59] N. Atodiresei, J. Brede, P. Lazić, V. Caciuc, G. Hoffmann, R. Wiesendanger, and S. Blügel, “Design of the local spin polarization at the organic-ferromagnetic interface,” *Physical Review Letters*, vol. 105, no. 6, 2010.
- [60] S. Schmaus, A. Bagrets, Y. Nahas, T. K. Yamada, A. Bork, M. Bowen, E. Beaurepaire, F. Evers, and W. Wulfhchel, “Giant magnetoresistance through a single molecule,” *Nature Nanotechnology*, vol. 6, no. 3, pp. 185–189, 2011.
- [61] S. Steil, N. Großmann, M. Laux, A. Ruffing, D. Steil, M. Wiesenmayer, S. Mathias, O. L. A. Monti, M. Cinchetti, M. Aeschlimann, and N. Grossmann, “Spin-dependent trapping of electrons at spinterfaces,” *Nature Physics*, vol. 9, no. 4, pp. 242–247, 2013.
- [62] T. L. A. Tran, P. K. J. Wong, M. P. de Jong, W. G. van der Wiel, Y. Q. Zhan, and M. Fahlman, “Hybridization-induced oscillatory magnetic polarization of C60 orbitals at the C60/Fe(001) interface,” *Applied Physics Letters*, vol. 98, no. 22, p. 222505, 2011.
- [63] T. Moorsom, M. Wheeler, T. Mohd Khan, F. Al Ma’Mari, C. Kinane, S. Langridge, D. Ciudad, A. Bedoya-Pinto, L. Hueso, G. Teobaldi, V. K. Lazarov, D. Gilks, G. Burnell, B. J. Hickey, and O. Cespedes, “Spin-polarized electron

REFERENCES

- transfer in ferromagnet/C60 interfaces,” *Physical Review B*, vol. 90, no. 12, 2014.
- [64] K. Bairagi, A. Bellec, V. Repain, C. Chacon, Y. Girard, Y. Garreau, J. Lagoute, S. Rousset, R. Breitwieser, Y. C. Hu, Y. C. Chao, W. W. Pai, D. Li, A. Smogunov, and C. Barreteau, “Tuning the Magnetic Anisotropy at a Molecule-Metal Interface,” *Physical Review Letters*, vol. 114, no. 24, 2015.
- [65] F. Al Ma’Mari, M. Rogers, S. Alghamdi, T. Moorsom, S. Lee, T. Prokscha, H. Luetkens, M. Valvidares, G. Teobaldi, M. Flokstra, R. Stewart, P. Gargiani, M. Ali, G. Burnell, B. J. Hickey, and O. Cespedes, “Emergent magnetism at transition-metal-nanocarbon interfaces,” *Proceedings of the National Academy of Sciences of the United States of America*, vol. 114, no. 22, pp. 5583–5588, 2017.
- [66] Y. S. Dedkov, M. Sicot, and M. Fonin, “X-ray absorption and magnetic circular dichroism of graphene/Ni(111),” *Journal of Applied Physics*, vol. 107, no. 9, p. 1530, 2010.
- [67] T. L. A. Tran, T. Q. Le, J. G. Sanderink, W. G. Van Der Wiel, and M. P. De Jong, “The multistep tunneling analogue of conductivity mismatch in organic spin valves,” *Advanced Functional Materials*, vol. 22, no. 6, pp. 1180–1189, 2012.
- [68] M. Gobbi, F. Golmar, R. Llopis, F. Casanova, and L. E. Hueso, “Room-temperature spin transport in C 60-based spin valves,” *Advanced Materials*, vol. 23, no. 14, pp. 1609–1613, 2011.
- [69] T. D. Nguyen, F. Wang, X. G. Li, E. Ehrenfreund, and Z. V. Vardeny, “Spin diffusion in fullerene-based devices: Morphology effect,” *Physical Review B - Condensed Matter and Materials Physics*, vol. 87, no. 7, 2013.
- [70] S. Liang, R. Geng, B. Yang, W. Zhao, R. Chandra Subedi, X. Li, X. Han, and T. D. Nguyen, “Curvature-enhanced Spin-orbit Coupling and Spinterface Effect in Fullerene-based Spin Valves,” *Scientific Reports*, vol. 6, no. 1, p. 19461, 2016.

REFERENCES

- [71] D. Huertas-Hernando, F. Guinea, and A. Brataas, “Spin-orbit coupling in curved graphene, fullerenes, nanotubes, and nanotube caps,” *Physical Review B - Condensed Matter and Materials Physics*, vol. 74, no. 15, p. 155426, 2006.
- [72] D. Sun, K. J. van Schooten, M. Kavand, H. Malissa, C. Zhang, M. Groesbeck, C. Boehme, and Z. Vally Vardeny, “Inverse spin Hall effect from pulsed spin current in organic semiconductors with tunable spin-orbit coupling,” *Nature Materials*, vol. 20, no. April, pp. 1–8, 2016.
- [73] W. I. F. David, R. M. Ibberson, and T. J. S. Dennis, “Structural Phase Transitions in the Fullerene C₆₀ Related content Neutron scattering and SR studies of fullerenes and their derivatives K Prassides-Structural Phase Transitions in the Fullerene C₆₀,” *EPL*, vol. 18, p. 219, 1992.
- [74] P. A. Heiney, J. E. Fischer, A. R. McGhie, W. J. Romanow, A. M. Denenstein, J. P. McCauley, A. B. Smith, and D. E. Cox, “Orientational Ordering Transition in Solid C₆₀,” *Physical Review Letters*, vol. 66, no. 22, pp. 2911–2914, 1991.
- [75] M. S. Dresselhaus, G. Dresselhaus, and P. C. Eklund, *Science of Fullerenes and Carbon Nanotubes*. 1996.
- [76] G. Gensterblum, “Structural, vibrational and electronic properties of fullerene and epitaxial C₆₀(111) films grown on GeS (001): A review,” *Journal of Electron Spectroscopy and Related Phenomena*, vol. 81, no. 2, pp. 89–218, 1996.
- [77] H. Kamerlingh Onnes, “Further experiments with Liquid Helium. D. On the change of Electrical Resistance of Pure Metals at very low Temperatures, etc. V. The Disappearance of the resistance of mercury,” *Proceedings of the Koninklijke Akademie Van Wetenschappen te Amsterdam*, vol. 14, pp. 113–115, 1911.
- [78] F. London and H. London, “The electromagnetic equations of the superconductor,” *Proceedings of the Royal Society of London. Series A - Mathematical and Physical Sciences*, vol. 149, no. 866, pp. 71–88, 1935.
- [79] V. Ginzburg and L. Landau, “On the theory of superconductivity,” *Zh.Eksp.Teor.Fiz*, vol. 20, no. 1064, pp. 1064–1082, 1950.

REFERENCES

- [80] A. Y. Rusanov, M. Hesselberth, J. Aarts, and A. I. Buzdin, “Enhancement of the Superconducting Transition Temperature in Nb/Permalloy Bilayers by Controlling the Domain State of the Ferromagnet,” *Physical Review Letters*, vol. 93, no. 5, 2004.
- [81] M. G. Flokstra, S. J. Ray, S. J. Lister, J. Aarts, H. Luetkens, T. Prokscha, A. Suter, E. Morenzoni, and S. L. Lee, “Measurement of the spatial extent of inverse proximity in a Py/Nb/Py superconducting trilayer using low-energy muon-spin rotation,” *Physical Review B - Condensed Matter and Materials Physics*, vol. 89, no. 5, p. 54510, 2014.
- [82] J. Bardeen, L. N. Cooper, and J. R. Schrieffer, “Theory of Superconductivity,” *Physical Review*, vol. 108, no. 5, pp. 1175–1204, 1957.
- [83] J. F. Annett, *Superfluids and Condensates*. Oxford University Press, 2004.
- [84] A. P. Mackenzie and Y. Maeno, “The superconductivity of Sr₂ RuO₄ and the physics of spin-triplet pairing,” *Rev. Mod. Phys.*, vol. 75, no. 2, pp. 657–712, 2003.
- [85] K. D. Nelson, Z. Q. Mao, Y. Maeno, and Y. Liu, “Odd-parity superconductivity in Sr₂RuO₄,” *Science*, vol. 306, no. 5699, pp. 1151–1154, 2004.
- [86] M. Eschrig, “Spin-polarized supercurrents for spintronics,” *Physics Today*, vol. 64, no. 1, pp. 43–49, 2011.
- [87] P. G. De Gennes, “Boundary effects in superconductors,” *Reviews of Modern Physics*, vol. 36, no. 1, pp. 225–237, 1964.
- [88] A. I. Buzdin, “Proximity effect in superconductor-ferromagnet heterostructures,” *Rev. Mod. Phys.*, vol. 77, no. 3, pp. 935–976, 2005.
- [89] B. Pannetier and H. Courtois, “Andreev Reflection and Proximity effect,” *Journal of Low Temperature Physics*, vol. 118, no. 5/6, pp. 599–615, 1999.
- [90] P. Fulde and R. A. Ferrell, “Superconductivity in a strong spin-exchange field,” *Physical Review*, vol. 135, no. 3A, pp. A550–A563, 1964.

REFERENCES

- [91] A. I. Larkin and Y. N. Ovchinnikov, “Nonuniform state of superconductors,” *Sov.Phys.JETP*, vol. 20, no. 762, 1965.
- [92] M. Eschrig, J. Kopu, A. Konstandin, J. Cuevas, M. Fogelström, and G. Schön, “Singlet-Triplet Mixing in Superconductor-Ferromagnet Hybrid Devices,” in *Advances in Solid State Physics*, pp. 533–546, Springer, 2004.
- [93] D. Fritsch and J. F. Annett, “Triplet superconductivity and proximity effect induced by Bloch and Néel domain walls,” *Superconductor Science and Technology*, vol. 28, no. 8, p. 85015, 2015.
- [94] C. T. Wu, O. T. Valls, and K. Halterman, “Proximity effects in conical-ferromagnet/superconductor bilayers,” *Physical Review B - Condensed Matter and Materials Physics*, vol. 86, no. 18, p. 184517, 2012.
- [95] D. Fritsch and J. F. Annett, “Proximity effect in superconductor/conical magnet/ferromagnet heterostructures,” *New Journal of Physics*, vol. 16, no. 5, p. 055005, 2014.
- [96] T. Yokoyama and J. Linder, “Josephson effect through magnetic skyrmions,” *Physical Review B - Condensed Matter and Materials Physics*, vol. 92, no. 6, p. 060503, 2015.
- [97] M. S. Kalenkov, A. D. Zaikin, and V. T. Petrashov, “Triplet superconductivity in a ferromagnetic vortex,” *Physical Review Letters*, vol. 107, no. 8, 2011.
- [98] T. Yokoyama, Y. Tanaka, and N. Nagaosa, “Anomalous Meissner effect in a normal-metal-superconductor junction with a spin-active interface,” *Physical Review Letters*, vol. 106, no. 24, 2011.
- [99] M. Alidoust, K. Halterman, and J. Linder, “Meissner effect probing of odd-frequency triplet pairing in superconducting spin valves,” *Physical Review B - Condensed Matter and Materials Physics*, vol. 89, no. 5, p. 54508, 2014.
- [100] A. Di Bernardo, Z. Salman, X. L. Wang, M. Amado, M. Egilmez, M. G. Flokstra, A. Suter, S. L. Lee, J. H. Zhao, T. Prokscha, E. Morenzoni, M. G. Blamire, J. Linder, and J. W. Robinson, “Intrinsic paramagnetic meissner effect due to s-wave odd-frequency superconductivity,” *Physical Review X*, vol. 5, no. 4, 2015.

REFERENCES

- [101] M. G. Flokstra, R. Stewart, N. Satchell, G. Burnell, H. Luetkens, T. Prokscha, A. Suter, E. Morenzoni, S. Langridge, and S. L. Lee, "Observation of Anomalous Meissner Screening in Cu/Nb and Cu/Nb/Co Thin Films," *Physical Review Letters*, vol. 120, no. 24, 2018.
- [102] M. G. Flokstra, N. Satchell, J. Kim, G. Burnell, P. J. Curran, S. J. Bending, J. F. K. Cooper, C. J. Kinane, S. Langridge, A. Isidori, N. Pugach, M. Eschrig, H. Luetkens, A. Suter, T. Prokscha, and S. L. Lee, "Remotely induced magnetism in a normal metal using a superconducting spin-valve," *Nature Physics*, vol. 12, no. 1, pp. 57–61, 2015.
- [103] A. Suter, G. Logvenov, A. V. Boris, F. Baiutti, F. Wrobel, L. Howald, E. Stilp, Z. Salman, T. Prokscha, and B. Keimer, "Superconductivity drives magnetism in δ -doped La₂CuO₄," *Physical Review B*, vol. 97, no. 13, p. 134522, 2018.
- [104] P. J. Kelly and R. D. Arnell, "Magnetron sputtering: a review of recent developments and applications," *Vacuum*, vol. 56, no. 3, pp. 159–172, 2000.
- [105] K. Ellmer, "Magnetron sputtering of transparent conductive zinc oxide: relation between the sputtering parameters and the electronic properties," *Journal of Physics D - Applied Physics*, vol. 33, pp. R17–R32, 2000.
- [106] Y. H. Kim, I. H. Lee, K. J. Chang, and S. Lee, "Dynamics of Fullerene Coalescence," *Physical Review Letters*, vol. 90, no. 6, p. 4, 2003.
- [107] J. A. Nisha, V. Sridharan, J. Janaki, Y. Hariharan, V. S. Sastry, C. S. Sundar, and T. S. Radhakrishnan, "Studies of C₆₀ Oxidation and Products," pp. 4503–4506, 1996.
- [108] H. Werner, M. Wohlers, D. Bublak, J. Blöcker, and R. Schlögl, "Interaction of molecular oxygen with solid c₆₀," *Fullerene Science and Technology*, vol. 1, no. 4, pp. 457–474, 1993.
- [109] G. H. Kroll, P. J. Benning, Y. Chen, T. R. Ohno, J. H. Weaver, L. P. F. Chibante, and R. E. Smalley, "Interaction of O₂ with C₆₀: photon-induced oxidation," *Chemical Physics Letters*, vol. 181, no. 2-3, pp. 112–116, 1991.

REFERENCES

- [110] J. Als-Nielsen and D. McMorrow, *Elements of modern X-ray physics*. Wiley, 2011.
- [111] L. G. Parratt, “Surface studies of solids by total reflection of x-rays,” *Physical Review*, vol. 95, no. 2, pp. 359–369, 1954.
- [112] D. Windover, E. Barnat, J. Y. Kim, M. Nielsen, T. Lu, A. Kumar, and H. Bakhru, “Thin Film Density Determination By Multiple Radiation Energy Dispersive X-Ray Reflectivity,” *Advances in X-ray Analysis*, vol. 42, no. C, pp. 590–600, 2000.
- [113] H. Kiessig, “Interferenz von Rontgenstrahlen an dunnen Schichten,” *Annalen der Physik*, vol. 402, no. 7, pp. 769–788, 1931.
- [114] M. Björck and G. Andersson, “GenX: An extensible X-ray reflectivity refinement program utilizing differential evolution,” *Journal of Applied Crystallography*, vol. 40, no. 6, pp. 1174–1178, 2007.
- [115] Quantum Design, “Magnetic Property Measurement System: SQUID VSM User’s Manual,” 2009.
- [116] J. Clarke and A. I. Braginski, *The SQUID Handbook*, vol. 1. Wiley-VCH, 2004.
- [117] R. C. Jaklevic, J. Lambe, A. H. Silver, and J. E. Mercereau, “Quantum Interference Effects in Josephson Tunneling,” *Physical Review Letters*, vol. 12, no. 7, 1964.
- [118] V. Capozzi, G. Casamassima, G. Lorusso, A. Minafra, R. Piccolo, T. Trovato, and A. Valentini, “Optical spectra and photoluminescence of C60 thin films,” *Solid State Communications*, vol. 98, no. 9, pp. 853–858, 1996.
- [119] R. W. Lof, M. A. Van Veenendaal, B. Koopmans, H. T. Jonkman, and G. A. Sawatzky, “Band Gap, Excitons, and Coulomb Interaction in Solid C60,” *Physical Review Letters*, vol. 68, p. 26, 1992.
- [120] Z. Luo, X. Cheng, Y. Luo, B. H. Loo, A. Peng, and J. Yao, “Photoassisted magnetization of fullerene C60 with magnetic-field trapped Raman scattering,” *Journal of the American Chemical Society*, vol. 134, no. 2, pp. 1130–5, 2012.

REFERENCES

- [121] C. Chancey and M. O'Brien, *The Jahn-Teller Effect in C60 and Other Icosahedral Complexes*. 1997.
- [122] G. van der Laan and A. I. Figueroa, "X-ray magnetic circular dichroism -A versatile tool to study magnetism," *Coordination Chemistry Reviews*, vol. 277, pp. 95–129, 2014.
- [123] C. R. McNeill and H. Ade, "Soft X-ray characterisation of organic semiconductor films," *J. Mater. Chem. C*, vol. 1, no. 2, pp. 187–201, 2013.
- [124] S. J. Blundell, "Spin-polarized muons in condensed matter physics," *Contemporary Physics*, vol. 40, no. 3, pp. 175–192, 1999.
- [125] S. J. Blundell, "Muon-spin rotation studies of electronic properties of molecular conductors and superconductors," *Chemical Reviews*, vol. 104, no. 11, pp. 5717–5735, 2004.
- [126] S. F. J. Cox, "Implanted muon studies in condensed matter science," *Journal of Physics C: Solid State Physics*, vol. 20, no. 22, pp. 3187–3319, 1987.
- [127] P. Bakule and E. Morenzoni, "Generation and applications of slow polarized muons," *Contemporary Physics*, vol. 45, no. 3, pp. 203–225, 2004.
- [128] S. L. Lee, R. Cywinski, and S. H. Kilcoyne, *Muon Science : Muons in Physics, Chemistry and Materials*. CRC Press, 1999.
- [129] T. Prokscha, E. Morenzoni, C. David, A. Hofer, H. Glückler, and L. Scandella, "Moderator gratings for the generation of epithermal positive muons," *Applied Surface Science*, vol. 172, no. 3-4, pp. 235–244, 2001.
- [130] A. Suter and B. M. Wojek, "Musrfit: A Free Platform-Independent Framework for μ sR Data Analysis," in *Physics Procedia*, vol. 30, pp. 69–73, 2012.
- [131] R. M. Macrae, K. Prassides, I. M. Thomas, E. Roduner, C. Niedermayer, U. Binninger, C. Bernhard, A. Hofer, and I. D. Reid, "Reorientational Dynamics of Solid C-70 Probed By Positive Muons," *Journal of Physical Chemistry*, vol. 98, no. 47, pp. 12133–12141, 1994.

REFERENCES

- [132] B. D. Patterson, “Muonium states in semiconductors,” *Reviews of Modern Physics*, vol. 60, no. 1, pp. 69–159, 1988.
- [133] T. L. Duty, J. H. Brewer, K. Chow, R. F. Kiefl, A. W. Macfarlane, G. D. Morris, J. W. Schneider, B. Hitti, R. Lichti, L. Brard, J. E. Fischer, A. B. Smith Iii, and R. M. Strongin, “ZERO-FIELD muSR IN CRYSTALLINE C60,” *Hyperfine Interactions*, vol. 86, pp. 789–795, 1994.
- [134] R. F. Kiefl, J. W. Schneider, A. Macfarlane, K. Chow, T. L. Duty, T. L. Estle, B. Hitti, R. L. Lichti, E. J. Ansaldo, C. Schwab, P. W. Percival, G. Wei, S. Wlodek, K. Kojima, W. J. Romanow, J. P. Mccauley, N. Coustel, J. E. Fischer, and A. B. Smith, “Molecular Dynamics of MuC60 Radical in Solid C60,” *Physical Review Letters*, vol. 68, no. 9, pp. 1347–1350, 1992.
- [135] R. F. Kiefl, J. W. Schneider, A. Macfarlane, K. Chow, T. L. Duty, T. L. Estle, B. Hitti, R. L. Lichti, E. J. Ansaldo, C. Schwab, P. W. Percival, G. Wei, S. Wlodek, K. Kojima, W. J. Romanow, J. P. Mccauley, N. Coustel, J. E. Fischer, A. B. Smith, R. F. Kiefl’, and T. L. Duty’, “Molecular Dynamics of the Muonium-C60 Radical in Solid C60,” *Physical Review Letters*, vol. 68, no. 17, pp. 2708–2711, 1992.
- [136] A. J. Ansaldo, C. Neidermayer, and C. E. Stronach, “Muonium in fullerite,” *Nature*, vol. 353, p. 121, 1991.
- [137] U. Binniger, C. Bernhard, A. Hofer, C. Niedermayer, E. Recknagel, J. Erxmeyer, and A. Weidinger, “Rotational dynamics of solid C70 investigated by the muon-spin-rotation technique,” *Physical Review B*, vol. 51, no. 21, pp. 14867–14873, 1995.
- [138] K. Prassides, T. J. S. Dennis, C. Christides, E. Roduner, H. W. Kroto, R. Taylor, and D. R. M. Walton, “Mu@C70: Monitoring the Dynamics of Fullerenes from Inside the Cage,” *The Journal of Physical Chemistry*, vol. 96, no. 26, pp. 10600–10602, 1992.
- [139] I. Mckenzie and S. P. Cottrell, “Microscopic muon dynamics in the polymer electrolyte poly(ethylene oxide),” *Physical Review E*, vol. 96, 2017.

REFERENCES

- [140] E. Abou-Hamad, Y. Kim, T. Wågberg, D. Boesch, S. Aloni, A. Zettl, A. Rubio, D. E. Luzzi, and C. Goze-Bac, “Molecular dynamics and phase transition in one-dimensional crystal of C 60 encapsulated inside single wall carbon nanotubes,” *ACS Nano*, vol. 3, no. 12, pp. 3878–3883, 2009.
- [141] A. Pivrikas, M. Ullah, T. B. Singh, C. Simbrunner, G. Matt, H. Sitter, and N. S. Sariciftci, “Meyer-Neldel rule for charge carrier transport in fullerene devices: A comparative study,” *Organic Electronics: physics, materials, applications*, vol. 12, no. 1, pp. 161–168, 2011.
- [142] A. Pivrikas, M. Ullah, H. Sitter, and N. S. Sariciftci, “Electric field dependent activation energy of electron transport in fullerene diodes and field effect transistors: Gill’s law,” *Applied Physics Letters*, vol. 98, no. 9, p. 092114, 2011.
- [143] M. Ullah, A. Pivrikas, I. I. Fishchuk, A. Kadashchuk, P. Stadler, C. Simbrunner, N. S. Sariciftci, and H. Sitter, “Electric field and grain size dependence of Meyer-Neldel energy in C60 films,” *Synthetic Metals*, vol. 161, no. 17-18, pp. 1987–1990, 2011.
- [144] S. Sanvito, “Molecular spintronics,” *Chemical Society Reviews*, vol. 40, no. 6, p. 3336, 2011.
- [145] C. A. Goodwin, F. Ortu, D. Reta, N. F. Chilton, and D. P. Mills, “Molecular magnetic hysteresis at 60 kelvin in dysprosocenium,” *Nature*, vol. 548, no. 7668, pp. 439–442, 2017.
- [146] F. Djeghloul, M. Gruber, E. Urbain, D. Xenioti, L. Joly, S. Boukari, J. Arab-ski, H. Bulou, F. Scheurer, F. Bertran, P. Le Fèvre, A. Taleb-Ibrahimi, W. Wulfhekel, G. Garreau, S. Hajjar-Garreau, P. Wetzel, M. Alouani, E. Beau-repaire, M. Bowen, and W. Weber, “High Spin Polarization at Ferromagnetic Metal-Organic Interfaces: A Generic Property,” *Journal of Physical Chemistry Letters*, vol. 7, no. 13, pp. 2310–2315, 2016.
- [147] S. Delprat, M. Galbiati, S. Tatay, B. Quinard, C. Barraud, F. Petroff, P. Seneor, and R. Mattana, “Molecular spintronics: the role of spin-dependent hybridiza-tion,” *Journal of Physics D: Applied Physics*, vol. 51, no. 47, p. 473001, 2018.

REFERENCES

- [148] V. A. Dediu, L. E. Hueso, I. Bergenti, and C. Taliani, “Spin routes in organic semiconductors,” *Nature Materials*, vol. 8, no. 9, pp. 707–716, 2009.
- [149] T. Moorsom, M. Rogers, I. Scivetti, S. Bandaru, G. Teobaldi, M. Valvidares, M. Flokstra, S. Lee, R. Stewart, T. Prokscha, P. Gargiani, G. Stefanou, M. Ali, F. Al Ma’Mari, G. Burnell, B. J. Hickey, and O. Cespedes, “Reversible spin storage in organic-metal-oxide heterojunctions,” *Under review*, pp. 1–17, 2018.
- [150] T. Moorsom, *Electron transfer and spin injection in C60 -ferromagnetic composites*. PhD thesis, 2016.
- [151] V. P. Malinenko, L. A. Aleshina, A. L. Pergament, and G. V. Germak, “Switching Effects and MetalInsulator Transition in Manganese Oxide,” *Journal on Selected Topics in Nano Electronics and Computing*, vol. 1, no. 1, pp. 44–50, 2014.
- [152] a. L. Pergament, V. P. Malinenko, L. a. Aleshina, and V. V. Kolchigin, “Metal-insulator phase transition and electrical switching in manganese dioxide,” *Physics of the Solid State*, vol. 54, no. 12, pp. 2486–2490, 2012.
- [153] G. Schmidt, D. Ferrand, L. Molenkamp, A. Filip, and B. van Wees, “Fundamental obstacle for electrical spin injection from a ferromagnetic metal into a diffusive semiconductor,” *Physical Review B - Condensed Matter and Materials Physics*, vol. 62, no. 8, pp. R4790–R4793, 2000.
- [154] W. Chen, D. Qi, X. Gao, and A. T. S. Wee, “Surface transfer doping of semiconductors,” 2009.
- [155] M. A. Baldo and S. R. Forrest, “Interface-limited injection in amorphous organic semiconductors,” *Physical Review B - Condensed Matter and Materials Physics*, vol. 64, no. 8, 2001.
- [156] L. Schulz, L. Nuccio, M. Willis, P. Desai, P. Shakya, T. Kreouzis, V. K. Malik, C. Bernhard, F. L. Pratt, N. A. Morley, A. Suter, G. J. Nieuwenhuys, T. Prokscha, E. Morenzoni, W. P. Gillin, and A. J. Drew, “Engineering spin propagation across a hybrid organic/inorganic interface using a polar layer,” *Nature Materials*, vol. 10, no. 1, pp. 39–44, 2011.

REFERENCES

- [157] R. C. Haddon, A. S. Perel, R. C. Morris, T. T. M. Palstra, A. F. Hebard, and R. M. Fleming, "C60 thin film transistors," *Applied Physics Letters*, vol. 67, no. 1, pp. 121–123, 1995.
- [158] S. Kazaoui and N. Minami, "Intermolecular charge transfer excitons in C70 as compared with C60 films," *Synthetic Metals*, vol. 86, pp. 2345–2346, 1997.
- [159] T. Ashley, C. Elliott, N. Gordon, T. Phillips, and R. Hall, "Applications of negative luminescence," *Infrared Physics & Technology*, vol. 38, no. 3, pp. 145–151, 1997.
- [160] P. E. Burrows and S. R. Forrest, "Electroluminescence from trap-limited current transport in vacuum deposited organic light emitting devices," *Applied Physics Letters*, vol. 64, no. 17, pp. 2285–2287, 1994.
- [161] T. Moorsom, M. Wheeler, M. Taukeer Khan, F. Al Ma'Mari, G. Burnell, B. J. Hickey, V. Lazarov, D. Gilks, and O. Cespedes, "Effects of spin doping and spin injection in the luminescence and vibrational spectrum of C60," *Applied Physics Letters*, vol. 105, no. 2, p. 022408, 2014.
- [162] J. L. Sauvajol, Z. Hricha, N. Coustel, Z. Zahab, and R. Aznar, "Photoluminescence of solid C60," *Journal of Physics: Condensed Matter*, vol. 5, no. 13, pp. 2045–2054, 1993.
- [163] V. Capozzi, T. Trovato, H. Berger, and G. F. Lorusso, "Photoluminescence spectra of C60 thin films deposited on different substrates," *Carbon*, vol. 35, no. 6, pp. 763–766, 1997.
- [164] G. Tian and Y. Luo, "Fluorescence and Phosphorescence of Single C 60 Molecules as Stimulated by a Scanning Tunneling Microscope," *Angewandte Chemie*, vol. 125, no. 18, pp. 4914–4917, 2013.
- [165] N. Asli, M. I. Vexler, A. F. Shulekin, and P. Seegebrecht, "Hot-electron-induced luminescence of metal – oxide-semiconductor tunnel devices," *Semicond. Sci. Technol. Semicond. Sci. Technol*, vol. 147, no. 1803, pp. 147–153, 2003.

REFERENCES

- [166] Z. C. Dong, X. L. Guo, A. S. Trifonov, P. S. Dorozhkin, K. Miki, K. Kimura, S. Yokoyama, and S. Mashiko, "Vibrationally Resolved Fluorescence from Organic Molecules near Metal Surfaces in a Scanning Tunneling Microscope," *Physical Review Letters*, vol. 92, no. 8, p. 086801, 2004.
- [167] C. Jansing, H. C. Mertins, A. Gaupp, A. Sokolov, M. C. Gilbert, H. Wahab, and H. Timmers, "X-ray natural linear dichroism of graphitic materials across the carbon K-edge: Correction for perturbing high-order harmonics," in *Journal of Physics: Conference Series*, vol. 712, 2016.
- [168] J. Stöhr and M. G. Samant, "Liquid crystal alignment by rubbed polymer surfaces: a microscopic bond orientation model," *Journal of Electron Spectroscopy and Related Phenomena*, vol. 98, no. 99, pp. 189–207, 1999.
- [169] J. Stöhr, H. A. Padmore, S. Anders, T. Stammler, and M. R. Scheinfein, "Principles of X-ray Magnetic Dichroism Spectromicroscopy," *Surface Review and Letters*, vol. 5, no. 6, pp. 1–12, 1998.
- [170] G. van der Laan, "Magnetic linear x-ray dichroism as a probe of the magnetocrystalline anisotropy," *Physical Review Letters*, vol. 82, no. 3, pp. 640–643, 1999.
- [171] A. Bedoya-Pinto, S. G. Miralles, S. Vélez, A. Atxabal, P. Gargiani, M. Valvidares, F. Casanova, E. Coronado, and L. E. Hueso, "Interface-Assisted Sign Inversion of Magnetoresistance in Spin Valves Based on Novel Lanthanide Quinoline Molecules," *Advanced Functional Materials*, vol. 28, no. 16, p. 1702099, 2018.
- [172] M. Takahashi and J. I. Igarashi, "X-ray magnetic circular dichroism at the K edge of Mn₃GaC," *Physical Review B - Condensed Matter and Materials Physics*, vol. 67, no. 24, 2003.
- [173] E. Morenzoni, E. M. Forgan, H. Glückler, T. J. Jackson, H. Luetkens, C. Niedermayer, T. Prokscha, T. M. Riseman, M. Birke, A. Hofer, J. Litterst, M. Pleines, and G. Schatz, "Muon spin rotation and relaxation experiments on thin films," *Hyperfine Interactions*, vol. 133, no. 1-4, pp. 179–195, 2001.

REFERENCES

- [174] R. J. Van De Veerdonk, J. Nowak, R. Meservey, J. S. Moodera, and W. J. De Jonge, “Current distribution effects in magnetoresistive tunnel junctions,” *Applied Physics Letters*, vol. 71, no. 19, pp. 2839–2841, 1997.
- [175] C. Niedermayer, “Fullerenes with μ SR,” *Hyperfine Interactions*, vol. 97-98, no. 1, pp. 285–304, 1996.
- [176] P. W. Percival, B. Addison-Jones, J. C. Brodovitch, and S. Sun-Mack, “Radio-frequency muon spin resonance studies of endohedral and exohedral muonium adducts of fullerenes,” *Applied Magnetic Resonance*, vol. 11, no. 2, pp. 315–323, 1996.
- [177] D. V. Konarev, A. V. Kuzmin, S. V. Simonov, E. I. Yudanov, S. S. Khasanov, G. Saito, and R. N. Lyubovskaya, “Experimental observation of C60 LUMO splitting in the C60²⁻ dianions due to the Jahn–Teller effect. Comparison with the C60 radical anions,” *Physical Chemistry Chemical Physics*, vol. 15, no. 23, p. 9136, 2013.
- [178] V. Filidou and S. Mamone, “Probing the C60 triplet state coupling to nuclear spins inside and out,” *Philosophical Transactions of the Royal Society A: Mathematical, Physical and Engineering Sciences*, vol. 371, no. 1998, pp. 20120475–20120475, 2013.
- [179] M. Kállay, K. Németh, and P. R. Surján, “Triplet state characteristics of higher fullerenes,” *Journal of Physical Chemistry A*, vol. 102, no. 8, pp. 1261–1273, 1998.
- [180] G. M. Luke, Y. Fudamoto, K. M. Kojima, M. I. Larkin, J. Merrin, B. Nachumi, Y. J. Uemura, Y. Maeno, Z. Q. Mao, Y. Mori, H. Nakamura, and M. Sgrist, “Time-reversal symmetry-breaking superconductivity in Sr₂RuO₄,” *Nature*, vol. 394, no. 6693, pp. 558–561, 1998.
- [181] A. Lappas, K. Prassides, K. Vavakis, D. Arcon, R. Blinc, P. Cevc, A. Amato, R. Feyerherm, F. N. Gygax, and A. Schenck, “Spontaneous Magnetic Ordering in the Fullerene Charge-Transfer Salt (TDAE)C₆₀,” *Science (New York, N.Y.)*, vol. 267, no. 5205, pp. 1799–1802, 1995.

REFERENCES

- [182] I. Riedel, J. Parisi, V. Dyakonov, L. Lutsen, D. Vanderzande, and J. C. Hummelen, “Effect of temperature and illumination on the electrical characteristics of polymer-fullerene bulk-heterojunction solar cells,” *Advanced Functional Materials*, vol. 14, no. 1, pp. 38–44, 2004.
- [183] A. D. Platt, M. J. Kendrick, M. Loth, J. E. Anthony, and O. Ostroverkhova, “Temperature dependence of exciton and charge carrier dynamics in organic thin films,” *Physical Review B*, vol. 84, no. 23, p. 235209, 2011.
- [184] E. A. Katz, D. Faiman, S. M. Tuladhar, J. M. Kroon, M. M. Wienk, T. Fromherz, F. Padinger, C. J. Brabec, and N. S. Sariciftci, “Temperature dependence for the photovoltaic device parameters of polymer-fullerene solar cells under operating conditions,” *Journal of Applied Physics*, vol. 90, no. 10, pp. 5343–5350, 2001.
- [185] A. Nitzan, “A Relationship between Electron-Transfer Rates and Molecular Conduction,” *The Journal of Physical Chemistry A*, vol. 105, no. 12, pp. 2677–2679, 2001.
- [186] V. Mujica, M. Kemp, and M. A. Ratner, “Electron conduction in molecular wires. I. A scattering formalism,” *The Journal of Chemical Physics*, vol. 101, no. 8, pp. 6849–6855, 1994.
- [187] M. K. Yang, J. W. Park, T. K. Ko, and J. K. Lee, “Bipolar resistive switching behavior in Ti/ MnO₂/Pt structure for nonvolatile memory devices,” *Applied Physics Letters*, vol. 95, no. 4, p. 42105, 2009.
- [188] D. B. Strukov, G. S. Snider, D. R. Stewart, and R. S. Williams, “The missing memristor found,” *Nature*, vol. 453, no. 7191, pp. 80–83, 2008.
- [189] B. Mohammad, M. A. Jaoude, V. Kumar, D. M. Al Homouz, H. A. Nahla, M. Al-Qutayri, and N. Christoforou, “State of the art of metal oxide memristor devices,” *Nanotechnology Reviews*, vol. 5, no. 3, pp. 311–329, 2016.
- [190] G. Indiveri, B. Linares-Barranco, R. Legenstein, G. Deligeorgis, and T. Prodromakis, “Integration of nanoscale memristor synapses in neuromorphic computing architectures,” *Nanotechnology*, vol. 24, no. 38, p. 13, 2013.

REFERENCES

- [191] W. Yuhang, W. Lingyuan, L. Guodong, and L. Lixin, “Non-destructive photo-voltaic reading of interface type memristors using graphene as transparent electrode,” *Journal of Alloys and Compounds*, vol. 740, pp. 273–277, 2018.
- [192] M. Grünewald, N. Homonnay, J. Kleinlein, and G. Schmidt, “Voltage-controlled oxide barriers in organic/hybrid spin valves based on tunneling anisotropic magnetoresistance,” *Physical Review B - Condensed Matter and Materials Physics*, vol. 90, no. 20, p. 205208, 2014.
- [193] L. E. Hueso, I. Bergenti, A. Riminucci, Y. Zhan, and V. Dediu, “Multipurpose magnetic organic hybrid devices,” *Advanced Materials*, vol. 19, no. 18, pp. 2639–2642, 2007.
- [194] I. Bergenti, F. Borgatti, M. Calbucci, A. Riminucci, R. Cecchini, P. Graziosi, D. A. MacLaren, A. Giglia, J. P. Rueff, D. Céolin, L. Pasquali, and V. Dediu, “Oxygen Impurities Link Bistability and Magnetoresistance in Organic Spin Valves,” *ACS Applied Materials and Interfaces*, vol. 10, no. 9, pp. 8132–8140, 2018.
- [195] M. Prezioso, A. Riminucci, I. Bergenti, P. Graziosi, D. Brunel, and V. A. Dediu, “Electrically programmable magnetoresistance in multifunctional organic-based spin valve devices,” *Advanced Materials*, vol. 23, no. 11, pp. 1371–1375, 2011.
- [196] A. Hoffmann and S. D. Bader, “Opportunities at the Frontiers of Spintronics,” *Physical Review Applied*, vol. 4, no. 4, p. 047001, 2015.
- [197] M. Eschrig, J. Kopu, J. C. Cuevas, and G. Schön, “Theory of Half-Metal/Superconductor Heterostructures,” *Physical Review Letters*, vol. 90, no. 13, p. 4, 2003.
- [198] E. Coronado, C. Martí-Gastaldo, E. Navarro-Moratalla, A. Ribera, S. J. Blundell, and P. J. Baker, “Coexistence of superconductivity and magnetism by chemical design,” *Nature Chemistry*, vol. 2, no. 12, pp. 1031–1036, 2010.

REFERENCES

- [199] J. Clarke, “the Proximity Effect Between Superconducting and Normal Thin Films in Zero Field,” *Le Journal de Physique Colloques*, vol. 29, no. C2, pp. C2–3–C2–16, 1968.
- [200] S. Bommel, N. Kleppmann, C. Weber, H. Spranger, P. Schäfer, J. Novak, S. V. Roth, F. Schreiber, S. H. Klapp, and S. Kowarik, “Unravelling the multilayer growth of the fullerene C 60 in real time,” *Nature Communications*, vol. 5, no. 1, p. 5388, 2014.
- [201] C. B. Winkelmann, N. Roch, W. Wernsdorfer, V. Bouchiat, and F. Balestro, “Superconductivity in a single-C60 transistor,” *Nature Physics*, vol. 5, no. 12, pp. 876–879, 2009.
- [202] J. Niederhausen, P. Amsalem, A. Wilke, R. Schlesinger, S. Winkler, A. Vollmer, J. P. Rabe, and N. Koch, “Doping of C60 (sub)monolayers by Fermi-level pinning induced electron transfer,” *Physical Review B - Condensed Matter and Materials Physics*, vol. 86, no. 8, pp. 1–5, 2012.
- [203] A. J. Maxwell, P. A. Brühwiler, A. Nilsson, N. Mårtensson, and P. Rudolf, “Photoemission, autoionization, and x-ray-absorption spectroscopy of ultrathin-film C60 on Au(110),” *Physical Review B*, vol. 49, no. 15, pp. 10717–10725, 1994.
- [204] J. G. Hou, L. Lu, V. H. Crespi, X.-D. Xiang, A. Zettl, and M. L. Cohen, “Resistivity saturation in alkali-doped C60,” Tech. Rep. 12, 1995.
- [205] A. F. Hebard, T. T. M. Palstra, R. C. Haddon, and R. M. Fleming, “Absence of saturation in the normal-state resistivity of thin films of K3C60 and Rb3C60,” *Physical Review B*, vol. 48, no. 13, pp. 9945–9948, 1993.
- [206] O. Gunnarsson and J. E. Han, “The mean free path for electron conduction in metallic fullerenes,” *Nature*, vol. 405, no. 6790, pp. 1027–1030, 2000.
- [207] F. A. S. Al Ma’Mari, *Emergent Spin Ordering at C60 interfaces*. PhD thesis, 2016.

REFERENCES

- [208] J. A. Larsson, S. D. Elliott, J. C. Greer, J. Repp, G. Meyer, and R. Al-lenspach, "Orientation of individual C60 molecules adsorbed on Cu(111): Low-temperature scanning tunneling microscopy and density functional calculations," *Physical Review B - Condensed Matter and Materials Physics*, vol. 77, no. 11, p. 115434, 2008.
- [209] W. W. Pai, H. T. Jeng, C. M. Cheng, C. H. Lin, X. Xiao, A. Zhao, X. Zhang, G. Xu, X. Q. Shi, M. A. Van Hove, C. S. Hsue, and K. D. Tsuei, "Optimal electron doping of a C60 monolayer on Cu(111) via interface reconstruction," *Physical Review Letters*, vol. 104, no. 3, 2010.
- [210] G. Xu, X. Q. Shi, R. Q. Zhang, W. W. Pai, H. T. Jeng, and M. A. Van Hove, "Detailed low-energy electron diffraction analysis of the (44) surface structure of C60 on Cu(111): Seven-atom-vacancy reconstruction," *Physical Review B - Condensed Matter and Materials Physics*, vol. 86, no. 7, 2012.
- [211] L. Martín-Olivera, D. G. Shchukin, and G. Teobaldi, "Role of Metal Lattice Expansion and Molecular π -Conjugation for the Magnetic Hardening at Cu-Organics Interfaces," *Journal of Physical Chemistry C*, vol. 121, no. 42, pp. 23777–23787, 2017.
- [212] J. Linder, T. Yokoyama, A. Sudbø, and M. Eschrig, "Pairing symmetry conversion by spin-active interfaces in magnetic normal-metal-superconductor junctions," *Physical Review Letters*, vol. 102, no. 10, 2009.
- [213] J. Linder, A. Sudbø, T. Yokoyama, R. Grein, and M. Eschrig, "Signature of odd-frequency pairing correlations induced by a magnetic interface," *Physical Review B - Condensed Matter and Materials Physics*, vol. 81, no. 21, 2010.
- [214] N. J. Stone, "Table of nuclear magnetic dipole and electric quadrupole moments," *Atomic Data and Nuclear Data Tables*, vol. 90, no. 1, pp. 75–176, 2005.
- [215] E. Morenzoni, H. Glückler, T. Prokscha, R. Khasanov, H. Luetkens, M. Birke, E. M. Forgan, C. Niedermayer, and M. Pleines, "Implantation studies of keV positive muons in thin metallic layers," *Nuclear Instruments and Methods in Physics Research, Section B: Beam Interactions with Materials and Atoms*, vol. 192, no. 3, pp. 254–266, 2002.

REFERENCES

- [216] M. Tinkham, *Introduction to superconductivity*. Dover Publications, 2004.
- [217] M. Schöck, C. Sürgers, and H. V. Löhneysen, “Superconducting and magnetic properties of Nb/Pd_{1-x}Fex/Nb triple layers,” *European Physical Journal B*, vol. 14, no. 1, pp. 1–10, 2000.
- [218] D. R. Tilley and J. Tilley, *Superfluidity and superconductivity. Second edition*. Hilger, 1986.
- [219] A. Mourachkine, *Room-temperature superconductivity*, vol. 7. Cambridge International Science Publishing, 2004.
- [220] A. F. Mayadas, R. B. Laibowitz, and J. J. Cuomo, “Electrical characteristics of rf-sputtered single-crystal niobium films,” *Journal of Applied Physics*, vol. 43, no. 3, pp. 1287–1289, 1972.
- [221] A. N. Lykov, “The superconducting mixed state of artificial microstructures,” *Advances in Physics*, vol. 42, no. 3, pp. 263–342, 1993.
- [222] A. I. Gubin, K. S. Il’in, S. A. Vitusevich, M. Siegel, and N. Klein, “Dependence of magnetic penetration depth on the thickness of superconducting Nb thin films,” *Physical Review B - Condensed Matter and Materials Physics*, vol. 72, no. 6, 2005.
- [223] S. Mironov, A. Mel’nikov, and A. Buzdin, “Vanishing Meissner effect as a Hallmark of in-Plane Fulde-Ferrell-Larkin-Ovchinnikov Instability in Superconductor-Ferromagnet Layered Systems,” 2012.
- [224] S. Aull, O. Kugeler, and J. Knobloch, “Trapped magnetic flux in superconducting niobium samples,” *Physical Review Special Topics - Accelerators and Beams*, vol. 15, no. 6, 2012.
- [225] A. K. Geim, S. V. Dubonos, J. G. Lok, M. Henini, and J. C. Maan, “Paramagnetic Meissner effect in small superconductors,” *Nature*, vol. 396, no. 6707, pp. 144–146, 1998.

REFERENCES

- [226] W. Braunisch, N. Knauf, V. Kataev, S. Neuhausen, A. Grütz, A. Kock, B. Roden, D. Khomskii, and D. Wohlleben, “Paramagnetic Meissner effect in Bi high-temperature superconductors,” *Physical Review Letters*, vol. 68, no. 12, pp. 1908–1911, 1992.
- [227] D. J. Thompson, M. S. Minhaj, L. E. Wenger, and J. T. Chen, “Observation of paramagnetic meissner effect in niobium disks,” *Physical Review Letters*, vol. 75, no. 3, pp. 529–532, 1995.
- [228] X. Han, W. Mi, and X. Wang, “Large magnetoresistance and spin-polarized photocurrent in La $2/3$ Sr $1/3$ MnO 3 (Co)/quaterthiophene/La $2/3$ Sr $1/3$ MnO 3 organic magnetic tunnel junctions,” *Journal of Materials Chemistry C*, vol. 7, no. 14, pp. 4079–4088, 2019.
- [229] S. Mironov, A. S. Mel’nikov, and A. Buzdin, “Electromagnetic proximity effect in planar superconductor-ferromagnet structures,” *Citation: Appl. Phys. Lett*, vol. 113, p. 22601, 2018.